

Deposition and Characterization of Electronics Materials in Bionanotechnology and Micro/Nano-electronics

BY

Nickolas Dean Anderson
B.S., University of Illinois at Chicago, 2014

THESIS

Submitted as partial fulfillment of the requirements
for the degree of Doctor of Philosophy in Bioengineering
in the Graduate College of the
University of Illinois at Chicago, 2019

Chicago, Illinois

Defense Committee:

Christos Takoudis, Chemical Engineering and Bioengineering, Chair and Co-Advisor
Greg Jursich, Chemistry and Bioengineering, Co-Advisor
Michael Strosio, Bioengineering
Salman Khetani, Bioengineering
Shiv Joshi, NextGen Aeronautics

ACKNOWLEDGEMENTS

First and foremost, I would like to thank my co-advisers Dr. Gregory Jursich and Prof. Christos Takoudis for their insightful suggestions, mentorship and their numerous contributions to the research projects. Their guidance, support and dedication to teaching were invaluable throughout my studies.

Additionally, I would like to thank Dr. Shiv Joshi, Dr. Yuzheng Zhang, Robert Demott, and Scott Bland of NextGen Aeronautics for their help with the research and helpful discussions. I also thank Nicole Szorc, Vimal Gunasekaran, Jeet Bhalala, Anuj Singhal, and John Sabino for their help with the research. I would also like to thank Dr. David Smith, Dr. Paul Lemaire and Dr. Dennis Hausmann from Lam Research for their helpful discussions. I additionally thank Dr. Rajib Mukherjee and Dr. Urmila Diwekar for their help with the research on modeling atomic layer deposition. I would also like to thank Prof. Constantine Megaridis, Prof. Alan Zdunek, Prof. Alan Feinerman and Prof. Salman Khetani for access to their laboratories and use of their equipment for parts of this research. I also thank the Bioengineering support staff, Susan Lee, Jessica Meija and Lukasz Zientara for all their help.

I also thank the AMReL group members and alumni for their help and support. This research was supported by NextGen Aeronautics, the Office of Naval Research [contract number N00014-14-C-0028], the National Science Foundation [grant number DMR-1309114], and Lam Research.

Last, but certainly not least I thank my family, friends and girlfriend for their patience, love and support throughout my graduate career.

Contribution of Authors

Chapter 1 provides a brief introduction to the techniques used in the dissertation. Chapter 2 is adapted from a published manuscript for which I am the primary author. Chapter 3 is partially adapted from published manuscripts for which I am a co-author. For chapter 2, Nicole Szorc and Vimal Gunasekaran assisted with the experiments. Chapter 2.1 was published in *Sensors and Actuators A: Physical*. For chapter 3, Dr. Yuzheng Zhang performed the cross-sectional SEM, fatigue testing, and tensile testing of strain gauges and transistors as well as cross-sectional SEM and tensile testing of the strain gauge arrays while I fabricated all the devices which were characterized and performed all other characterization. More specifically, Dr. Yuzheng Zhang generated Figures 11, 12, 15, 16 17, 23, 27, 28, 30, 32, 35, 36 and 37. Portions of chapter 3 were published in *Sensors and Actuators A: Physical* and *SPIE: Industrial and Commercial Applications of Smart Structures Technologies*. For chapter 4, Dr. Arghya Bishal performed the atomic layer deposition of the titanium dioxide and platinum, ellipsometry, ATR-FTIR, XPS and SEM of the collagen samples after ALD deposition and assisted with the electrical measurements. More specifically, Dr. Arghya Bishal generated Figures 39, 40, 43, and 45. Chapter 4 is currently under revision for publication in *Biosensors and Bioelectronics*. For chapters 5 and 6, Soumya Saha assisted with the atomic layer deposition of zirconia, ellipsometry measurements and X-ray photoelectron spectroscopy. Chapter 5 has been submitted to the *ECS Journal of Solid State Science and Technology*. Chapter 6 is being prepared for publication. For appendix B.1, Dr. Rajib Mukherjee and Dr. Urmila Diwekar developed the theoretical model. For appendix B.2, Jeet Bhalala, and Lyla Handoklow assisted with the screen-printing and resistance measurements, and Anuj Singhal assisted with the laser trimming. My advisers, Dr. Gregory M. Jursich and Prof. Christos G. Takoudis helped with project planning, design of experiments and manuscript corrections.

TABLE OF CONTENTS

<u>CHAPTER</u>		<u>PAGE</u>
1.	INTRODUCTION	1
1.1	Electronics Materials.....	1
1.2	Screen Printing.....	1
1.3	Atomic Layer Deposition.....	1
1.4	Selective Atomic Layer Deposition.....	2
2.	SCREEN PRINTED STRAIN GAUGES RESULTS AND INK COMPOSITION OPTIMIZATION	4
2.1	Introduction.....	4
2.2	Methods and Materials.....	8
2.2.1	Strain Gauge Printing.....	8
2.2.2	Electromechanical Measurements.....	8
2.2.3	Optical Microscopy.....	10
2.3	Results.....	10
2.3.1	Strain Gauge Resistance.....	10
2.3.2	Strain Gauge Sensitivity.....	13
2.3.3	Strain Gauge Variability.....	17
2.4	Conclusions.....	19
3.	SCREEN PRINTED CARBON STRAIN GAUGES, STRAIN GAUGE ARRAYS AND SCREEN PRINTED TRANSISTORS	21
3.1	Introduction.....	21
3.2	Methods and Materials.....	27
3.2.1	Screen Printing of Carbon Gauges.....	27
3.2.2	Screen Printing of Strain Gauge Arrays.....	28
3.2.3	Screen Printing of Transistors.....	28
3.2.4	Strain Measurements.....	33
3.2.5	Fatigue Measurements.....	35
3.2.6	I-V Measurements of Transistors.....	35
3.2.7	Microscopy and Profilometry.....	35
3.3	Results.....	35
3.3.1	Screen Printed Carbon Strain Gauges.....	35
3.3.2	Screen Printed Strain Gauge Arrays.....	44
3.3.3	Screen Printed Transistors.....	58
3.4	Conclusions.....	70
4.	ATOMIC LAYER DEPOSITION OF PLATINUM ON COLLAGEN	73
4.1	Introduction.....	73
4.2	Methods and Materials.....	75
4.2.1	Sample Preparation.....	75
4.2.2	Surface Characterization.....	76
4.2.3	Electrical Characterization.....	76
4.3	Results.....	81
4.4	Conclusions.....	90
5.	SELECTIVE ATOMIC LAYER DEPOSITION OF ZIRCONIA ON ELECTROPLATED COPPER	92
5.1	Introduction.....	92

TABLE OF CONTENTS (Continued)

<u>CHAPTER</u>		<u>PAGE</u>
	5.2 Methods and Materials.....	93
	5.3 Results.....	94
	5.4 Conclusions.....	104
6.	SELECIVE ATOMIC LAYER DEPOSITION OF ZIRCONIA ON CHEMICALLY MECHANICALLY POLISHED COPPER.....	106
	6.1 Introduction.....	106
	6.2 Methods and Materials.....	108
	6.3 Results.....	109
	6.4 Conclusions.....	119
	CITED LITERATURE.....	123
	APPENDICES.....	133
	Appendix A.....	134
	Appendix B.....	136
	VITA.....	148

LIST OF TABLES

<u>TABLE</u>	<u>PAGE</u>
I. COMPARISON OF GAUGE FACTORS AND MATERIALS FOR SCREEN PRINTED STRAIN SENSORS REPORTED IN LITERATURE. *GAUGE FACTORS APPROXIMATED FROM FIGURES.	7
II. AVERAGE RESISTANCES, AVERAGE GAUGE FACTORS AND AVERAGE CORRELATION COEFFICIENTS FROM LINEAR REGRESSION ANALYSIS FOR EIGHT GAUGES OF EACH COMPOSITION AND FOUR COMMERCIAL GAUGES (CONSTANTAN (CU-NI) GAUGES, KFH-20-120-C1-11L1M2R FROM OMEGA.....	15
III. SUMMARY OF PRINTED THIN FILM TRANSISTOR LITERATURE WHERE REFERENCES FOUR THROUGH NINE WERE CONSIDERED ALL-PRINTED.....	25
IV. CHANNEL DIMENSIONS FOR THE ARRAY OF SCREEN-PRINTED TRANSISTORS...	28
V. AVERAGE RESISTANCE, STANDARD DEVIATION, AND DEVIATION OF THE MAXIMUM AND MINIMUM RESISTANCE FROM THE MEAN FOR (A) ONE OF OUR EARLIEST PRINTED STRAIN GAUGE ARRAYS, AND (B) A STRAIN GAUGE ARRAY THAT WAS PRINTED AFTER REDUCING THE VARIATION IN OFFSET DISTANCE BETWEEN DIFFERENT AREAS OF THE SCREEN.....	46
VI. ELECTRICAL RESISTIVITY OF THE CONTROL NON-COATED AND ALD PT COATED COLLAGEN SAMPLE GROUPS AND THE CORRESPONDING PT FILM THICKNESS AS MEASURED ON REFERENCE SI SAMPLES.....	81
VII. PEAKS OBSERVED FROM X-RAY PHOTOELECTRON SPECTRA OF THE COPPER SUBSTRATES SHOWN IN FIGURE 53. SPECTRA WERE ALIGNED TO HAVE THE CARBON 1S PEAK AT 284.8 EV.....	111
VIII. ATOMIC PERCENTAGES CALCULATED FROM THE SURVEYS. EP: ELECTROPLATED CU SUBSTRATE. CMP: CHEMICALLY MECHANICALLY POLISHED CU SUBSTRATE.....	111
IX. CONTRIBUTIONS TO THE CU $L_{3M_{4.5}M_{4.5}}$ PEAKS FROM CU_2O , $CU(0)$, CUO , AND $CU(OH)_2$ CALCULATED FROM FITTING THE PEAKS SHOWN IN FIGURE 55.....	114
X. ATOMIC PERCENTAGES CALCULATED FROM THE SURVEYS. CMP: CHEMICALLY MECHANICALLY POLISHED CU SUBSTRATE AFTER DI H_2O RINSE AND N_2 DRY. CMP-ETOH: CHEMICALLY MECHANICALLY POLISHED CU SUBSTRATE AFTER ETOH TREATMENT. CMP: CHEMICALLY MECHANICALLY POLISHED CU SUBSTRATE AFTER HEAT TREATMENT.....	117

LIST OF TABLES (CONTINUED)

<u>TABLE</u>	<u>PAGE</u>
XI. SCREEN PRINTED LINE WIDTHS AND APPROXIMATE THICKNESSES FOR GAUGES WITH DIFFERENT LINE WIDTH DESIGNS. LINE WIDTHS WERE MEASURED FROM THE OPTICAL MICROSCOPY IMAGES AND LINE THICKNESSES WERE APPROXIMATED FROM THE OPTICAL PROFILOMETRY IMAGES SHOWN IN FIGURE 61.....	139
XII. AVERAGE RESISTANCES AND STANDARD DEVIATIONS FOR DUPONT 7102 CARBON GAUGES SCREEN PRINTED ONTO PET.....	142
XIII. RESISTANCES AND GAUGE FACTORS BEFORE AND AFTER LASER TRIMMING FOR TWO DUPONT 7102 CARBON 45-DEGREE ROSETTES ON PET. GAUGE FACTORS INCLUDE THE STANDARD ERROR FROM THE LINEAR REGRESSION. GAUGE 90-2 WAS DAMAGED BY THE LASER TRIMMING DUE TO MISALIGNMENT OF THE LASER.....	143

LIST OF FIGURES

<u>FIGURE</u>		<u>PAGE</u>
1.	Diagram of the typical metal oxide atomic layer deposition process.....	3
2.	(a) Optical image of one set of four printed strain gauge patterns which used 60 wt.% carbon ink for the gauge elements and (b) a diagram of the strain gauge printing procedure.....	9
3.	Diagram of strain due to curvature, where y is the distance of the top of the gauge element from the neutral axis, NA is the neutral axis, and ρ is the radius of curvature.....	11
4.	Average resistances versus gauge composition shown as weight percent carbon ink. The bottom portion of the graph indicates the standard deviation of the resistances from eight gauges of each composition.....	12
5.	Relative change in resistance versus strain for 0, 40, and 100 wt. % carbon ink gauges along with a commercial constantan strain gauge, with linear regression fits for set of resistance-strain measurements with each gauge using a zero y-intercept constraint.....	14
6.	Average gauge factors versus gauge composition shown as weight percent carbon ink. Error bars and the bottom portion of the graph indicate the standard deviation of the gauge factors from eight gauges of each composition.....	16
7.	Optical microscopy images of the ink that composes the gauge element of our strain gauges at 500X magnification. The text in the upper left-hand corner of each image refers to the weight percent carbon ink used.	18
8.	Diagram of the proposed system for structural monitoring of aircraft.....	22
9.	Diagram of the screen-printing procedure for preparing strain gauge arrays. The substrate used was 2-mil thick polyimide, Kapton HN, from DuPont, the carbon ink used was DuPont 7102C, the silver ink used was Conductive Compounds Ag-530, the dielectric ink used was Conductive Compounds UV-2531, and the discrete transistors were attached using silver epoxy.....	31
10.	Diagram of the transistor printing process. The S-SWNCT solution used was IsoSol-S100, 99.9+% semiconducting CNTs in toluene (NanoIntegris), the silver inks used were DuPont 5028 and Ag-530 (Conductive Compounds), and the barium titanate dielectric ink used was BT-101 (Conductive Compounds).....	32
11.	(a) Micro-tensile measurement apparatus and (b) geometry of dog-bone specimens for tensile testing of carbon strain gauges.....	34
12.	Diagram of (a) longitudinal and (b) transverse loading applied with four-point bending for fatigue testing of printed strain gauges.....	36
13.	Diagram of the I-V setup for characterizing transistors. Electrical potentials are applied from the drain to the source and from the gate to the source, and the electrical current is measured between the drain and source.....	37

LIST OF FIGURES (Continued)

<u>FIGURE</u>		<u>PAGE</u>
14.	Screen printed strain gauges with line widths ranging from 125 μm to 1,100 μm	38
15.	Microstructure of a screen-printed carbon gauge composed of DuPont 7082 carbon ink with an over-layer of DuPont 5028 silver ink.....	40
16.	Strain response of a screen-printed strain gauge showing (a) the same linear response with tension and recovery at 1.1% strain and (b) the same linear response when cycling at different levels of strain up to 0.9% strain.....	41
17.	(a) Change in resistance with strain divided by the unstrained resistance vs. tensile strain and (b) gauge factor versus loading cycles, showing the same linear response and gauge sensitivity after 10^5 cycles of 0.2% strain.....	42
18.	Temperature response of the DuPont 7082 carbon ink used for the gauge element.....	43
19.	Color maps of the deviation of the resistance values of each strain gauge from the mean resistance for the sheet of 64 strain gauges. (a) Resistance values prior to optimizing the printing procedure. (b) Resistance values after optimizing the printing procedure, where the procedure was optimized by adjusting the distance between the screen pattern and the substrate.....	45
20.	Resistance change of free-standing carbon ink blocks as a function of temperature. (a) DuPont 7102. (b) DuPont 7082.....	47
21.	Configuration of the strain gauge array with dummy gauge for temperature compensation.....	49
22.	Optical profilometry image of Kapton HN polyimide film.....	50
23.	Cross-sectional images of (a) carbon and (b) silver inks used for fabricating strain gauge arrays showing void-free interfaces when screen-printed onto a polyimide substrate.....	51
24.	Image of a screen printed 45° rosette with temperature compensation gauge and silver traces, where gauge line widths are 305 μm , gauge lengths are 7.7 mm and silver trace line widths are 305 μm	53
25.	Normalized change in resistance versus microstrain showing the linear response of four separate gauges and a gauge factor of approximately 18 ± 0.7	54
26.	(a) Fully printed 4x4 strain gauge array and (b) a fully printed 4x4 strain gauge array bonded to an aluminum plate with discrete bare-die transistors and data acquisition connector bonded to the substrate.....	55
27.	Uniaxial tension test of a printed strain sensor array on an aluminum test sheet.....	56

LIST OF FIGURES (Continued)

<u>FIGURE</u>		<u>PAGE</u>
28.	(a) Response from the row 1, column 1 strain sensor during 3 different runs of the axial tension test, and (b) strain gauge rosettes that suffered debonding of at least one transistor during the test cycles.....	57
29.	Optical image of top-gate screen-printed transistors on a PET substrate.....	59
30.	Cross-sectional image of the source and drain of a transistor (a) without a flattened source and drain layer and (b) with a flattened source and drain layer and debonding between the source and drain layer and the substrate.....	60
31.	Histograms of frequency versus thickness from optical profilometry of (a) as-printed and (b) mechanically flattened silver ink.....	62
32.	SEM cross-sectional image of a transistors showing variation of the dielectric thickness between the channel region and the source/drain region.....	63
33.	I-V responses of screen-printed transistors on (a) an uncoated PET substrate and (b) an alumina coated PET substrate.....	64
34.	Optical profilometry images of (a) an uncoated PET substrate and (b) an alumina coated PET substrate showing the much more textured surface of alumina coated PET.....	65
35.	Cross-sectional SEM of (a) unstrained Al ₂ O ₃ coated PET before printing and (b) after transistor printing and 2% strain.....	67
36.	Cross-sectional SEM images of (a) an unstrained transistor, (b) a transistor after one cycle of 10,000 $\mu\epsilon$ strain was applied, and (c) a transistor after 10 ⁵ cycles of 1,000 $\mu\epsilon$ were applied....	68
37.	Cross-sectional SEM images of a transistor with (a) incompatible conductive and dielectric inks and (b) more compatible conductive and dielectric inks.....	69
38.	Optical images of transistors, (a) a top-gate transistor and (b) a bottom-gate transistor, showing the effects of the carbon nanotube solution when deposited first for top-gate transistors and last for bottom-gate transistors.....	71
39.	Schematic of the custom-built ALD reactor used for deposition onto the collagen membrane.....	78
40.	Schematic representation of the ALD process for preparing different collagen sample groups. Coll-Pt400 has 400 ALD cycles of Pt. Coll-TiO ₂ -Pt200 has 9 nm of TiO ₂ deposited via ALD and 200 ALD cycles of Pt. Coll-TiO ₂ -Pt400 has 9 nm of TiO ₂ deposited via ALD and 400 ALD cycles of Pt.....	79
41.	Diagram of the electrical measurement setup. 1, 2, 3, and 4 indicate the contact numbers for the screen-printed silver ink contacts. Low V and High V indicate the low and high potential connections to the LCR meter, and Low I and High I indicate the low and high current connections to the LCR meter.....	80

LIST OF FIGURES (Continued)

<u>FIGURE</u>	<u>PAGE</u>
42. Optical microscopy images of collagen films coated with platinum or titanium dioxide and platinum at 500x magnification showing the surface features of the collagen samples. The control sample is a collagen membrane as received. The Coll-Pt400 sample has 400 ALD cycles of platinum on a collagen. The Coll-TiO ₂ -Pt200 and Coll-TiO ₂ -Pt400 samples have ~9 nm of TiO ₂ and 200 and 400 ALD cycles of Pt, respectively.....	82
43. SEM images of the collagen films with ALD Pt or ALD TiO ₂ /Pt at 50,000X magnification showing the surface morphology at the nanoscale. The control is the pristine collagen sample, Coll-Pt400 has 400 ALD cycles of Pt, Coll-TiO ₂ -Pt200 and Coll-TiO ₂ -Pt400 are coated with ~9 nm of TiO ₂ and 200 ALD and 400 ALD cycles of Pt, respectively.....	83
44. SEM images of the collagen films after 5 and 10 minutes of ozone exposure at 20,000X magnification showing the morphology of the collagen fibers.....	86
45. Chemical analysis of collagen samples. (a) ATR-FTIR spectrum of collagen sample groups. (b) X-ray photoelectron spectra of the Coll-TiO ₂ -Pt400 group showing Pt core level energy region. (c) Proposed chemical bonding of the ALD-Pt coating with the collagen molecule.....	87
46. (a) Photograph of all the collagen sample groups showing color difference due to Pt nucleation on collagen surfaces. (b) Photograph of electrical conductivity test using LED light showing only Coll-TiO ₂ -Pt400 provided sufficient conductivity to illuminate the LED, but sufficient conductivity was not provided by the other sample groups. (c) Average volume resistivity versus microstrain for the Coll-Pt400 and Coll-TiO ₂ -Pt400 samples. Error bars indicate the standard deviation of the volume resistivity from three measurements on each sample. Inset photographs show the bending of ALD-Pt coated collagen samples. (d) Photograph of the flexible Coll-TiO ₂ -Pt400 sample that provided sufficient conductivity to illuminate the LED while the sample was in a flexed state.....	91
47. High-resolution X-ray photoelectron spectra of the electron beam evaporated (EB) and electroplated copper (EP) substrates after a DI H ₂ O rinse and N ₂ dry. (a) C 1s. (b) O 1s. (c) Cu LMM. (d) Cu 2p.....	96
48. (a) ZrO ₂ film thickness on silicon and electroplated copper coated silicon substrates versus number of ALD cycles, where film thickness was measured via spectral ellipsometry and error bars indicate the uniformity of the film across the samples. Deposition consisted of a 5-minute ethanol pretreatment and 2-minute Ar purge followed by 2 s ZyALD:15 s Ar and 15 s ethanol:30 s Ar pulses at 200°C. (b-c) X-ray photoelectron spectra of samples prepared with a 5-minute ethanol pretreatment and 0 to 200 ALD cycles of ZrO ₂ . (b) Spectra for electroplated copper coated silicon substrates. (c) Spectra for silicon substrates.	99
49. X-ray photoelectron spectra of samples prepared with different ethanol pretreatment times and 100 ALD cycles of ZrO ₂ . (a) Spectra for silicon substrates. (b) Spectra for electroplated copper coated silicon substrates.....	100
50. Ratio of Zr 3d Area (Si/Cu) vs. ethanol pretreatment time.....	101

LIST OF FIGURES (Continued)

<u>FIGURE</u>	<u>PAGE</u>
51. X-ray photoelectron spectra of electroplated copper after DI water rinse (EP) and after 60 minutes of in-situ ethanol treatment at 200°C (EP-EtOH). (a) C 1s. (b) O 1s. (c) Cu LMM. (d) Cu 2p.....	103
52. Spectral ellipsometry measurements of ZrO ₂ thickness and growth rate on silicon substrates from 70 ALD cycles. (a) ZrO ₂ growth rate versus precursor pulse times when an oxidizer pulse time of 15 seconds was used. (b) ZrO ₂ growth rate versus oxidizer pulse times when a precursor pulse time of 7 seconds was used.....	110
53. X-ray photoelectron spectra of the copper substrates. EP: Spectra for the electroplated Cu substrate. CMP: spectra for the chemically mechanically polished Cu substrate. Spectra were aligned to have the carbon 1s peak at 284.8 eV and all samples were rinsed with DI water and dried with N ₂ prior to XPS.....	112
54. X-ray photoelectron spectra from electroplated (EP) and chemically mechanically polished (CMP) Cu substrates. (a) C 1s. (b) O 1s. (c) Cu LMM. (d) Cu 2p.....	115
55. High-resolution X-ray photoelectron spectra of the copper Cu L ₃ M _{4.5} M _{4.5} region with peak fitting. (a) Spectra for the electroplated Cu substrate. (b) Spectra for the chemically mechanically polished Cu substrate. Spectra were aligned to have the carbon 1s peak at 284.8 eV and all samples were rinsed with DI water and dried with N ₂ prior to XPS.....	116
56. X-ray photoelectron spectra after 50 and 70 ALD cycles of ZrO ₂ on (a) CMP copper and (b) Si substrates, after a 5-minute in-situ EtOH treatment at 200°C.....	118
57. X-ray photoelectron spectra from CMP Cu substrates with different treatments. CMP: Spectra for the CMP Cu substrate after a DI H ₂ O rinse and N ₂ dry. CMP-EtOH: Spectra for the CMP Cu substrate after 60 minutes of EtOH treatment at 200°C and 1500 mTorr with EtOH/N ₂ flow. CMP-HT: Spectra for the CMP Cu substrate after 1 hour of heating at 335 °C and 640 mTorr with N ₂ flow. Spectra were aligned to have the carbon 1s peak at 284.8 eV (a) C 1s. (b) O 1s. (c) Cu LMM. (d) Cu 2p. (e) N 1s.....	121
58. X-ray photoelectron spectra after 70 ALD cycles of ZrO ₂ on (a) CMP copper and (b) Si substrates after a 60-minute heat treatment at 335 °C and 640 mTorr and a 5-minute in-situ EtOH treatment at 200°C.....	122
59. Experimental and theoretical growth rates of ZrO ₂ on silicon substrates versus precursor pulse time. (a) Experimental growth rates are from ALD performed using ZyALD as the Zr precursor and ethanol as the oxidizer and theoretical growth rates are from the interaction parameters from ZyALD and ethanol. (b) Experimental growth rates are from ALD performed using ZyALD as the Zr precursor and oxygen/ozone as the oxidizer and theoretical growth rates were calculated using the interaction parameters from ZyALD and ethanol.....	138
60. Image of screen-printed DuPont 7102 carbon strain gauges on PET.....	140

LIST OF FIGURES (Continued)

<u>FIGURE</u>	<u>PAGE</u>
61. Optical microscopy and optical profilometry images of DuPont 7102 carbon ink strain gauges screen printed onto PET. The top images correspond to the finest line width devices (150 μm), the middle images correspond with the intermediate line width devices (250 μm), and the bottom images correspond to the thickest line width devices (500 μm).....	141
62. DuPont 7102 carbon gauges on PET after laser trimming. Red circles indicate where the laser trimming was performed.....	144
63. $\Delta R/R$ versus laser trimming iteration for two DuPont 7082 carbon strain gauges on PET.....	145
64. $\Delta R/R$ versus microstrain for two DuPont 7102 carbon 45-degree rosettes on PET before and after laser trimming. Gauge 90-2 was damaged by the laser trimming.....	146

LIST OF ABBREVIATIONS

ALD	Atomic Layer Deposition
ATR-FTIR	Attenuated Total Reflection Fourier Transform Infrared Spectroscopy
BTA	Benzotriazole
CBM	Condition Based Maintenance
CMP	Chemically Mechanically Polished
CNT	Carbon Nanotube
Cu	Copper
EP	Electroplated
GF	Gauge Factor
IR	Infrared
I-V	Current-Voltage
LCR	Inductance-Capacitance-Resistance
NAVAIR	Naval Air Systems Command
PET	Polyethylene Terephthalate
Pt	Platinum
SALD	Selective Atomic Layer Deposition
SEM	Scanning Electron Microscopy
S-SWCNT	Semiconducting Single-Walled Carbon Nanotube
TDMAT	Tetrakis(dimethylamido) titanium
TiO ₂	Titanium Dioxide
UAV	Unmanned Aerial Vehicle
Wt. %	Weight Percent
XPS	X-ray Photoelectron Spectroscopy
ZrO ₂	Zirconia
ZyALD™	Tris(dimethylamino)cyclopentadienyl zirconium

SUMMARY

Electronics materials and especially electronics materials for flexible electronics are of increasing interest in numerous applications from wearable health monitoring, displays, and consumer electronics to structural health monitoring and energy harvesting. Deposition of materials with desired thickness and composition through scalable processes is vital to ensure flexibility, device functionality and translation to commercial processes. Graphic printing techniques and atomic layer deposition (ALD) were utilized to deposit these materials. Graphic printing techniques are of interest for large-scale fabrication where low-cost is the primary driving force, thick films are desirable and constraints on device performance are relatively relaxed. Whereas ALD is used for large-scale fabrication when film quality, device performance, and device reliability are paramount, thin films are desirable and cost is less of a concern. This thesis focuses on materials deposited using these two techniques for fabricating electronics and characterization of the materials and devices.

Graphic printing, specifically screen printing, was used to deposit carbon and silver inks for fabrication of strain gauges for structural monitoring. The effect of different ink compositions from 100 wt.% silver ink to 100 wt.% carbon ink on the gauge sensitivity and linearity was investigated. Resistance measurements indicated a percolation threshold of approximately 40 wt.% carbon ink. At this percolation threshold, gauge sensitivity was approximately 66, whereas for the two pure inks, 100 wt.% silver ink and 100 wt.% carbon ink, gauge sensitivity was approximately 11 and 8, respectively. The linearity of the gauge response was found to depend mainly on the gauge resistance as gauges with low resistance were more affected by slight variations in probe placement. Variation in resistance was largest near the percolation threshold and was attributed to the sensitivity of the gauges to slight changes in composition at this region. While variation in gauge response was largest for 30 wt.% carbon gauges. This variation was attributed to variation in probe placement and limited miscibility of the inks near this region as agglomerates of silver ink were visible with optical microscopy.

Along with strain gauges composed of mixed inks, gauges composed entirely of carbon ink and arrays of strain gauges were studied. The gauges and arrays were studied to determine their suitability for large-area structural monitoring. In this effort, two carbon inks were studied for the use as the gauge element. In addition to the strain

SUMMARY (Continued)

gauges, screen printed transistors were studied for use as switches in the strain gauge arrays. Strain gauges were characterized via cross-sectional scanning electron microscopy (SEM), their resistance values, change in resistance with strain and fatigue, and change in resistance with temperature. For the first carbon ink, DuPont 7082, tensile testing showed the gauges exhibited a maximum strain level greater than 0.9% strain. Fatigue measurements showed the same linear response and sensitivity after 100,000 cycles of loading at 0.2% strain. Resistance versus temperature measurements found a temperature coefficient of resistance of $\sim 2.4 \times 10^{-3} \text{ K}^{-1}$ at room temperature. Cross-sectional SEM showed a void-free microstructure of the carbon ink, indicating its suitability for strain applications. However this carbon ink, DuPont 7082, had too high of resistance to be used in the strain gauge arrays and therefore, DuPont 7102 carbon ink was used. Gauges of DuPont 7102 carbon ink were characterized via cross-sectional SEM, their resistance, resistance variation across the array of 64 strain gauges, and change in resistance with strain and temperature. Cross-sectional SEM images showed that gauges of this ink also had void-free microstructures. Through optimization of the printing procedure, the resistance tolerances of the gauges were reduced to $\sim 20\%$. The gauges were found to exhibit linear responses to strain with gauge factors of ~ 18.8 . The temperature coefficient of resistance of the ink was measured to be $\sim 0.26 \times 10^{-3} \text{ K}^{-1}$. Transistors were evaluated by examining their microstructure with cross-sectional SEM and measuring their I-V characteristics before and after strain. Additionally, the effect of several process changes on the reliability of the printing process were investigated. Mechanically flattening the first silver ink layer was found to reduce the number of short circuits. Optimizing the dielectric thickness increased the on-off ratios of the transistors and printing on alumina coated PET increased the on-current. However, transistors were damaged under strain and fatigue. This damage was attributed to the brittle nature of the alumina coating and poor adhesion of the semiconductor to uncoated PET substrates.

Subsequent research shifted to the use of ALD for materials deposition. Platinum and titanium dioxide were deposited onto collagen membranes for biosensor and electrogenic tissue regeneration applications. ALD titanium dioxide was deposited using tetrakisdimethyl titanium and ozone, while ALD platinum was deposited using (Trimethyl)methylcyclopentadienylplatinum(IV) and ozone. The deposited films were imaged using SEM

SUMMARY (Continued)

and optical microscopy and were found to conformally coat the fibers of the collagen membranes. 400 ALD cycles were found to provide 100% surface coverage. ALD of TiO_2 prior to ALD of Pt was found to promote Pt nucleation to achieve a continuous film. Resistivity measurements of the Pt films were performed after screen printing silver ink contacts onto the films to reduce contact resistance and to prevent damage to the thin Pt films. With 400 ALD cycles of Pt and a 9 nm TiO_2 layer on collagen, volume resistivity was approximately half of that of 400 ALD cycles of Pt directly on collagen. The Pt coated membranes were further characterized by measuring the change in volume resistivity versus bending strain. Volume resistivity was found to increase by ~11% and 20% for strains of ~1.5% for Pt on collagen and Pt/ TiO_2 coated collagen, respectively. The larger increase with the TiO_2 coating was believed to be due to the larger overall thickness of the coating (~37%) or differences in adhesion with the TiO_2 coating. Attenuated total reflectance Fourier transform infrared spectroscopy (ATR-FTIR) and X-ray photoelectron spectroscopy (XPS) were used to characterize the chemical nature of the collagen sample groups. ATR-FTIR showed that the amide functional groups of the collagen film were not affected by the ALD processes. XPS showed that the films were metallic Pt, which was consistent with the resistivity measurements.

Selective atomic layer deposition (SALD) of zirconium oxide (ZrO_2) was performed using silicon and electroplated copper substrates, tris(dimethylamino)cyclopentadienyl zirconium as the zirconium precursor, and ethanol as the oxygen source and reducing agent for the copper substrates. This process selectively deposited ZrO_2 onto the silicon substrates for up to 70 ALD cycles with no deposition onto the electroplated copper substrates, where selectivity was determined and quantified using X-ray photoelectron spectroscopy. Selectivity above 70 cycles was improved through optimization of the initial ethanol reduction step. Changes in selectivity with the ethanol treatment were attributed to reduction of copper oxides and byproduct formation from adsorption of ethanol on the copper surface.

After demonstrating SALD of ZrO_2 for electroplated copper substrates, selective deposition was further studied using chemically mechanically polished copper substrates. Electroplated copper is of major interest for interconnects in integrated circuits; however, it must be chemically mechanically polished after deposition to

SUMMARY (Continued)

planarize the surface. Therefore, it is vital that SALD of ZrO_2 can be performed after the planarization process. The copper oxides and chemical species present on the chemically mechanically polished copper after various treatments were examined through X-ray photoelectron spectroscopy to explain the differences in selectivity of ALD ZrO_2 and to better understand the mechanisms for selective deposition. While selectivity for at least 70 ALD has been demonstrated for electron beam evaporated and electroplated copper, it has not been demonstrated for chemically mechanically polished copper. XPS studies of the substrate indicated that the corrosion inhibitor benzotriazole (BTA) was present from the polishing process and was not removed after ethanol treatment. Thus, it is likely the main cause of differences in selectivity between the electroplated and chemically mechanically polished copper substrates. Additional treatments were used to remove BTA from the surface and improved the selectivity, supporting this theory.

CHAPTER 1

INTRODUCTION

1.1 **Electronics Materials**

Electronics materials are generally classified as materials with desirable properties for use in the electrical industries. These can include the materials most commonly associated with electronics such as semiconductors, conductors, and dielectrics to polymers, ceramics, and composites used in packaging, circuit boards, displays, cables, etc. Due to the ubiquity of electronic devices there is a perpetual demand for new and improved materials and processes for their fabrication. Of particular interest are additive manufacturing techniques such as graphic printing and processes which reduce the number of fabrication steps.

1.2 **Screen Printing**

Screen printing is a graphic printing technique where a thixotropic material is deposited through a screen pattern consisting of a thin wire mesh and a polymer coating. The thin wire mesh serves as a support for the ink and polymer coating, where the polymer coating serves as a mask restricting the transfer of material. This modality allows for numerous materials to be deposited so long as they are formulated into thixotropic pastes of suitable viscosity for printing. The inks for screen printing are generally composed of particles of the material of choice, a polymer binder, and a solvent. The polymer binder is used to hold the material of choice together and adhere it to the substrate. The solvent reduces the viscosity for printing and evaporates during heating to produce the cured films.

1.3 **Atomic Layer Deposition**

Atomic layer deposition (ALD) is a technique where vapor phase chemicals called precursors are sequentially introduced to deposit various materials. The first precursor introduced reacts with active sites on the substrate to deposit an atomic layer of material. Any of the unreacted precursor or byproducts are then purged from the reactor and the second precursor is introduced. The second precursor reacts with the

active sites from the material deposited by the first precursor and is then purged from the reactor. As the precursors only react with the available active sites, the process is self-limiting, and the aforementioned steps are repeated sequentially until a desired film thickness is reached. As ALD is a self-limiting process, it produces conformal growth, uniform thickness over large areas, and pinhole-free dense films so long as there are sufficient active sites and sufficient precursor is used. A diagram of the ALD process is provided in **Figure 1** and the main steps of the process are shown in this figure.

1.4 Selective Atomic Layer Deposition

Selective atomic layer deposition (SALD), as its name suggests, selectively deposits material using atomic layer deposition. To provide selective deposition, SALD generally relies on either area-activation or area-deactivation. Area-activation SALD primarily relies on formation of a thin layer of the desired material in a specific area which provides nucleation sites for the SALD process, while deposition does not occur on areas without these nucleation sites. The materials that can be deposited by this approach are fairly limited as they must not nucleate on the materials of the non-growth area. Area-deactivation SALD typically relies on materials deposited on the non-growth area to prevent deposition while growth occurs on all other areas. With careful selection of the deactivating material, numerous materials can be deposited and the most commonly used materials to prevent deposition are self-assembled monolayers or polymers. The downside of this approach is that the deactivating materials often have low thermal stability and typically must be removed after the SALD process, increasing the number of fabrication steps.

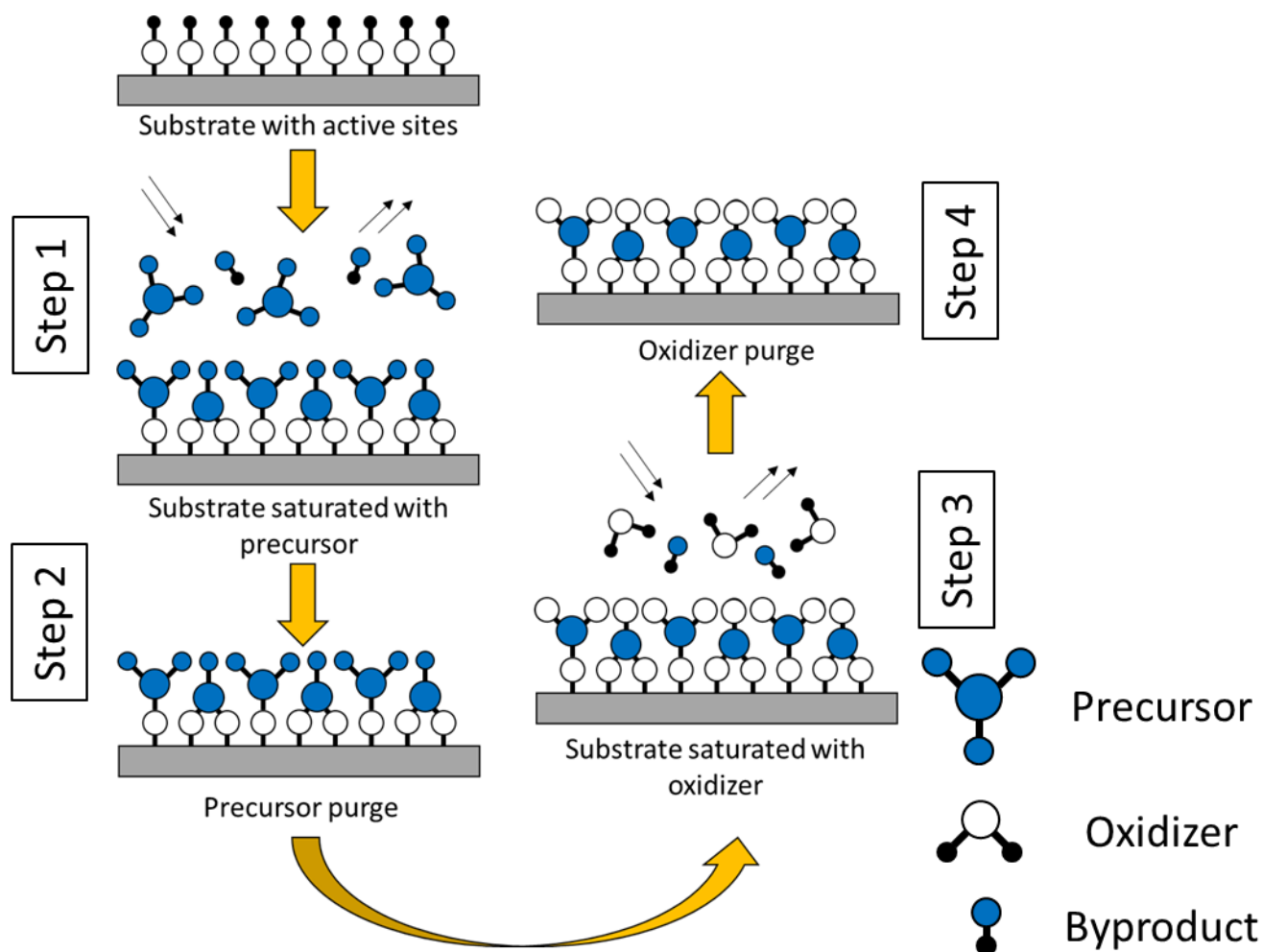


Figure 1. Diagram of the typical metal oxide atomic layer deposition process. Prior to step one, the substrate is covered with active sites. During step one, precursor flows into the reactor for a set period of time and reacts with the available active sites on the substrate until the substrate is saturated with the precursor. During step two, precursor flow is stopped, and any unreacted precursor and byproducts are purged from the system using an inert gas. In step three, an oxidizer flows into the reactor for a set period of time and reacts with the active sites from the precursor until all active sites are occupied. Then in step four, oxidizer flow is stopped, and any unreacted oxidizer and byproducts are purged from the system using an inert gas. These four steps are repeated cyclically until the desired thickness or number of cycles is reached.

CHAPTER 2

Screen Printed Strain Gauges and Ink Composition Optimization

(Previously Published as Anderson, N., Szorc, N. Gunasekaran, V. Joshi S., & Jursich G. (2019) “Highly Sensitive Screen printed Strain Sensors on Flexible Substrates via Ink Composition Optimization.” *Sensors and Actuators A: Physical*. 290, 1-7.)

2.1 Introduction

Strain sensors are in high demand in a vast number of diverse applications ranging from structural integrity analysis in automobiles, aerospace vehicles, and civil structures to medical diagnostics with wearable equipment and monitoring systems. For resistive strain sensors, the resistance change with strain is used to quantify the amount of strain applied. The magnitude of the resistance change with strain defines its sensitivity or gauge factor and this is determined by the piezoresistivity of the sensor material along with its geometric dimensions. Commercial sensors are often made of either thin metal foil or single-crystal doped silicon. [1–3] For these materials, the mechanism of resistance change with strain is quite different, leading to much different piezoresistivity properties. For metals, strain leads to small increases in resistance due to electron scattering effects whereas for semiconductors such as doped silicon, strain results in changes in the bandgap of the material leading huge influence on resistivity and thus high sensitivity. Although semiconductor materials lead to highly sensitive sensors, their applications are limited to only rigid frameworks where temperature changes are small, and the rigidity of the semiconductor material can be tolerated. Metal foil gauges offer more flexibility but at a price of much lower sensitivity. For a comparison, gauge factors as high as 100 were achieved by Smith with single-crystal silicon [1,2] while gauge factors of approximately 2 are typically reported for metal foil gauges. [3]

Recently, interest in strain sensor manufacturing methods has shifted from high-cost vacuum deposition and etching processes towards lower-cost graphic printing techniques. This shift is further driven by easy scalability of print manufacturing offering large area systems at low cost coupled with advancing technologies of print manufacturing. In the past, printed strain gauges have been prepared with numerous different methods using various composite ink formulations of conductive particles. Previous printed sensors have gauge factors ranging from 0.35 [4] to 50,000 [5], with most gauge factors being between 1 and 10, [4,6–20]. Only in the cases of very high strain

(> 20%) [5], custom ink formulations [5,21–24] or special gauge preparation [25] are gauge factors greater than ~30 observed. Table 1 below summarizes previous literature results on screen printed strain sensors using a variety of inks.

One of the most versatile bench scale printing techniques is screen printing and this is the print method of this work. In screen printing, a squeegee is used to transfer material through a screen pattern composed of a thin wire mesh and a polymer coating. The polymer coating serves as a mask, restricting the transfer of material and creating a patterned deposit, while the mesh serves as a support for the polymer coating and the material to be deposited. Using this modality, numerous materials can be deposited so long as they are formulated into a thixotropic paste such that they do not readily flow through the screen until a shear force is applied via the squeegee [26].

Printed gauges typically use composite inks composed of conductive particles embedded in either a less conductive or insulating polymer matrix. Given that the conductive particles are much more conductive than the polymer matrix, the conductivity of the printed material strongly depends on particle loading, particle size, and distribution which, in turn, is influenced by strain. For conductive particles within an insulating matrix, the minimal volume fraction of conductive particles at which the composite material becomes conductive is termed the percolation threshold [26]. The percolation threshold is the point at which electrical conduction transitions from passing primarily through a highly resistive polymer matrix composition to the much higher conductive elements. Near this transition point, the conductivity of the composite material becomes highly sensitive to factors which affect particle distribution such as mechanical strain [27] and as a result strain gauge sensitivity becomes greatly enhanced. In fact in some cases gauge factors over 1000 have been reported under strain conditions greater than 20% [5,25]

Here we report the averages and relative standard deviations of resistance and strain sensitivity for multiple sets of strain gauges prepared by screen printing using mixtures of commercially available conductive silver particle and resistive graphite inks. Gauge factors from approximately 8 to 66 are observed with changes in composition and inverse relation between sensitivity and repeatability is clearly seen. It is also important to note from this work that the changes in gauge factor with composition are more gradual when blending a conductive ink with a resistive ink rather than highly insulating polymer ink alone as done in previous work [27]. With more gradual change in

sensitivity, one has better manufacturing control when optimizing sensitivity and repeatability of a sensor to a particular application requirement thus permitting optimal sensitivity and repeatability of the sensors for a particular application.

Overall, this work demonstrates not only a simple means of enhancing printed strain gauge sensitivity but shows the degree of which sensor fabrication repeatability is affected over a large number of printed sensors. Further, since readily available ink materials are used in a low-cost, industrially-viable printing process, this approach can easily be scaled up for large area strain mapping of low-level strain such as that needed in structural health monitoring applications.

Sensor Materials	Gauge Factor	Reference
Silver Nanoparticle Ink (SG, Central Midori)	~2-3* for 3 to 10% ϵ	[5]
	50,000* for 20% ϵ	[5]
Graphite Ink (26-8203, SunChemical)	600-1600	[25]
Carbon Black / Polyacrylic Acid	647 for -0.06 to -0.13% ϵ	[22]
	33 for -0.13% to -0.22% ϵ	
Single-wall Carbon Nanotube Ink	20-90*	[21]
Silver Coated Polystyrene / Polydimethylsiloxane (PDMS)	17.5 for 0-10% ϵ	[23]
	6.0 for 10-60% ϵ	[23]
	78.6 for 60-80% ϵ	[23]
Silver Nanowires / Silver Ink (479SS, Henkel)	21-33	[24]
Silver Ink	28*	[28]
Molybdenum / Poly Butanedithiol 1,3,5-triallyl-1,3,5-triazine-2,4,6(1H,3H,5H)-trione pentenoic Anhydride	20	[29]
Graphite Ink (26-8203 from Sun Chemical)	19.3	[30]
Bi ₂ Ru ₂ O ₇ (8000 Series, DuPont), RuO ₂ , (8241, Heraeus), Bi ₂ Ru ₂ O ₇ (3414, ESL)	2.5-16.5	[31]
1400 Series, DuPont	10-13.4	[32]
7600 Series, DuPont and 3100 Series, ESL	1.2-12.3	[33]
Carbon Black / Multi-wall Carbon Nanotubes / PDMS	12.25	[34]
Carbon Ink (7082, DuPont)	8.8	[10]
RuO ₂ (HS8000 Series, Heraeus)	8.7	[7]
Silver Ink (CI-1036, ECM), Carbon Ink (CI-2051, ECM)	6, 7	[16]
Silver Ink (PF-050, Henkel), Carbon Black Ink (PR-406B, Henkel)	1.85, 4.9-6.4	[14]
Silver Ink (PF-050, Henkel), Carbon Ink (PR-406B, Henkel)	1.74, 4.30	[17]
Multi-wall Carbon Nanotubes / Polyvinyl Alcohol	0.5-3	[13]
Graphite Paste (FTU-165, Asahi Chemical)	2.99	[15]
Carbon Ink (7082, DuPont) / PDMS	0.85, 2.48	[18]
Silver Nanowires / PDMS	0.7	[19]
Aluminum Paste	0.5*	[20]
Carbon Ink (7082, DuPont) / Silver Ink (5028, DuPont) Mixtures	8-66 depending on composition	this work

TABLE I. COMPARISON OF GAUGE FACTORS, AND MATERIALS FOR SCREEN PRINTED STRAIN SENSORS REPORTED IN LITERATURE. *GAUGE FACTORS APPROXIMATED FROM FIGURES.

2.2 Methods and Materials

2.2.1 Strain Gauge Printing

Mixtures of a carbon graphite particle based resistive ink (DuPont 7082) and a silver particle conductive ink (DuPont 5028) were manually screen printed onto 5 mil thick polyethylene terephthalate (PET) sheets using a Gold Print SPR-25 screen printer, 70 durometer (Shore A) squeegee blades, a printing offset of 3 mm, and an approximate printing speed of 3 cm/sec. This printing was done at room temperature ($\sim 20^\circ\text{C}$), with a squeegee angle of ~ 70 degrees. The graphite based ink contains micron size graphite particles dispersed into a proprietary polymer and solvent mixture which exhibits an overall viscosity of 210-260 Pa s, yielding printed films with sheet resistivity of ~ 400 ohm/sq/mil sheet [35]. The silver particle ink contains 5-10 μm silver particles dispersed in a polymer-solvent mixture with an overall viscosity of 15-30 Pa s, yielding printed films typically of 25 μm thickness with sheet resistivity of < 12 milliohm/sq/mil [10,36]. Mixtures of these two inks exhibited similar viscosity during printing such that no changes to the printing process were required. Prior to printing, the substrates were cleaned with isopropanol and then heated to 105°C for two hours to reduce shrinking of the substrates during thermal curing of the inks. Mixtures of the two inks varied from 0 to 100 wt. % carbon ink. The ink mixtures were first printed and then dried for two hours at 105°C . Contact traces to the printed gauges were then screen printed with the same silver ink (DuPont 5028) and subsequently dried for 75 minutes at 105°C . All thermal drying was done in a box oven under 15.6 L/min filtered air flow. The screens for both printed gauges and contact traces had wire diameters of 228.6 μm with 325 wires per inch set at a mesh angle of 45° . The printed sensors had lengths, widths and line widths of 1.06, 0.80, and 0.11 centimeters, respectively with a tension of 27 Ncm. Commercial constantan (Cu-Ni) gauges, KFH-20-120-C1-11L1M2R from Omega, were used for comparison to the printed gauges and had lengths, widths and line widths of 2.007, 0.305, and 0.025 centimeters, respectively. An image of one set of four printed strain gauges and a diagram of the overall printing process is shown below in **Figure 2**.

2.2.2 Electromechanical Measurements

The resistances of the printed and commercial gauges under strain were measured using a B&K 5491B Precision Multimeter which had an uncertainty of $\sim 2\%$ or less for all resistance measurements. Strain was induced

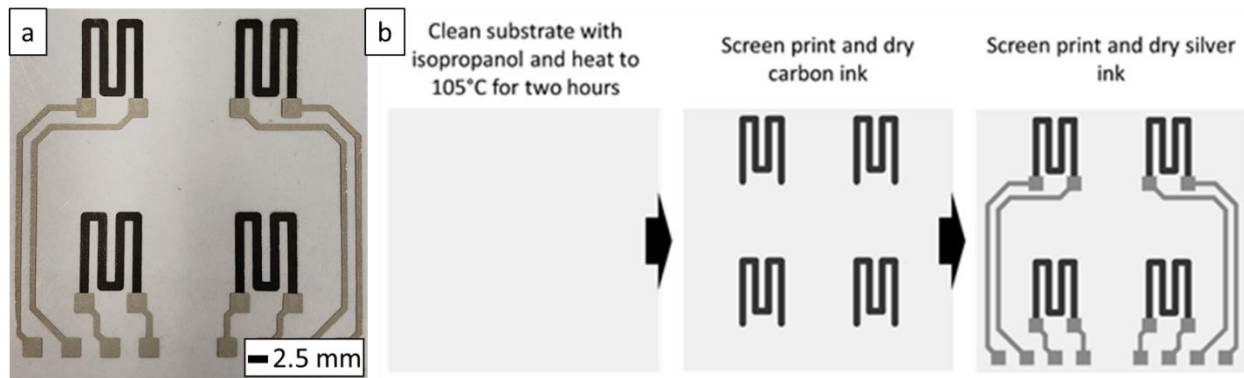


Figure 2. (a) Optical image of one set of four printed strain gauge patterns which used 60 wt.% carbon ink for the gauge elements and (b) a diagram of the strain gauge printing procedure.

by taping the gauges to surfaces with different curvatures, ranging from a flat surface, to a radius of curvature of 0.628". Strain from the curvature was calculated using **Equation 1**. In **Equation 1**, y is the distance from the neutral axis to the top of the gauge layer, assumed to be equal to half the thickness of the substrate (t), plus half the gauge thickness (g). ρ is the radius of curvature of the substrate calculated as equal to the radius of the curved surface plus half the thickness of the substrate (t) and half the thickness of the gauge (g). Here we are assuming that the printed gauges have approximately the same modulus of elasticity as the PET substrate, where the ink is $\sim 5 \mu\text{m}$ thick and the PET is $\sim 127 \mu\text{m}$ thick. Compared to assuming the gauge has negligible effect on the strain, this assumption results in only $\sim 4\%$ increase in the strain. We believe our gauges have a modulus lower than the PET substrate and that this assumption is a slight overestimation of the strain and underestimation of the gauge factors, which serves as a worst-case scenario. A diagram of the strain induced by the curved surfaces is shown in **Figure 3**. Gauge factors were calculated using linear regression to fit the resistance versus strain data according to **Equation 2**, where R_0 is the unstrained resistance, R is the resistance after straining, and ϵ is the strain.

$$\text{Strain from Curvature } (\epsilon) = \frac{y}{\rho} = \frac{\frac{t+g}{2}}{r + \frac{t+g}{2}} \quad (1)$$

$$\text{Gauge factor} = \frac{(R - R_0)/R_0}{\epsilon} \quad (2)$$

2.2.2 Optical Microscopy

After performing electromechanical measurements, optical microscopy images of each ink composition were acquired using a Keyence VHX6000 optical microscope at 500x magnification.

2.3 Results

2.3.1 Strain Gauge Resistance

The average resistance of eight identical gauges printed with the same screen pattern but different compositions are shown in **Figure 4**. The average resistance of these gauges changes only slightly with composition from 0 to 40 wt. % carbon ink. In this region, the conductivity is governed by the silver particles and the resistance remains quite low. However, at around 40 wt. % and higher carbon ink composition, the silver particle density becomes too low to maintain conductivity by itself, and as a result, an abrupt increase in resistance is observed. In this region, conductivity is now supported by the carbon particles of the ink mixture and as carbon content increases further, there is even less contribution of conductivity from the silver particles and the resistance increases linearly

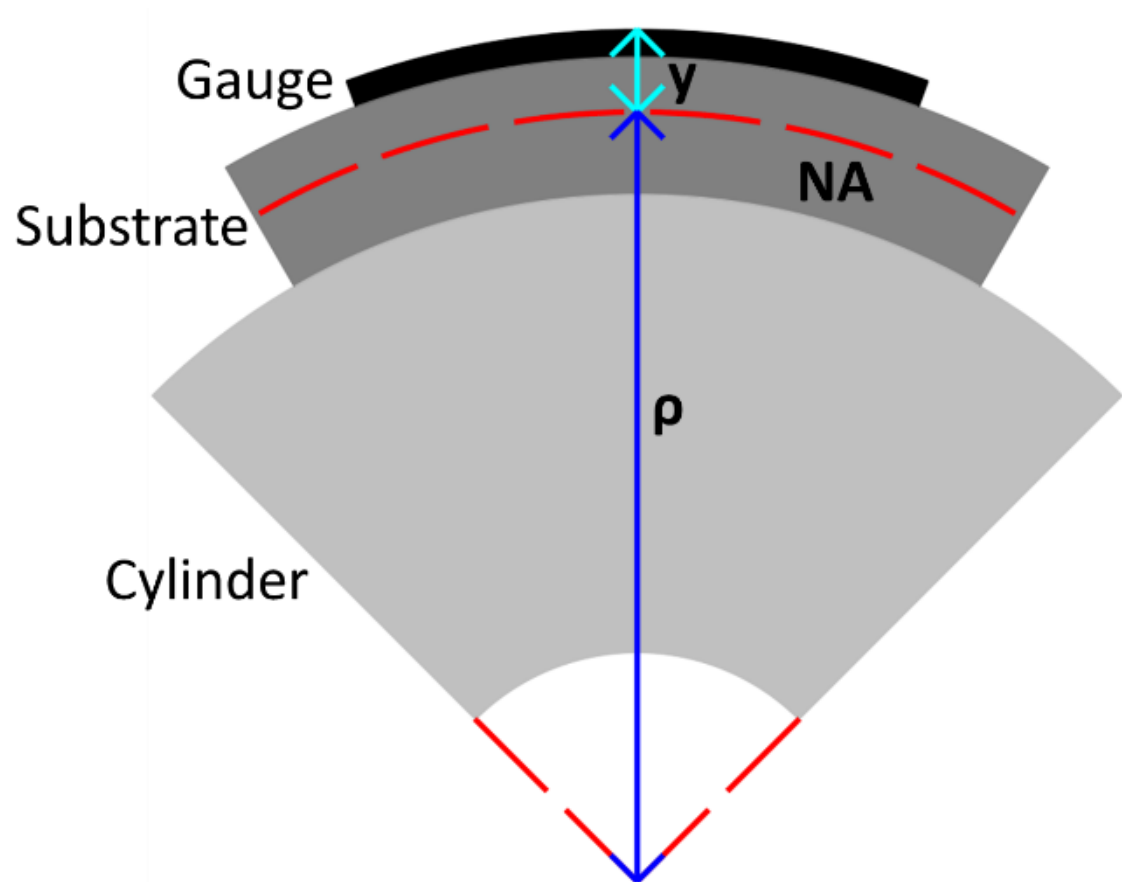


Figure 3. Diagram of strain due to curvature, where y is the distance of the top of the gauge element from the neutral axis, NA is the neutral axis, and ρ is the radius of curvature.

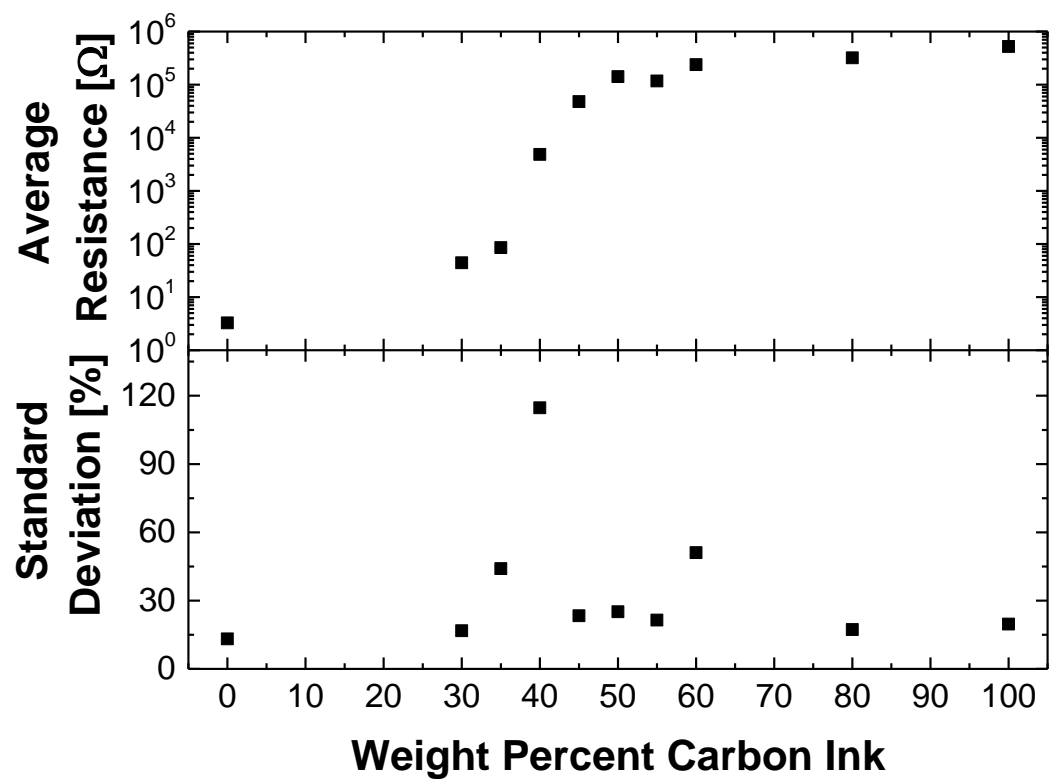


Figure 4. Average resistances versus gauge composition shown as weight percent carbon ink. The bottom portion of the graph indicates the standard deviation of the resistances from eight gauges of each composition.

with composition as typically observed with blending of other resistive inks [35]. At around 40 wt. % carbon ink the percolation threshold is reached where the majority of conductivity appears to transition from the silver particles to the carbon graphite particles pathways. Since the ink mixtures contained highly conductive silver containing and less conductive (resistive) graphite ink components, this change in conductivity from one component to another is not as pronounced as in previous work with Ag/silica composite strain gauges fabricated using a sol-gel method with ultraviolet photoreduction [27]. Nevertheless, the resistance near the percolation is highly sensitive to variation in composition, evident from the slope of this region, where compositional changes of as little as 5 wt.% can change the resistance by as much as factor of 50.

2.3.2 Strain Gauge Sensitivity

A typical plot of relative resistance change versus strain is shown in **Figure 5** below for a few individual strain gauges printed from different ink compositions along with that from a commercial Cu-Ni foil gauge.

The response of these strain gauges is linear out to ~4100 microstrain and large differences in strain response can be seen depending on the composition. In this study, eight gauges of each composition were evaluated (80 gauges in all) and resistance with strain was measured over seven different strains for each gauge. The gauge factor of each gauge was determined by performing linear regression with zero y-intercept constraint on the relative resistance change over strain from curvature for each individual gauge and then averaged over sets of eight identical gauges.

Table 2 summarizes these averaged results along with averaged correlation coefficients from the regression analyses. For comparison, the table also includes previously determined averaged zero-strain resistances. Overall, the gauges were observed to have linear responses to strain within the scatter of the data. Gauge factors with lower averaged correlation coefficients was due to more random scatter in the data. This occurred more with the higher conductive gauges (Constantan foil and 0 wt. % to 35 wt. % carbon ink) and is believed to be due to slight resistance variations with probe contacts which becomes significant when measuring small changes of low resistance values of ~100 ohms or less. In addition to probe contact variability, the low resistance measurements have greater uncertainty from the multimeter measurements (up to ~25 % for Constantan foil and the 0% carbon ink mixture). In principle, the measurements on high silver containing gauges can be improved with alternate probe contacts and detection electronics; however, these gauges are of less interest in the present study due to their relatively low sensitivity and higher current requirements.

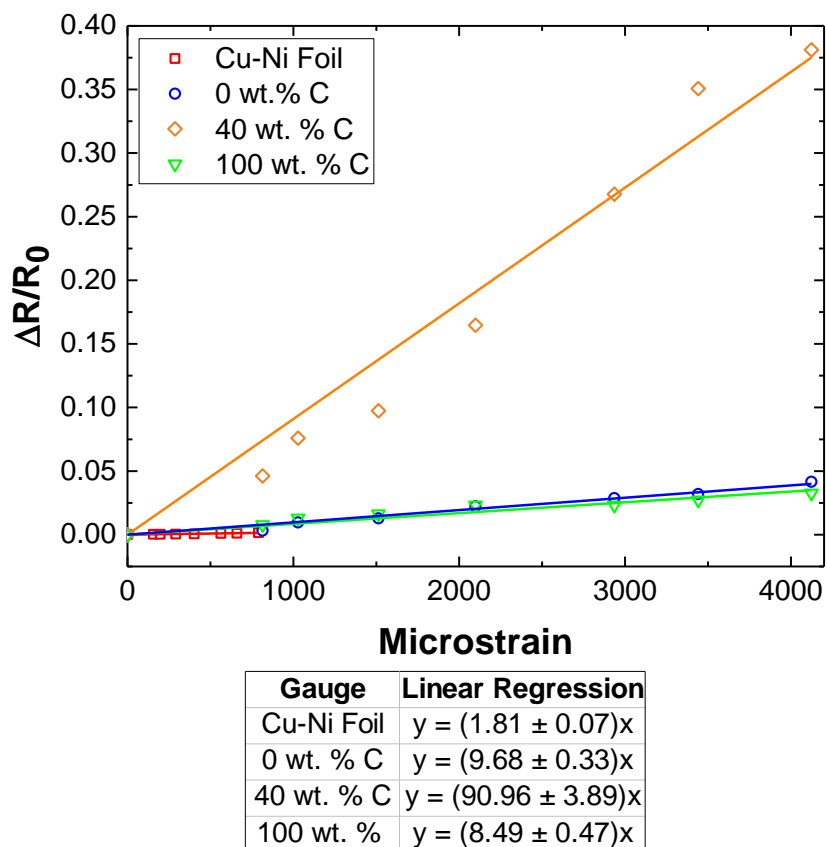


Figure 5. Relative change in resistance versus strain for 0, 40, and 100 wt. % carbon ink gauges along with a commercial constantan strain gauge, with linear regression fits for set of resistance-strain measurements with each gauge using a zero y-intercept constraint.

All Ink Compositions Expressed as % Carbon Ink	Average Resistance with no applied strain [Ω] \pm Std. Dev(%)	Average Gauge Factor \pm Std. Dev(%)	Average Correlation Coefficient
Constantan (Cu-Ni)	120.44 \pm 0.03	2.0 \pm 40.0	0.964
100% C	522,925 \pm 19.6	7.9 \pm 0.6	0.986
80% C	320,775 \pm 17.3	20.8 \pm 21.8	0.993
60% C	237,375 \pm 51.1	42.6 \pm 9.6	0.987
55% C	117,330 \pm 21.4	48.2 \pm 12.7	0.986
50% C	141,519 \pm 25.1	39.5 \pm 42.4	0.987
45% C	47,746 \pm 23.3	58.2 \pm 17.9	0.987
40% C	4,844 \pm 114.7	65.9 \pm 45.8	0.959
35% C	85.1 \pm 44.0	8.6 \pm 18.0	0.856
30% C	44.4 \pm 16.7	5.8 \pm 67.2	0.700
0% C	3.3 \pm 13.2	10.9 \pm 39.9	0.878

TABLE 2. AVERAGE RESISTANCES, AVERAGE GAUGE FACTORS AND AVERAGE CORRELATION COEFFICIENTS FROM LINEAR REGRESSION ANALYSIS FOR EIGHT GAUGES OF EACH COMPOSITION AND FOUR COMMERCIAL GAUGES (CONSTANTAN (CU-NI) GAUGES, KFH-20-120-C1-11L1M2R FROM OMEGA).

To further illustrate ink mixture composition influence on gauge strain sensitivity, the average gauge factors are plotted over ink composition along with their relative standard deviations and illustrated in **Figure 6** below. Only slight change in sensitivity was observed between 0 and 35 wt. % carbon ink; however, a significant increase in gauge factor from 8.6 to 65.9 was observed between the narrow composition range of 35 to 40 wt. % carbon ink. At 40 wt. % carbon ink, it is believed that the conductivity is still dominated by the silver particles but with minimal required volume density and so under strain, large changes in resistance are observed as the volume density of conducting silver particles decrease below its percolation threshold and the conductivity becomes dominated by the more abundant graphite particles in the carbon ink. Above 40 wt. % carbon ink, the sensitivity decreased approximately linearly with increasing carbon content to a gauge factor of 7.9 for the pure carbon ink gauges. It is interesting to note that the gauge factor of 7.9 observed here for the 100 wt % carbon ink is quite similar to the observed gauge factor of 8.8 using the same carbon ink but different strain gauge dimensions [10]. In this composition region (above 40%) there is a gradual decrease of strain sensitivity with increasing carbon ink content. Based on these results, it appears sensitivity of a printed carbon ink strain gauge can be enhanced by factor of 7 – 8 by the simple ink mixing with a miscible silver conducting ink. Based on percolation theory, much greater

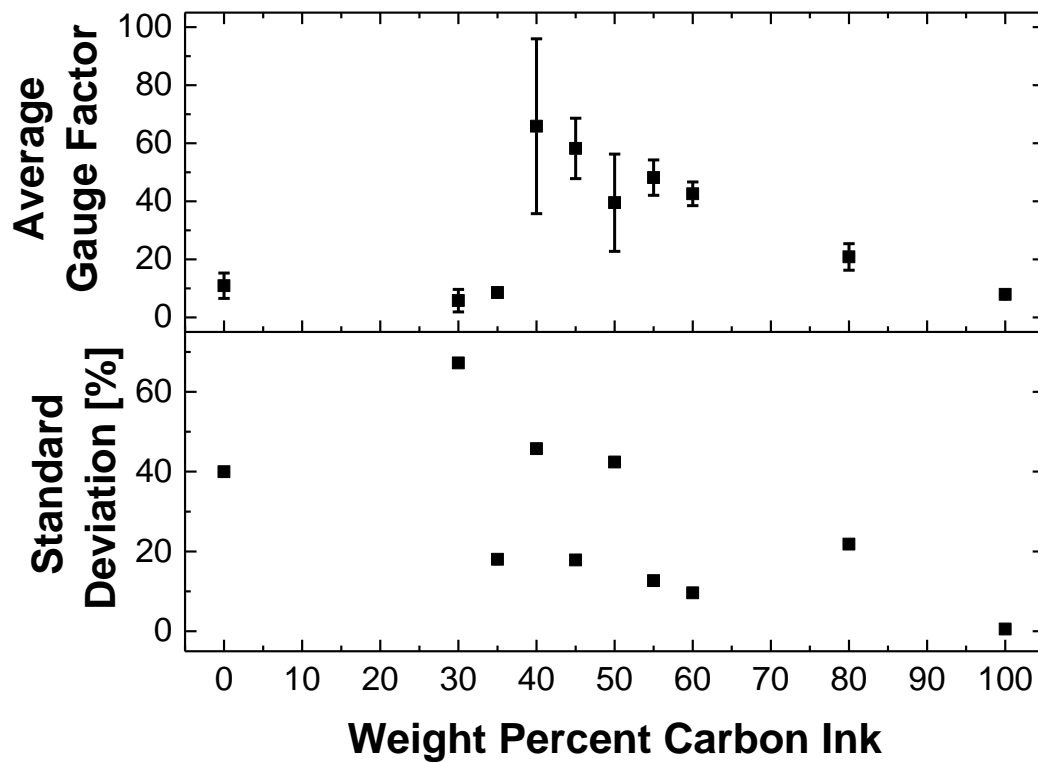


Figure 6. Average gauge factors versus gauge composition shown as weight percent carbon ink. Error bars and the bottom portion of the graph indicate the standard deviation of the gauge factors from eight gauges of each composition.

sensitivity enhancement is possible as one approaches closer to the percolation threshold and have conductive particles in a more insulating matrix. However, there is a practical limitation to consider here as well and that is, as one approaches percolation threshold, the manufacturing reproducibility of the gauges becomes much more stringent on fabrication process controls of ink mixing accuracy and consistency of the printing process itself.

In this work there is a more gradual change in strain sensitivity with composition since conductive inks are blended with resistive ink rather than insulating inks. With this approach, the control of gauge ink composition becomes less critical and more readily achievable than in other works where insulating and conducting composites are used [27].

To examine the compromise between repeatability and enhanced sensitivity together, the standard deviations of averages are examined in greater detail in the next section.

2.3.3 Strain Gauge Variability

An important factor in strain gauges particularly in large area strain mapping is the consistency of sensitivity of individual gauge elements in the array. This aspect, although critically important in strain mapping, is often not well addressed in prior studies involving highly sensitive strain gauges based on composite materials near-percolation threshold. As seen in previous section, sensitivity is significantly enhanced when approaching the percolation threshold; however, along with that enhancement is the need for more stringent control of the strain gauge composition and printing process. That is to say, there is a trade-off between sensitivity and reproducibility of fabrication. To demonstrate this further based in this work, standard deviations from the average of eight printed gauges are determined for each of the different ink compositions as a means of assessing variability of both resistances and gauge factors of the printed gauges. In Figure 3, the standard deviations of average resistance measurements appear to peak sharply near the percolation threshold of about 40% C ink. Note how the resistance variation remains around 20% for most of the ink compositions except at the percolation threshold region. This is consistent with our previous work [10] where strain gauges were printed from 100% carbon containing ink only. The resistance variation of the printed gauges is believed to be due to thickness variation as printed linewidths showed far less variation while the sensitivity variation is thought to be result of differences in particle distribution in the ink mixtures [10]. Optical microscopy images of the ink compositions are shown in **Figure 7**. These images were taken after straining the gauges and no damage in the microstructure was noted. At high carbon concentrations and for pure silver ink, the gauges appear well homogenized. However, for ink mixtures with carbon ink

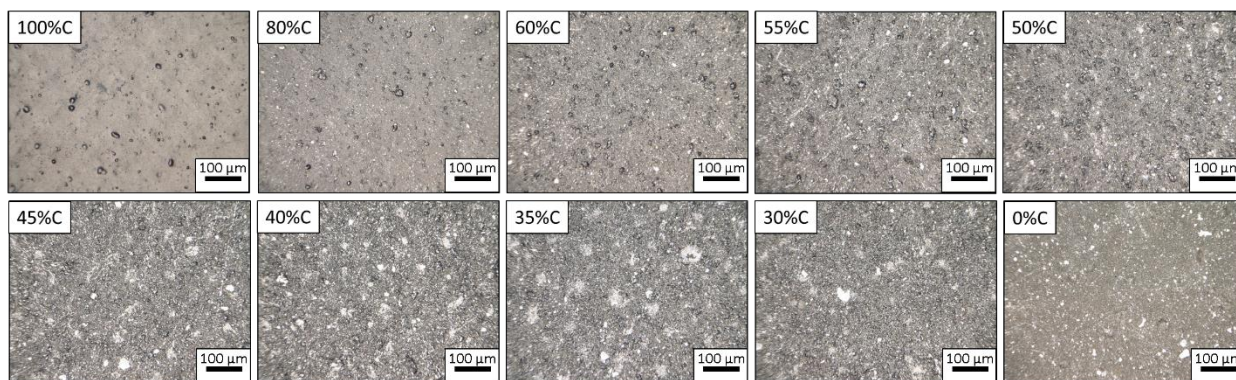


Figure 7. Optical microscopy images of the ink that composes the gauge element of our strain gauges at 500x magnification. The text in the upper left hand corner of each image refers to the weight percent carbon ink used.

concentrations between 30 and 45 wt.%, agglomerates of silver ink on the order of tens of microns in diameter are visible. Thus, the main sources of fabrication variation in this work are believed to be difficulties in homogenizing ink mixtures with high silver content with these two specific inks, and repeatability of printing, namely printing speed and screen deflection.

In comparison, the standard deviations of averaged gauge factors shown in **Figure 6** appear to increase more gradual and peak for the ink mixture of lower carbon ink content of ~30%. However, this difference needs be viewed with care as lower resistance measurements have greater measurement uncertainties which contribute significantly more for gauge factor determination. Another additional uncertainty at the low carbon ink compositions is that there may likely be more limited miscibility of these two inks. For the low carbon ink compositions striations were visible in the ink during printing and agglomerates of silver ink were visible in microscopy images as shown in **Figure 7**. This leads to less uniformity of the ink mixture resulting in differences in particle distribution and greater variability in the measured gauge factors. None the less, the main points to realize in the comparing these results is that gauge factor variability will maximize near the percolation threshold and there is a practical limit how much sensitivity enhancement one gains with the ink mixtures which will be defined by the degree of process control for ink blending and printing processes. Based on these studies, it appears better to formulate ink mixture on the higher resistance side of the percolation threshold. Upon further inspection of the data in the bottom section of **Figure 6**, it appears that the gauge factor can be increased to around 60 with the simple blending of Ag ink and still attain standard deviation of about 20% or less. It is expected that with more automated process equipment providing tighter control of ink formulation and printing, higher sensitivity would be achievable.

2.4 Conclusions

In this study, we present multiple replicate sets of fully printed strain gauges with enhanced sensitivity by preparing resistive-conductive ink mixtures near the percolation threshold and show how this sensitivity enhancement influences printing repeatability. Gauge factors as high as 66 were measured for gauges with mixed ink composition nearest to the percolation threshold, and in comparison, gauge factors of 8 and 11 were observed for gauges prepared from pure carbon and silver based inks, respectively. While the largest gauge factor measured was near the percolation threshold of 40 wt. % carbon ink, there is significant variation in gauge response near this region of 46% which may limit usefulness in practical applications. Within a constraint of 20% standard deviation

of response, gauge factors of 43 to 49 were measured using 55-60 wt. % resistive carbon ink mixed into a conductive silver ink. It is anticipated less variation can be achieved with a more automated printing process. By blending resistive and conductive inks together, the change in sensitivity is more gradual and thus more process controllable for better optimization of sensitivity enhancement and printing repeatability for a particular application.

CHAPTER 3

Screen Printed Carbon Strain Gauges, Strain Gauge Arrays, and Screen Printed Transistors

(Previously published as Joshi, S., Bland, S., DeMott, R., **Anderson, N.**, & Jursich, G. (2017) “Challenges and the state of the technology for printed sensor arrays for structural monitoring.” *SPIE: Industrial and Commercial Applications of Smart Structures Technologies*. 10166, 101660H. and as Zhang, Y., **Anderson, N.**, Bland, S. Nutt S., Jursich, G., & Joshi, S. (2017) “All-printed strain sensors: Building blocks of the aircraft structural health monitoring systems.” *Sensors and Actuators A: Physical*. 253, 165-172)

3.1 Introduction

As aviation technology advances so does the need for low-cost, large area structural health monitoring systems for maintenance of existing in-service aircraft, development of newer prototype vehicles and new aircraft. Two specific applications for structural health monitoring would be in operation of unmanned air vehicles (UAVs) and more cost-effective maintenance of aircraft in the field, so that maintenance schedules can be based on condition of critical components of aircraft rather than time-usage intervals. More specifically, Naval Air Systems Command (NAVAIR) expressed interest in real-time spatial strain monitoring for unmanned aerial vehicles (UAVs) and to store such information in an on-board computer system for data logging and establishing condition-based maintenance (CBM) of their aircraft. This requires a strain sensor monitoring system that is low-cost and flexible. While strain sensing arrays of various materials have been prepared previously, they have been prepared primarily using conventional microfabrication processes [37–41]. These processes limit the scalability, increase the cost and limit the flexibility of the arrays. Furthermore all-printed arrays of strain gauges or strain gauges and transistors have not been reported in literature. Therefore, the focus of this work was on using low-cost printing processes to fabricate and demonstrate an advanced thin-film, flexible strain sensing system. This system could easily be applied to contoured surfaces of critical structural components of aircraft and yet easily interfaced with existing on-board computer systems. A diagram of the proposed system is shown in **Figure 8**.

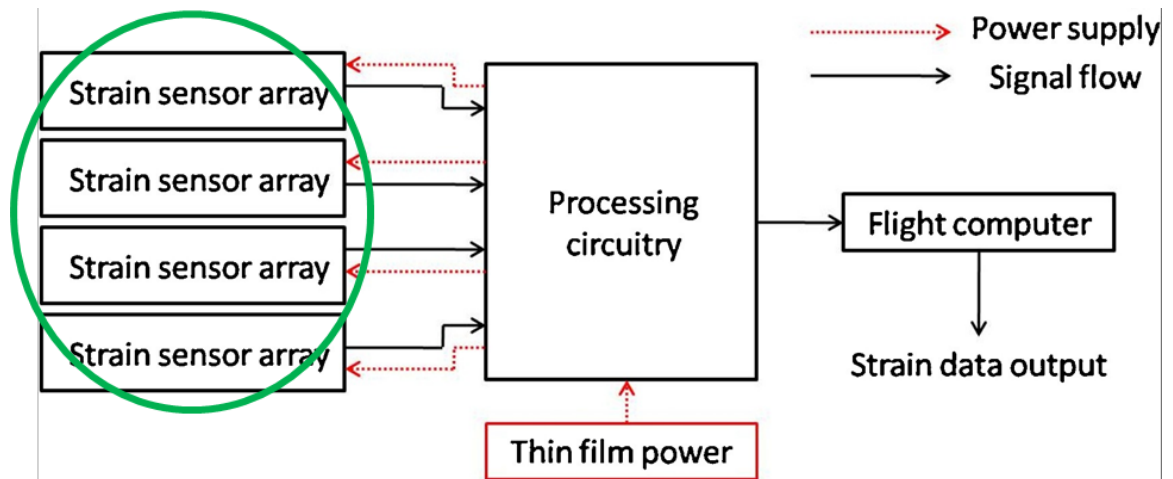


Figure 8. Diagram of the proposed system for structural monitoring of aircraft.

The most critical component of the strain sensing system is the sensor itself. These sensors are devices capable of reproducible changes in either electrical or optical characteristics in response to mechanical strain, which for one dimension is represented by the ratio of $\Delta L/L$, where ΔL is the change in length from an applied force and L is the unstrained length. In the case of electrical resistance sensors (or piezo-resistive sensors), the sensitivity is expressed in terms of gauge factor (GF), defined as fractional change of resistance over strain or $(\Delta R/R)/(\Delta L/L)$.

As to sensor materials, many innovative technologies and functional materials have been explored over the last several years to develop strain sensors with low-cost printing techniques. Many of the screen-printed gauges have been presented in the literature review in the previous chapter (**Table I**). However, printed gauges have not been fabricated into large arrays suitable for structural health monitoring. Among the classes of functional materials there are metals such as Ag, Au, various alloys, semiconductors such as Si, ITO, Ge, and dielectric-metal composites. All of these have been examined as strain sensors. Of these different classes of sensor materials, metals typically have the lowest strain sensitivity but low transverse strain sensitivity and relatively low temperature dependence. Whereas semiconductors typically have the highest sensitivity to strain but typically have the highest temperature dependences and are rigid unless fabricated into delicate, extremely thin sub-micron thicknesses. Lastly, resistive strain sensors made of dielectric-metallic composites can have high sensitivity to strain depending on the composite composition while being easily printable, and have a long, mature manufacturing history in printed electronics.

The complexity of collecting numerous signals from many sensor elements in an array over a large area necessitates either very fine conductive lines or signal multiplexing electronics that need to be printed on a flexible substrate or structure. For this, transistors or diodes need to be implemented within the strain sensor array. For transistors, there are two fabrication approaches; one is the printing of transistors using conductive, semiconductive, and dielectric inks which is the most ideal, low-cost manufacturing approach. While an alternate hybrid approach is to use small silicon transistors directly bonded onto the screen-printed sensor array. A literature table of printed transistors is shown in **Table III**. While some of the articles included in this table prepared transistors entirely through printing methods, printing repeatability, large arrays of transistors, and the effect of strain and fatigue were not well studied. From the literature surveyed we selected the methods of Xuan Cao et al. [42] as the basis for our transistor printing as the performance of their printed transistors met the requirements of the processing circuitry

(on-currents $> 10^{-6}$ A, on/off current ratios $> 10^3$) and little change in transistor performance with bending was reported.

CYEPL	cyano-ehtylpullulan (dielectric / insulator)
PVP	poly(4-vinylphenol) (dielectric / insulator)
TIPS Pentacene	6,13-bis(triisopropyl-silylethynl) pentacene (active layer / semiconductor)
BTO/PPMA	high-k barium titanate nanoparticles and poly(methyl methacrylate) (gate dielectric)
BTO	high-k barium titanate nanoparticle ink (gate dielectric)
s-SWCNT	semiconductor single walled carbon nanotubes (active layer / semiconductor)
m-SWCNT	metallic single walled carbon nanotubes (contacts)
PEDOT:PSS	poly(3,4-ehlenedioxythiophene):poly(styrenesulfonic acid) (electrodes)
PTPA2	amorphous poly(tri-phenyl-amine) (active layer / semiconductor)
P105/PMMA	proprietary butylene copolymer/poly(methyl methacrylate) (dielectric / insulator)
PEN	planarized polyethylene nappthalate (Substrate) - Dupont
pBTTT	poly(2,5-bis(3-tetradecylthiophene-2-yl)thieno[3,2-b]thiophene) (semiconductor)
P3HT	poly(3-hexyl-thiophene)/toluene (semiconductor)
PES	polyestersulfone
P-PVP	photo-definable poly(4-vinylphenol)
PVA	poly(vinylalcohol)
PL-C	parylene-C
PS	polystyrene
AlNd	aluminum neodymium alloy
Deposition Acronyms	
PE-CVD	plasma-enhanced chemical vapor deposition
RF PE-CVD	radio-frequency excited plasma enhanced chemical vapor deposition
EP	electrochemical polymerization
ID	immersion deposition
PL	photolithography

TABLE III. SUMMARY OF PRINTED THIN FILM TRANSISTOR LITERATURE WHERE REFERENCES FOUR THROUGH NINE WERE CONSIDERED ALL-PRINTED.

Here we report on strain gauges, transistors and strain gauge arrays prepared via screen printing and characterization of the materials and devices. Strain gauges were found to have linear responses to strain with longitudinal gauge factors of ~ 8 for up to at least 1.1% strain. Additionally, the strain gauges were found to exhibit the same linearity and sensitivity after 10^5 cycles at 0.2% strain. Furthermore, these gauges were found to have void-free microstructures indicating their suitability for strain applications. Due to the low resistance and fine line widths required for the strain gauge arrays, a less resistive carbon ink was used.

$\sim 8'' \times 10''$ arrays of 64 strain gauges with locations for 192 transistors and approximately 500 dielectric cross-over regions were prepared on polyimide substrates. Through optimization of the printing process, resistance tolerances of the gauges in the arrays were reduced to $\sim 20\%$. The gauges exhibited longitudinal gauge factors of

~19 for up to at least 0.25% strain and the ink showed a temperature coefficient of resistance of $\sim 0.26 \times 10^{-3} \text{ K}^{-1}$. Similar to the previously prepared carbon gauges, these also showed void-free microstructures.

Arrays of 55 transistors composed of commercial silver and barium titanate inks and semiconducting single-walled carbon nanotubes (S-SWCNTs) were prepared on PET and alumina coated PET substrates. The alumina coated substrate was found to increase adhesion of the carbon nanotubes thereby increasing the on-current of the transistors by $\sim 10,000$. However, the off-current also increased and the overall on/off current ratios decreased by approximately a factor of 2. The effect of strain and fatigue on the microstructure and performance of the transistors was also examined. While transistors with the best performance were prepared on alumina coated PET, this alumina coating failed under strain, damaging the transistors. On the PET substrate, transistors were found to debond in the channel region likely due to poor adhesion of the carbon nanotubes and the inks printed on top of the carbon nanotubes. This debonding led to damage of the transistors under both strain and fatigue. Additionally, the effect of some process changes in the transistor performance and printing reliability are presented.

3.2 Methods and Materials

3.2.1 Screen Printing of Carbon Gauges

The first ink selected for the sensor element of the gauges was DuPont 7082 carbon ink and the ink selected for the contacts of the gauges was DuPont 5028 silver ink. All screen printing was done using a manually operated Gold-Print SPR-25 screen printer. Strain gauges were deposited using 70 durometer (Shore A) squeegee blades, and a 304 stainless steel screen pattern with an emulsion thickness of 0.005 inches, a mesh angle of 45 degrees, 325 wires per inch, and a wire diameter of 0.009 inches. These strain gauges were printed onto 5 mil PET film (McMaster-Carr) that had been preheated at 105°C for two hours in a laboratory oven to prevent dimensional changes during thermal curing of the ink. The gauge layer was dried for 120 minutes at 105°C to obtain a stable resistance from the gauge. Shorter drying times for this ink resulted in resistance values gradually changing at ambient and elevated temperatures. The contact layer was dried for 75 minutes at 105°C in order to maintain a stable resistance. In this case, resistances were found to decrease by more than 10% with shorter drying times indicating insufficient drying time.

3.2.2 Screen Printing of Strain Gauge Arrays

A 64-element strain sensor array was fabricated in four layers via screen printing on 2 mil thick polyimide film (DuPont Kapton HN). The sensor components were printed using a resistive, graphite based ink (DuPont 7102C). The horizontal and vertical traces were printed using a highly flexible silver-based ink (Conductive Compounds Ag-530), and the insulator layer was printed using a UV-curable dielectric ink (Conductive Compounds UV-2530). To reduce the possibility for short circuits at the cross-over regions, three layers of the dielectric ink were printed with partial curing between prints. The carbon ink was dried at 105°C for two hours and the silver ink was dried at 105°C for 75 minutes. Thirty minutes into the drying process, the metallic Ag flakes in the silver ink were flattened by rolling a 2 kg metal cylinder twice across the partially dried ink. The insulator layers were cured with a custom-built UV curing system where the first two layers were each cured for 30 minutes and the third layer was cured for 40 minutes. All thermal drying and UV curing of inks were done with addition of 17.8 L/min filtered airflow in an enclosed chamber. After screen printing, discrete bare-die transistors were attached using silver conductive epoxy which is then dried at ~120°C. A diagram of the fabrication process is shown in **Figure 9**.

3.2.3 Screen Printing of Transistors

Arrays of 55 transistors were screen printed onto mostly 5 mil thick, non-coated PET (McMaster-Carr) and in few cases 5 mil thick Al₂O₃ coated PET (Mitsubishi) substrates. A diagram of the printing procedure is shown in **Figure 10** and the dimensions of the channel regions of these transistors are given in **Table IV**. Prior to printing,

Transistor Row	Channel Length [μm]	Channel Width [μm]
1	75	1,000
2	100	1,000
3	125	1,000
4	150	1,000
5	200	1,000

TABLE IV. CHANNEL DIMENSIONS FOR THE ARRAY OF SCREEN-PRINTED TRANSISTORS

the substrates were cleaned with isopropanol and additionally uncoated PET substrates were heated for two hours at 105°C. Printing was done using 80 durometer (Shore A) squeegee blades and screen patterns with mesh angles of 45°, 400 wires per inch, wire diameters of 0.0007 inches, and emulsion thicknesses of 0.0002 inches. The transistors were printed mainly in top-gate configuration where the semiconductor was printed first directly on the substrate followed by source and drain electrodes, gate dielectric layer and the gate electrode last. The semiconductor ink that was primarily used was IsoSol-S100 which is a 99.9+% semiconducting single walled carbon nanotubes (S-SWCNTs) dispersion in Toluene (NanoIntegris). This solution was deposited onto the substrate by either immersion or drop casting. For immersion, the substrate was placed in the solution for up to 120 minutes, baked at 75°C for 15 minutes, rinsed with toluene and baked at 100°C for an additional 15 minutes. For drop casting, 0.5 μ l of solution was dropped onto the channel regions, baked at 75°C for 15 minutes, rinsed with toluene and baked at 100°C for an additional 15 minutes. The source and drain electrodes were printed using Ag-530 silver ink (Applied Ink Solutions) which was dried for 10 minutes at 105°C before being mechanically flattened using a 2-kg metal cylinder and dried an additional 65 minutes. The gate dielectric layer was printed using two layers of the barium titanate ink with a 10 minute 105°C thermal cure between layers and 75 minute 105°C dry after printing the second layer. The gate was printed using undiluted silver ink and was dried for 75 minutes at 105°C dry.

Throughout this project numerous transistors were printed, and the printing procedure was modified numerous times to try to improve the transistor performance and repeatability. Two important modifications to the printing procedure were dilution of the silver ink used for the source and drain electrodes, and dilution of the barium titanate ink used for the gate dielectric. These inks were used with many different dilutions in order to identify optimal dilution so as to make the print thicknesses as thin as possible without risk of degrading print quality. After many trials, 15 weight percent (wt.%) dilution for source and drain electrodes and 10 wt.% dilution for the gate dielectric were identified as the most optimal. For both inks, the dilution was done with diethylene glycol ethyl ether acetate (Alfa Aesar).

Another important printing process modification was the use of different surface treatments of the substrate prior to printing. The surface treatments tested in this work were oxygen plasma etching of the substrate and surface treating the substrate with 0.01% w/v poly-l-lysine in deionized water (Ted Pella). Oxygen plasma treatment was

done for uncoated PET films using a Plasma Etch PE-50 benchtop plasma cleaning system using a gas flow rate of 10 ccm, pressure of 200 mTorr, power of 100 Watts, and a treatment time of 5 minutes. Poly-l-lysine was deposited by pipetting approximately 5 mL of the solution onto the substrate, waiting for 5 minutes, returning the solution to the container, rinsing the substrate with deionized water and drying the substrate with nitrogen.

Yet another printing process modification that was investigated was increasing the amount of post-rinsing of the S-SWCNTs deposited onto the PET films. The amount of rinsing was first done with 5 mL pipette aliquots for a total of 20 mL of toluene followed by more extensive rinsing with 50 mL pipette aliquots for a total of 250 mL additional toluene. In these rinsing procedures, the relative amount of S-SWCNTs remaining on the substrate was determined by resistance measurements as the less S-SWCNTs remain, the higher the resistance.

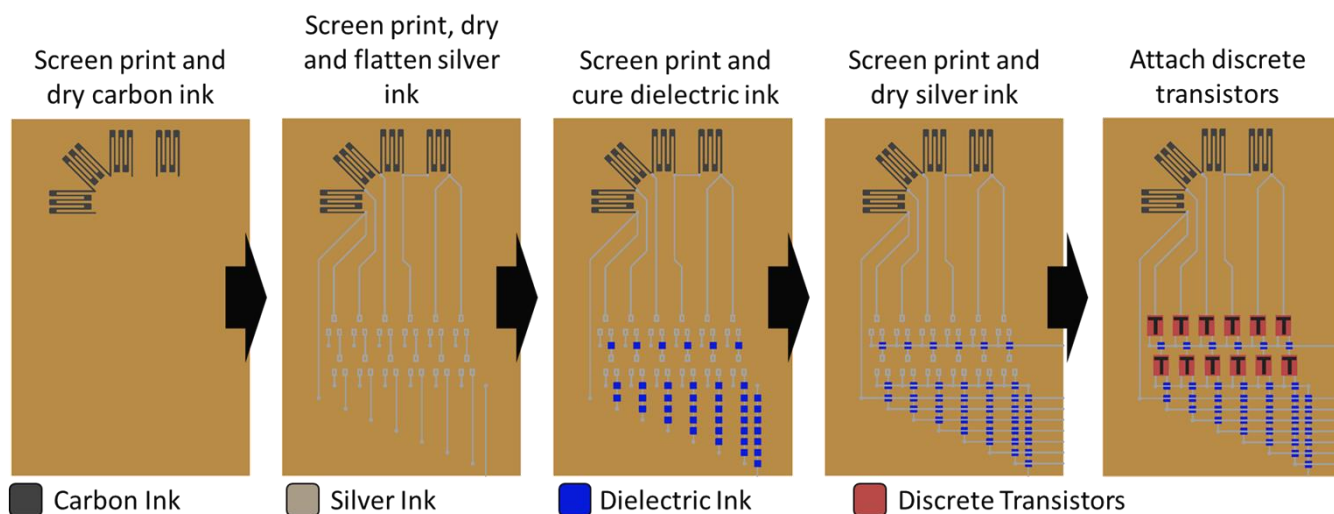


Figure 9. Diagram of the screen-printing procedure for preparing strain gauge arrays. The substrate used was 2-mil thick polyimide, Kapton HN, from DuPont, the carbon ink used was DuPont 7102C, the silver ink used was Conductive Compounds Ag-530, the dielectric ink used was Conductive Compounds UV-2531, and the discrete transistors were attached using silver epoxy.

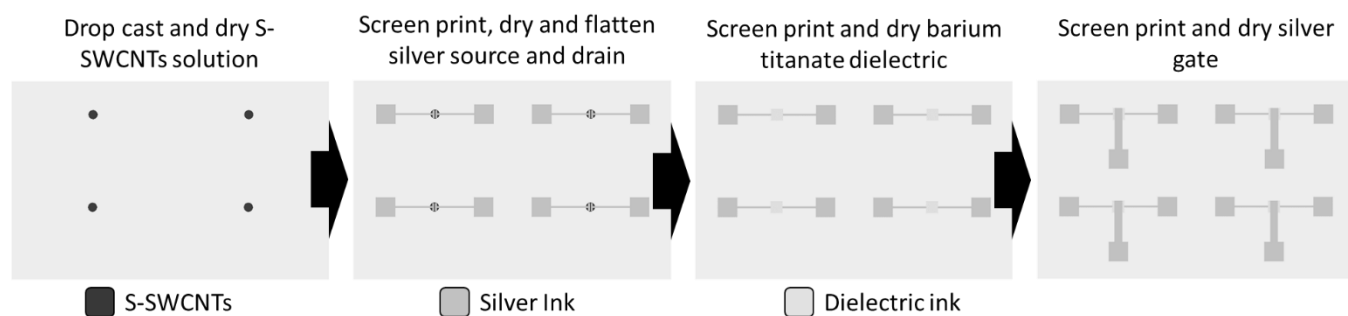


Figure 10. Diagram of the transistor printing process. The S-SWCNT solution used was IsoSol-S100, 99.9+% semiconducting CNTs in toluene (NanoIntegris), the silver inks used were DuPont 5028 and Ag-530 (Conductive Compounds), and the barium titanate dielectric ink used was BT-101 (Conductive Compounds).

3.2.4 Strain Measurements

For the strain gauges, tensile strain was applied quasi-statically at a constant rate of 10^{-4} s^{-1} to printed gauges that had been cut into dog-bone shapes as also shown in **Figure 11**. Applied strain was measured via the displacement transducer on the micro-tensile module and resistance change was measured using a digital multimeter. This same apparatus and setup were used for straining transistors.

For the strain gauge arrays, resistance of the gauges was measured using a B&K 5491B Precision Multimeter under strain-free and induced strain conditions. Strain was induced by taping the gauges to surfaces of different curvatures ranging from a flat surface to a radius of curvature of 1.255". Strain from the curvature was calculated using **Equation 1** where y is the distance from the neutral axis to the top of the gauge layer, assumed to be equal to half the thickness of the substrate (t), plus half the gauge thickness (g). ρ is the radius of curvature of the substrate calculated as equal to the radius of the curved surface plus half the thickness of the substrate (t) and half the thickness of the gauge (g). Here we are assuming that the printed gauges have approximately the same modulus of elasticity as the polyimide substrate, where the ink is $\sim 5 \text{ }\mu\text{m}$ thick and the polyimide is $\sim 50.8 \text{ }\mu\text{m}$ thick. Compared to assuming the gauge has negligible effect on the strain, this assumption results in only $\sim 10\%$ increase in the strain. We believe our gauges have an elastic modulus lower than the polyimide substrate and that this assumption is a slight overestimation of the strain and underestimation of the gauge factors, which serves as a worst-case scenario. Gauge factors were calculated from linear regression of the slopes of fractional resistance change versus strain data according to **Equation 2** where R_0 is the initial resistance, R is the resistance after strain, and ϵ is the strain.

$$\text{Strain from Curvature } (\epsilon) = \frac{y}{\rho} = \frac{\frac{t+g}{2}}{r + \frac{t+g}{2}} \quad (1)$$

$$\text{Gauge factor} = \frac{(R - R_0)/R_0}{\epsilon} \quad (2)$$

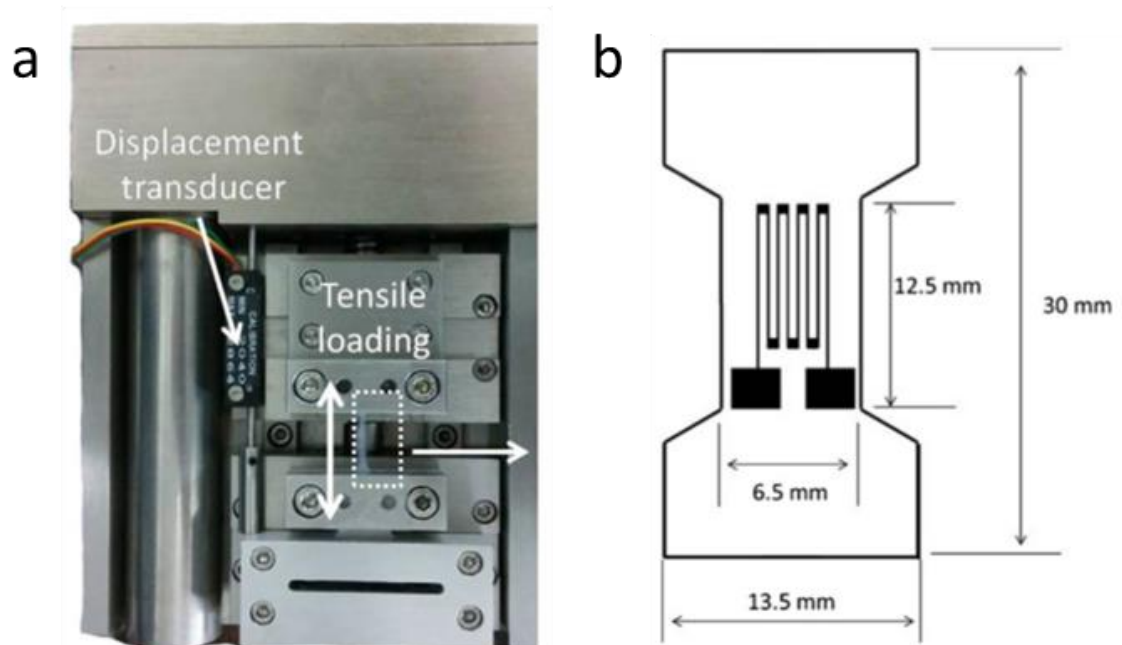


Figure 11. (a) Micro-tensile measurement apparatus and (b) geometry of dog-bone specimens for tensile testing of carbon strain gauges.

3.2.5 Fatigue Measurements

Sensor reliability versus cyclic loading was tested using a fatigue testing frame (Instron 8500) with a cyclic load frequency of 5 Hz. Fatigue testing was done with a four-point bending setup with both printed sensors and commercial foil gauges attached to an aluminum beam as shown in **Figure 12**. The thickness to length ratio of the aluminum beam in this setup was small enough to assume that bending was uniform between two inner adjacent bending pins. The applied strain in this case was determined in real time using commercial reference gauges. This same setup was used for fatigue testing of printed transistors.

3.2.6 I-V Measurements of Transistors

Current-voltage (I-V) characteristics of transistors were obtained using a three-probe system connected to a Keithley 6517A electrometer/high resistance meter and a Keithley 230 programmable voltage source and controlled by a LabVIEW (National Instruments) virtual instrument. A diagram of this testing setup is shown in **Figure 13**.

3.2.7 Microscopy and Profilometry

Optical profilometry was performed using a Bruker Contour GT-K optical profilometer in vertical scanning interferometry mode with 5x magnification. Scanning electron microscopy (SEM) was done using a field emission SEM (JEOL JEM 7001F) operated at 20 kV. Cross sectional samples were prepared for SEM measurements using an ion polisher (JEOL IB-09010CP). Optical microscopy was performed using a Keyence VHX-600e stereo digital light microscope.

3.3 Results

3.3.1 Screen Printed Carbon Strain Gauges

Serpentine-shaped strain gauges were printed with different gauge dimensions. The printed gauges were compared in terms of resistivity, sensitivity (gauge factors), and consistency of printing. **Figure 14** shows several of the different designs which were screen printed with resistive carbon-based inks on PET substrates. Although line widths as thin as 125 μm can be screen-printed, gauges with larger line widths were printed with much better

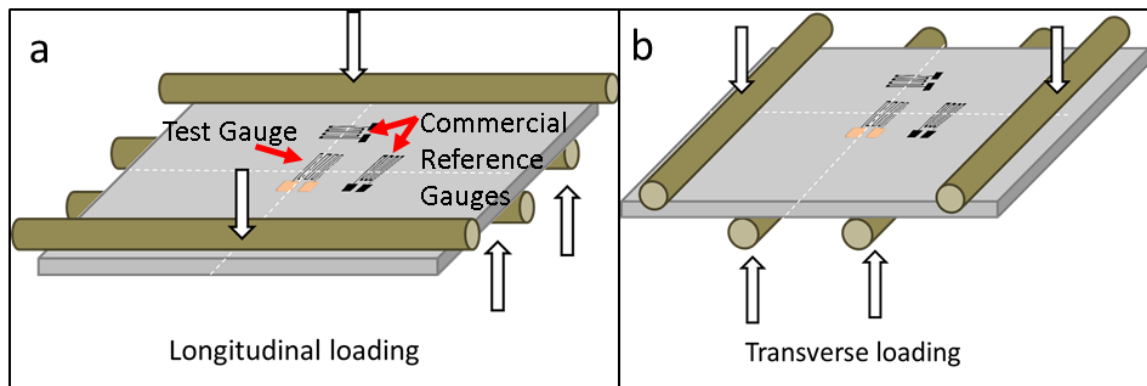


Figure 12. Diagram of (a) longitudinal and (b) transverse loading applied with four-point bending for fatigue testing of printed strain gauges.

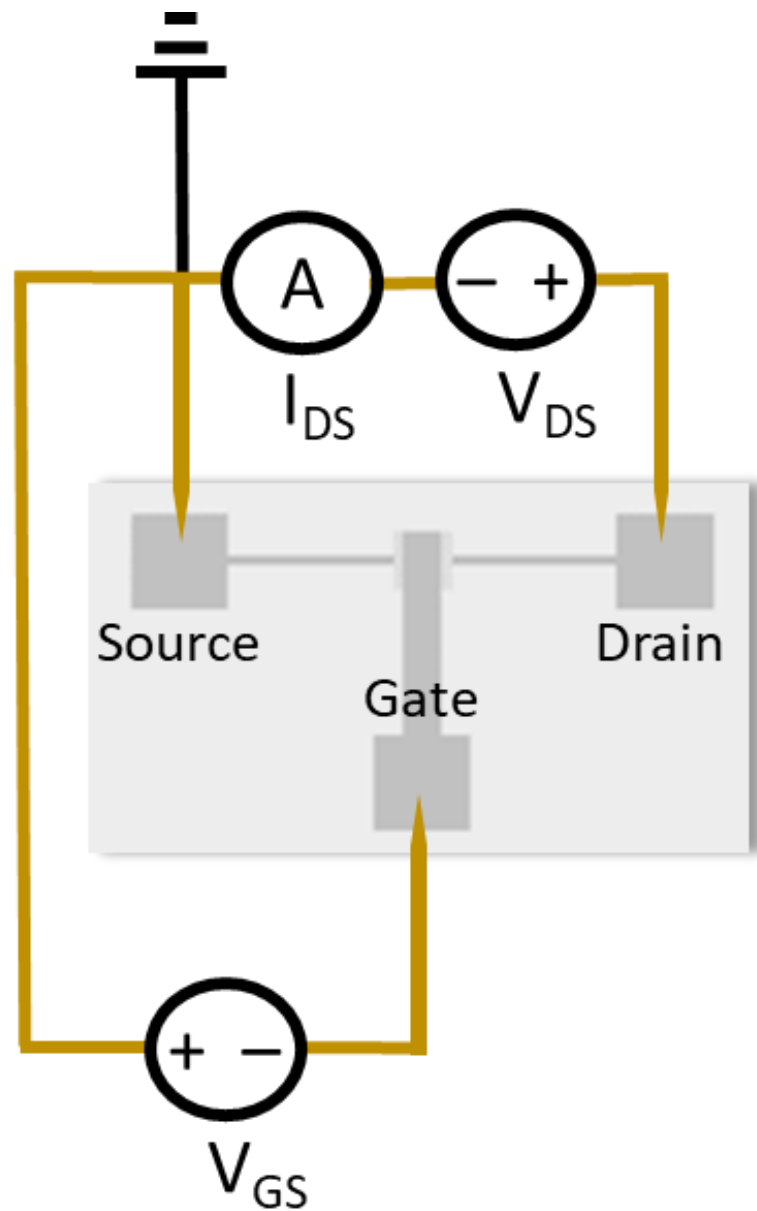
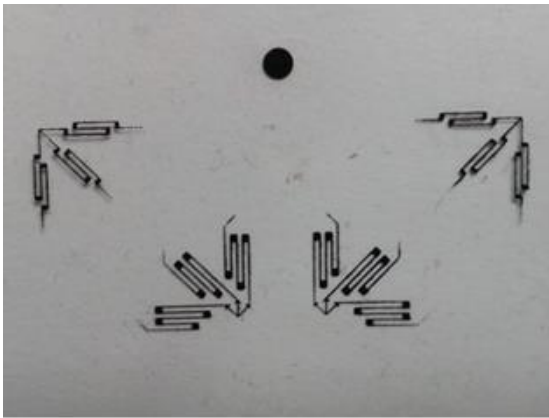
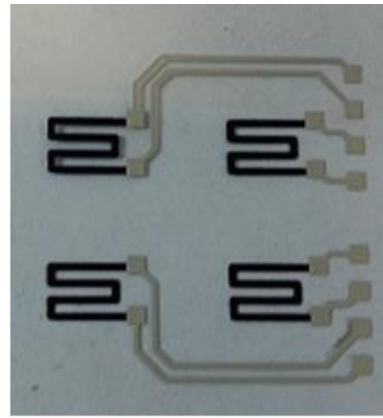


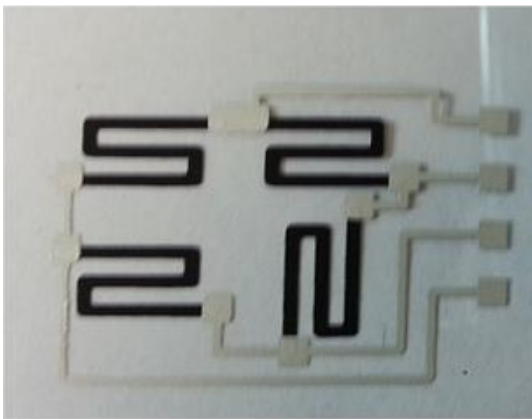
Figure 13. Diagram of the I-V setup for characterizing transistors. Electrical potentials are applied from the drain to the source and from the gate to the source, and the electrical current is measured between the drain and source.



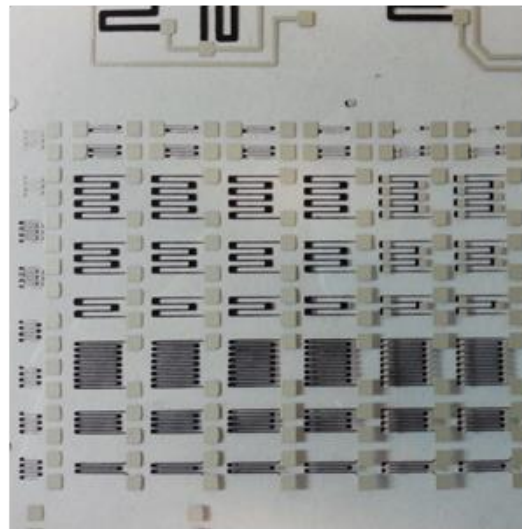
45° rosettes with line widths of 125 μm .



Gages with line widths of 1,100 μm .



Wheatstone bridge with line widths of 1,100 μm .



Various gage designs with line widths of 125 μm to 250 μm .

Figure 14. Screen printed strain gauges with line widths ranging from 125 μm to 1,100 μm .

consistency and with the least variability for the largest linewidths, $\sim 1,100\ \mu\text{m}$. Despite this low variability, gauges with line widths of $\sim 340\ \mu\text{m}$ were selected for strain and fatigue analysis. This selection was made as gauges with smaller line widths occupy less space in an array, increasing the spatial resolution and decreasing the size of the array. In general, gauge resistance scaled linearly with gauge dimensions for a given ink as expected, but sensitivity of gauges (gauge factor) varied only slightly with dimensions. This is because gauge factors are measured based on the relative fractional change of resistance and not absolute resistance.

Screen-printed gauges exhibited void-free microstructures with no evidence of cracking or damage after strain testing as also shown in **Figure 15**. The void-free microstructure indicates the suitability of these gauges for strain applications. Using the micro-tensile strain apparatus, the change in resistance versus strain for the screen-printed gauges was measured for up to 1.1% strain and is shown in **Figure 16**. The gauges were found to have linear responses to strain, gauge factors of $\sim 8.8 \pm 0.3$ and no hysteresis. In addition to the strain measurements, fatigue measurements were made on screen printed gauges where the gauges were subjected to over 10^5 cycles at 0.2% strain and the results are shown in **Figure 17**. Strain response of these screen-printed gauges remained linear for this testing with no change in gauge factor.

Given that the carbon 7082 ink used in screen printing yielded promising gauge results for the prototype system, the temperature dependence of the ink's resistance was also measured. These measurements were done using a free-standing, thick block of carbon 7082 that has been peeled away from the substrate. The result of these temperature measurements is shown below in **Figure 18**. The thermal coefficient of resistance was calculated using the approximately linear portion of the curve from 25 to 60°C and was found to be $2.4 \times 10^{-3}\ \text{K}^{-1}$, which is consistent with the general finding that carbon resistance type inks have relatively high temperature dependence when compared to foil gauges which have a temperature coefficient of resistance of $\sim 10^{-5}\ \text{K}^{-1}$. [53] This is well understood in terms of the conduction mechanism involved in these carbon-based inks. Given the relatively high temperature dependence of the resistance of these inks, temperature compensation was integrated into the design of the prototype strain sensor array system as a precautionary measure even though temperature dependence of actual gauge factor is expected to be less.

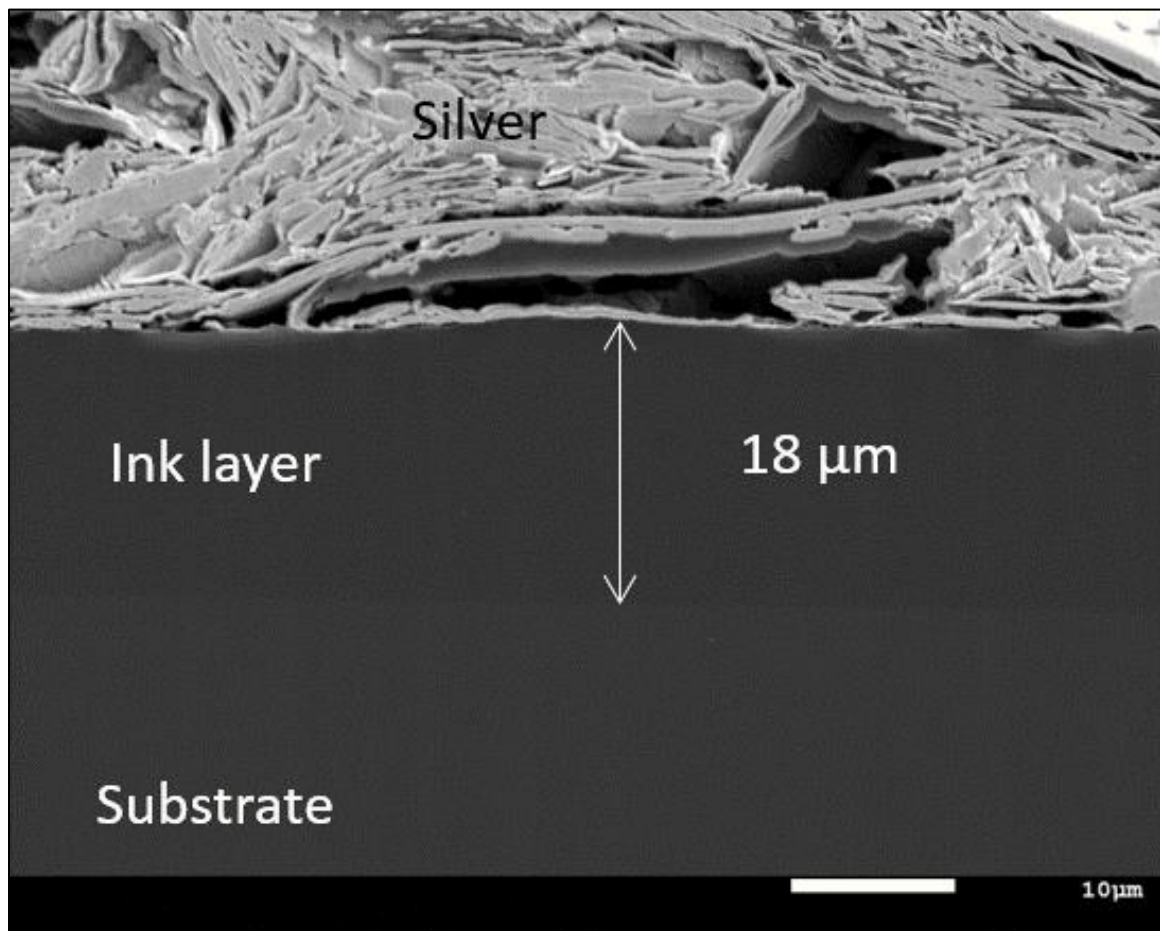


Figure 15. Microstructure of a screen-printed carbon gauge composed of DuPont 7082 carbon ink with an over-layer of DuPont 5028 silver ink

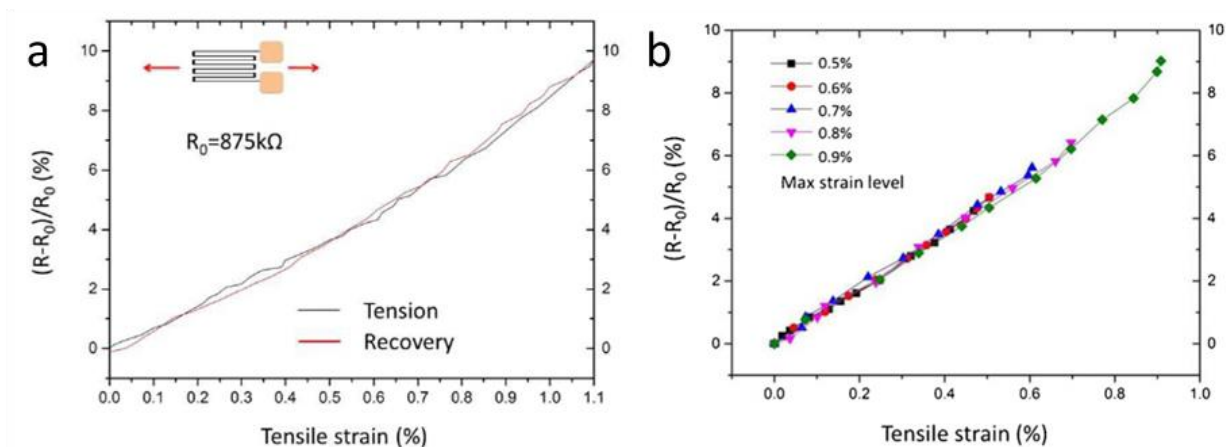


Figure 16: Strain response of a screen-printed strain gauge showing (a) the same linear response with tension and recovery at 1.1% strain and (b) the same linear response when cycling at different levels of strain up to 0.9% strain.

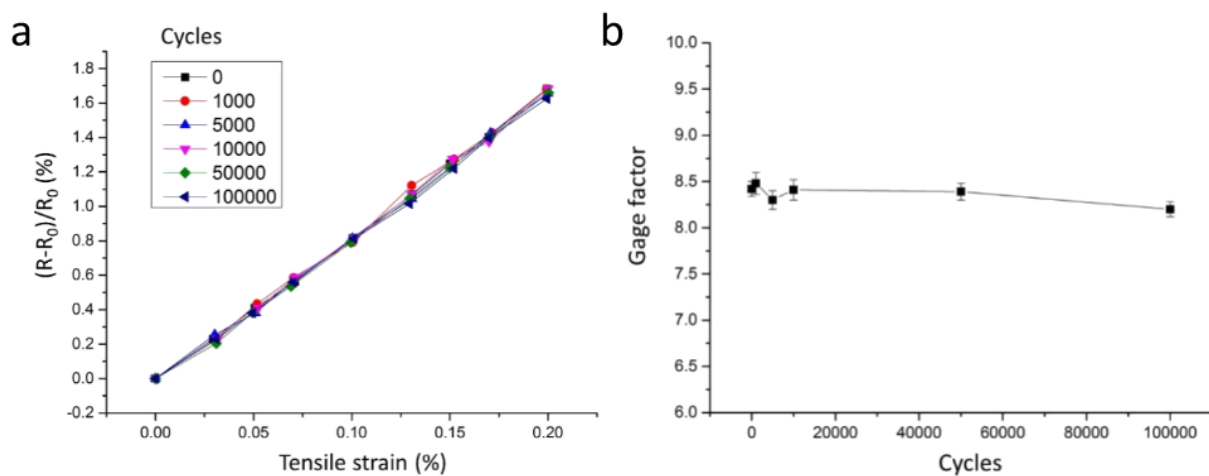


Figure 17. (a) Change in resistance with strain divided by the unstrained resistance vs. tensile strain and (b) gauge factor versus loading cycles, showing the same linear response and gauge sensitivity after 10^5 cycles of 0.2% strain.

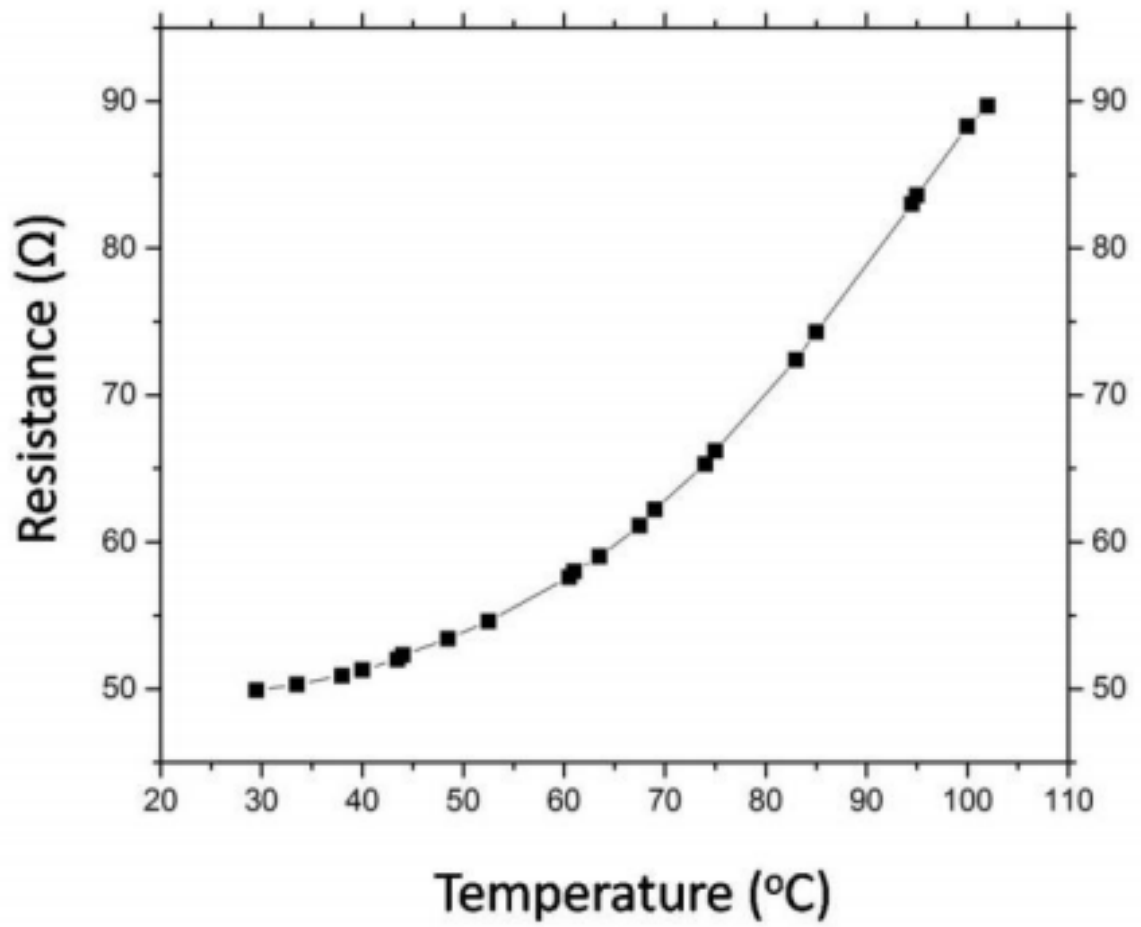


Figure 18. Temperature response of the DuPont 7082 carbon ink used for the gauge element.

3.3.2 Screen Printed Strain Gauge Arrays

The resistance variation of screen-printed strain sensors over the printed area is primarily affected by the mechanics of the screen-printing process. The effect of these mechanics and different printing parameters on ink thickness and resistance is well documented in other work [54]. In this work, the squeegee speed and the applied force were held relatively constant, while the offset of different areas of the screen was adjusted by adding shims under the substrate platform. The offset distance was increased in areas of high resistance and decreased in areas of low resistance to reduce the overall variation. The effect of these small adjustments at reducing variation can be seen in several ways. **Figure 19(a)** and **Figure 19(b)** show color-maps of the resistances from one of our first printed strain gauge arrays and a strain gauge array that was printed after several iterations of adjusting the offset distances. In these images, the color is scaled from the minimum deviation in resistance from the mean, to the maximum deviation in resistance from the mean for each strain gauge array. Color-maps like these were used for locating outliers and determining where the offset distance needed to be adjusted. After the offset was adjusted, most of the outliers were removed and the remaining resistances were closer to the average. Additionally, the average resistance, standard deviation, and deviation of the minimum and maximum from the mean is shown in **Table V**, showing a 10% reduction in the standard deviation, and a 15-25% reduction in the deviation of the minimum and maximum from the mean. Although the resistance variations do not greatly affect the gauge factors as seen in our previous work [10], less variation simplifies the design of the data acquisition system (DAQ) and allows for more sensitive measurements.

Due to the high variability in resistance of the printed strain elements, it was impractical to use a traditional Wheatstone bridge configuration for measuring strain. Instead, the DAQ drives a specified current through each strain sensor and then measures the resulting voltages. The resistance can then be calculated and compared with the initial resistance value to determine the change due to strain. The benefit of this approach is that it relaxes manufacturing tolerance requirements, allowing a wide range of resistances to be used. The main limitation is the sacrificed sensitivity of the resistance measurements. Since the voltage across the entire strain element is being measured, and changes in resistance due to strain are small, much of the analog/digital converter's resolution is not being efficiently utilized. This is in contrast to a Wheatstone bridge approach, where the bridge output more directly reflects the change in resistance and the ADC's input range can be fully utilized. The ideal situation for the printed

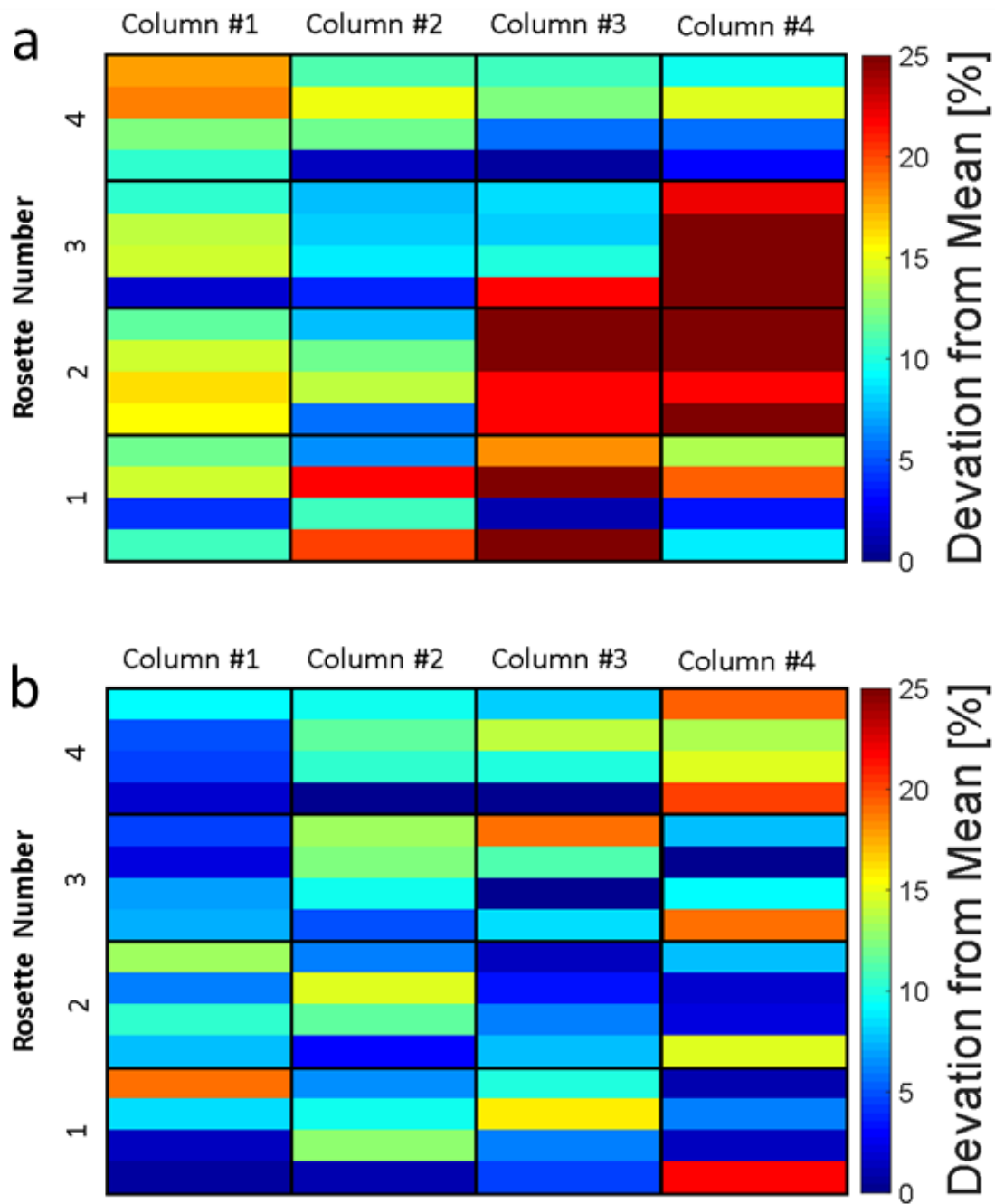


Figure 19. Color maps of the deviation of the resistance values of each strain gauge from the mean resistance for the sheet of 64 strain gauges. (a) Resistance values prior to optimizing the printing procedure. (b) Resistance values after optimizing the printing procedure, where the procedure was optimized by adjusting the distance between the screen pattern and the substrate.

	Average Resistance [kΩ]	Standard Deviation [%]	Deviation of Minimum from the Mean [%]	Deviation of the Maximum from the Mean [%]
a	8.11	20.5	37.7	56.7
b	13.61	10.1	18.9	21.9

TABLE V. AVERAGE RESISTANCE, STANDARD DEVIATION, AND DEVIATION OF THE MAXIMUM AND MINIMUM RESISTANCE FROM THE MEAN FOR (A) ONE OF OUR EARLIEST PRINTED STRAIN GAUGE ARRAYS, AND (B) A STRAIN GAUGE ARRAY THAT WAS PRINTED AFTER REDUCING THE VARIATION IN OFFSET DISTANCE BETWEEN DIFFERENT AREAS OF THE SCREEN.

strain sensor would be for the sensor material to be very sensitive to strain and insensitive to all other factors. Unfortunately, this is very difficult to achieve with commercial inks. To investigate the effects of temperature on the resistance of the carbon ink used for the strain sensors, the temperature coefficient of resistance, α , was measured using a cured carbon ink block (36Ω at 300K) that was not attached to a substrate. Temperature was continuously recorded using a thermocouple and ink resistance was measured using a B&K 5491B Precision Multimeter. **Figure 20a** shows the resistance of the carbon block (36 Ω at 300 K) as a function of temperature.

The temperature response of the curve was fitted used **Equation 1**,

$$R(\Omega) = a_0 + a_1 \cdot T(^{\circ}\text{C}) + a_2 \cdot T(^{\circ}\text{C})^2 \quad (1)$$

$$\text{where } a_0=35.9, a_1=1.5 \times 10^{-3}, \text{ and } a_2=1.6 \times 10^{-4}.$$

At room temperature, the temperature coefficient of resistance, α , of the carbon ink is $0.26 \times 10^{-3} \text{ K}^{-1}$. For comparison, the temperature response of DuPont 7082 was also measured and is shown in **Figure 20b**. Using the same fitting, the coefficient of resistance for DuPont 7082 inks was found to be $2.4 \times 10^{-3} \text{ K}^{-1}$. The larger temperature coefficient of resistance for DuPont 7082 was suspected to be due the different carbon particles in this ink. DuPont 7082 uses carbon black particles while DuPont 7102 uses graphite particles which are larger and more conductive. The linear coefficient of thermal expansion is usually on the order of $10^{-6} \sim 10^{-5} \text{ K}^{-1}$ [55]. Therefore, the temperature coefficient of resistance divided by the gauge sensitivity is the dominant factor in the temperature sensitivity of the carbon-ink sensors.[56,57] The temperature sensitivity of the carbon ink is a material-related property and therefore must be compensated in calculations of strain. Instead of looking for new ink materials, separating the thermal

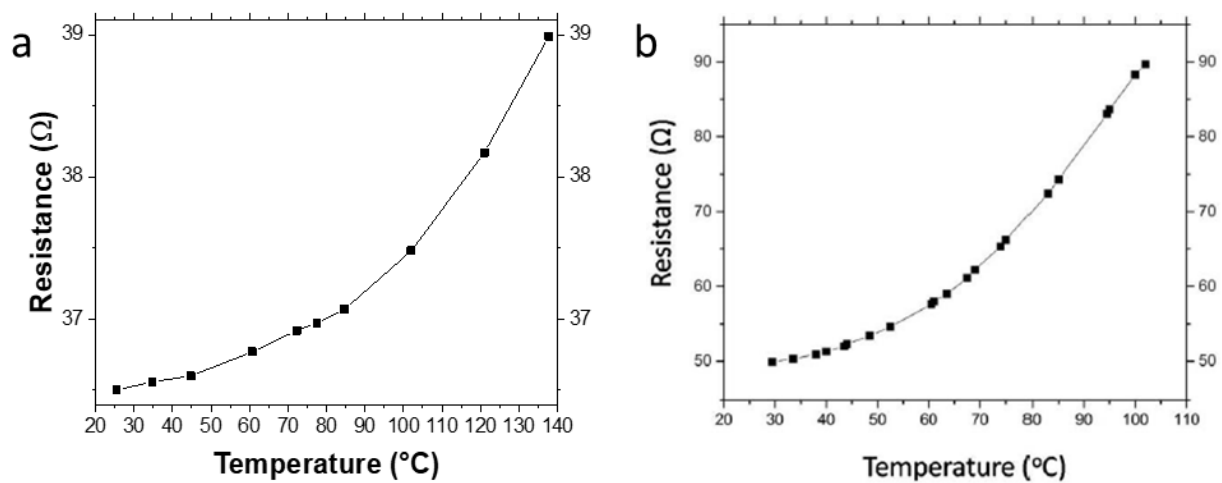


Figure 20. Resistance change of free-standing carbon ink blocks as a function of temperature. (a) DuPont 7102. (b) DuPont 7082.

signal from the strain response is a more practical and realistic approach. This can be achieved with a proximity temperature sensor as long as the temperature response of the printed sensors is well established or a dummy strain sensor which is unstrained but still exposed to varying temperatures can be used to offset the change in resistance due to temperature. A dummy sensor was included in the 4x4 strain sensor array as one method of mitigating the printed strain sensor temperature sensitivity as shown in **Figure 21**. The dummy sensor approach was utilized to prevent the need for additional temperature sensing devices and associated circuitry on the array. The primary drawback to this approach is the increase in size of the array to accommodate the additional sensor and trace routing for the extra sensor, as well as the strain relieving area around the sensor to ensure that it remains unstrained. This was accomplished by cutting the polyimide substrate around the dummy gauge. This approach was acceptable for a relatively small array but may be impractical for larger more complex arrays.

As the prior strain gauges were primarily printed on PET film, we investigated the surface of our Kapton HN polyimide films and the interface between our inks and the polyimide film. As seen in **Figure 22**, optical profilometry of the polyimide surface showed relatively smooth films with an average roughness of 50 nm, but with 1-300 μm particles embedded in the film which extend as high as 1.5 μm above the surface. As these particles were only found to extend 1.5 μm above the film surface and are relatively small in diameter, they are unlikely to significantly affect the printed films which are at minimum five microns thick. Our previous work on printed strain gauges has shown that a dense, void-free microstructure and interface between printed inks and the substrate is essential for components that are subjected to strain, and is especially important for reliable measurements from strain sensors. **Figure 23(a)** and **Figure 23(b)** show cross-sectional images of the carbon and silver ink that were used for the strain gauge arrays on polyimide. The lack of voids and cracks in the microstructure and between the ink and the substrate suggests that these inks would be good candidates for strain sensor components.

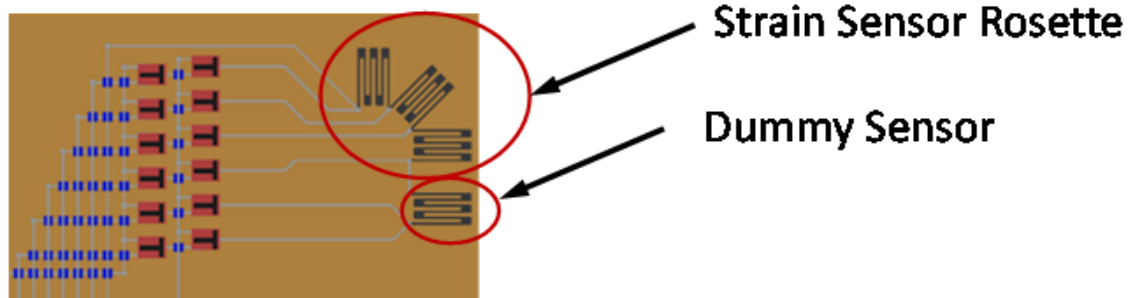


Figure 21. Configuration of the strain gauge array with dummy gauge for temperature compensation.

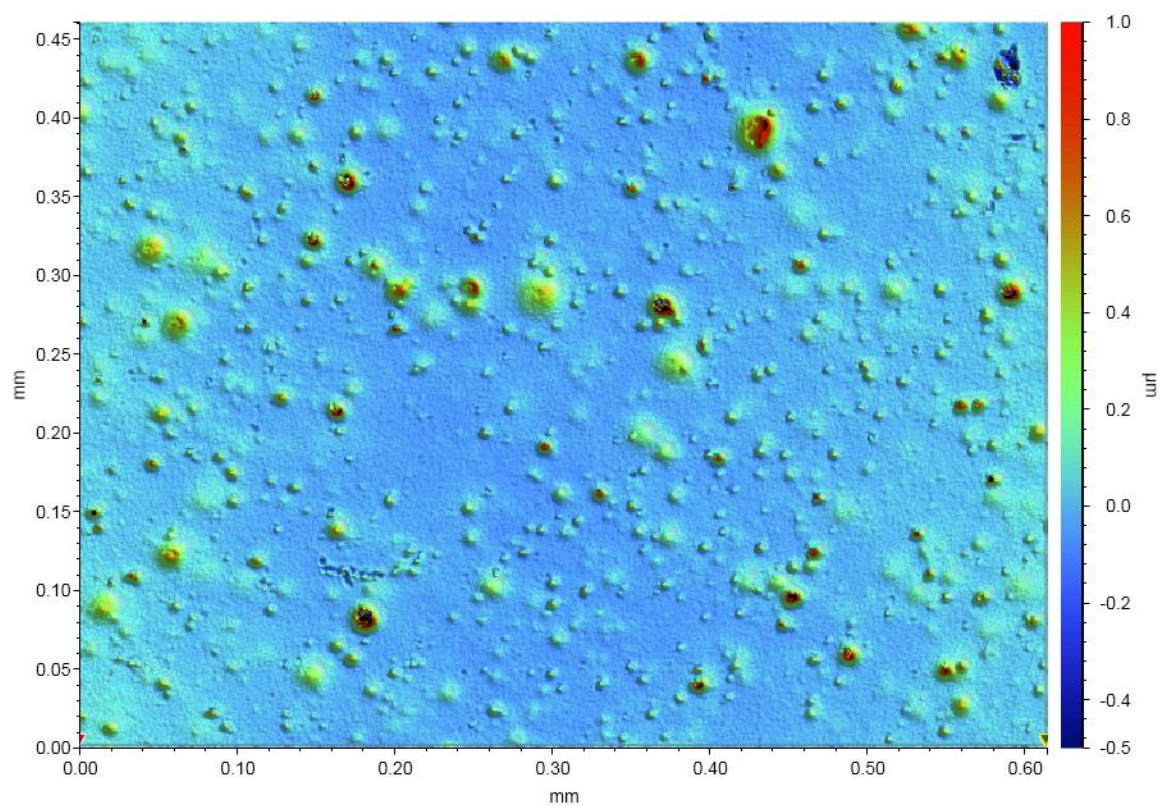


Figure 22. Optical profilometry image of Kapton HN polyimide film.

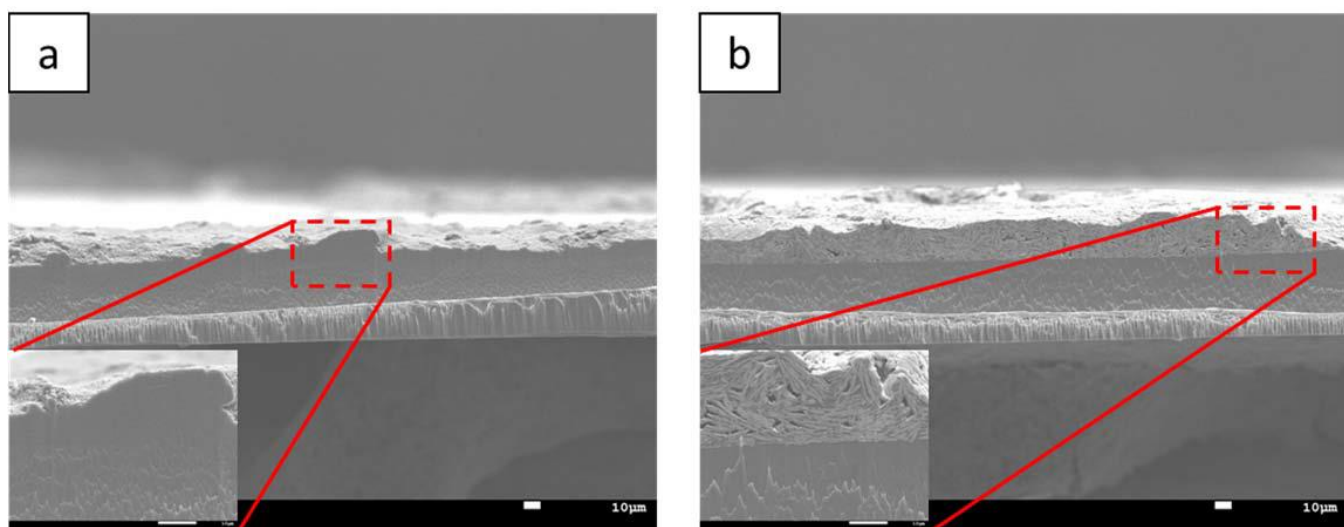


Figure 23. Cross-sectional images of (a) carbon and (b) silver inks used for fabricating strain gauge arrays, showing void-free interfaces when screen-printed onto a polyimide substrate.

After characterizing and optimizing the printing process for the 4x4 array, the strain response of some of the gauges were evaluated. These initial strain measurements were done by inducing strain longitudinally with different radii of curvature and were done for the three gauges of one rosette and the dummy gauge. An image of the four gages that were tested is shown in **Figure 24**, where the fourth gauge from the left is a dummy gauge used for temperature compensation. The strain response of this rosette is shown in **Figure 25** and the average gauge factor of this rosette was found to be 18.8 with a standard deviation of 0.7.

The fully printed components of the 4x4 strain sensor array along with the array with multiplexing transistors and header for connecting the data acquisition unit bonded are shown in **Figure 26**. In this figure, the array with printed and discrete components bonded has its sensing elements bonded to an aluminum plate, and the dummy gages partially cut out from the polyimide substrate. This strain sensor array was bonded to a 12 x 12 x 0.032 inch 6061 aluminum sheet to allow for characterization of the response from the various elements in the array. This test specimen was tested in a uniaxial test machine with grips placed in the center of the sheet. This loading did not result in a uniform applied strain over the sample, but allowed for evaluation of the durability of the printed strain sensors and transistors. Images of the test setup and sample are shown in **Figure 27**. The sample shown in **Figure 27** was loaded to achieve strains of $2000\mu\epsilon$ on the row 1, column 1 sensor. This load was cycled three times and the response from the row 1, column 1 strain sensor can be seen in **Figure 28a**. As can be seen in the figure, response of the sensor in terms of change of resistance of the gauge is roughly linear with larger variations in response as the strain increases. This variation in the response of the strain sensor is believed to be due to random noise which is present primarily due to the differential measurement approach. After the third load cycle, a number of the discrete transistors debonded from the array which resulted in loss of the ability to acquire data from these strain sensors. The location of array elements which lost one or more transistors is shown in **Figure 28b**. The exact cause of the transistor debonding is not certain, but the most likely cause is debonding of the silver epoxy which was used to attach the leads of the discrete transistor to the printed silver ink traces in the array. This debonding would be due to the shear stress that developed due to local variation in stiffness of the transistor casing, silver epoxy and the polyimide substrate. These stresses could be reduced by using flexible transistors which are printed or made through some other process, or grading the material properties at the interface of the discrete component using encapsulates or other techniques.

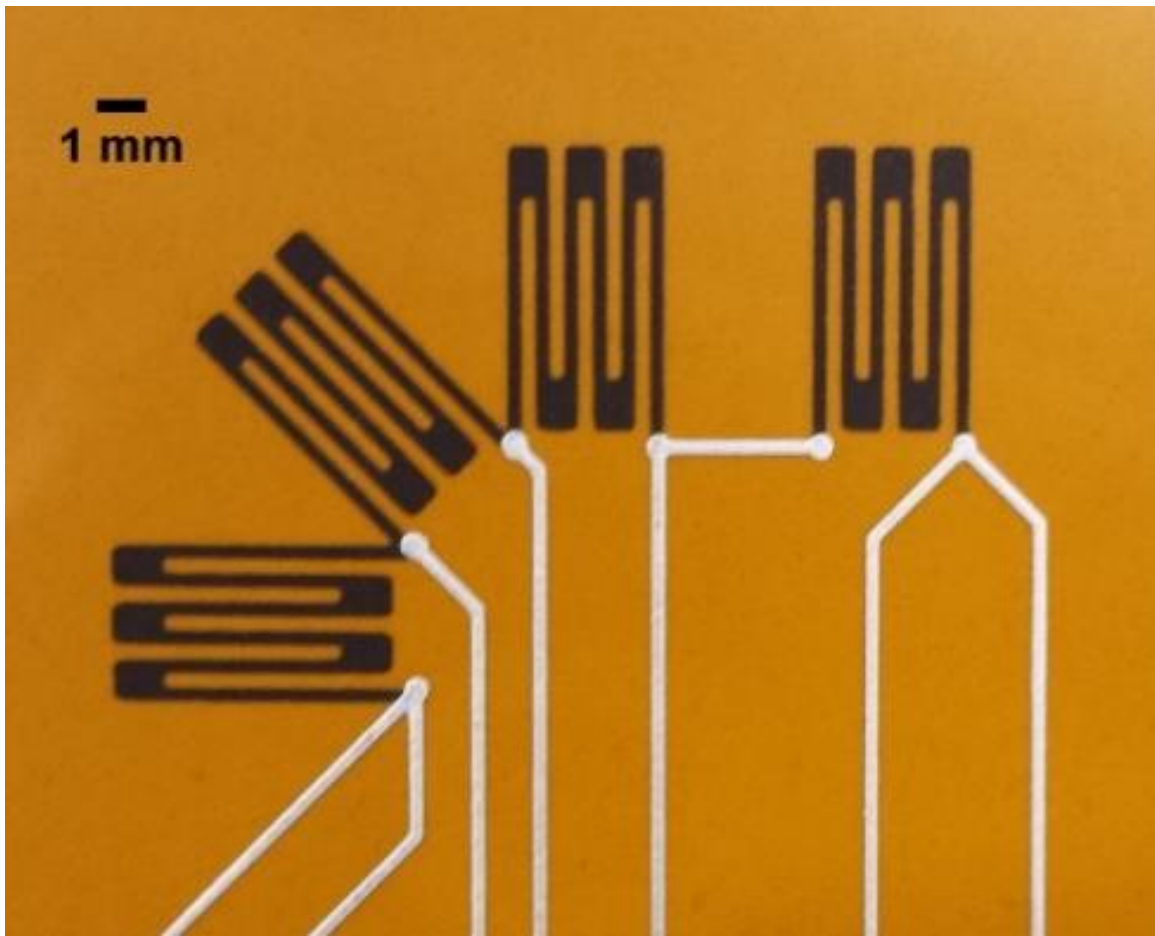


Figure 24. Image of a screen printed 45° rosette with temperature compensation gauge and silver traces, where gauge line widths are 305 μm , gauge lengths are 7.7 mm and silver trace line widths are 305 μm .

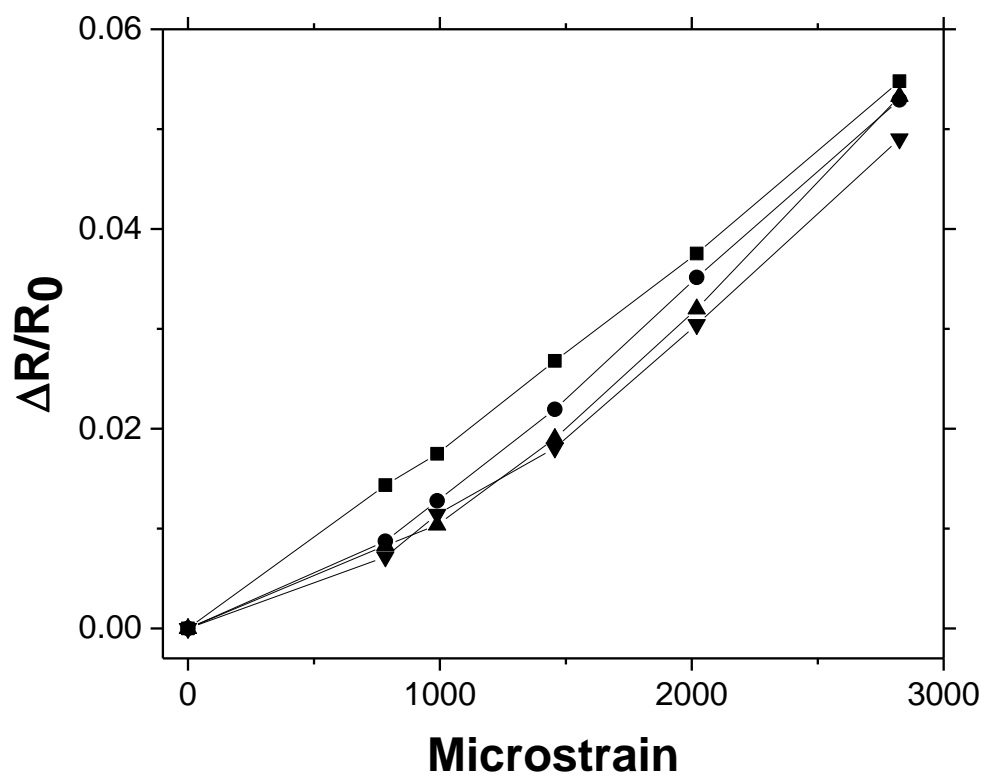


Figure 25. Normalized change in resistance versus microstrain showing the linear response of four separate gauges and a gauge factor of approximately 18 ± 0.7 .

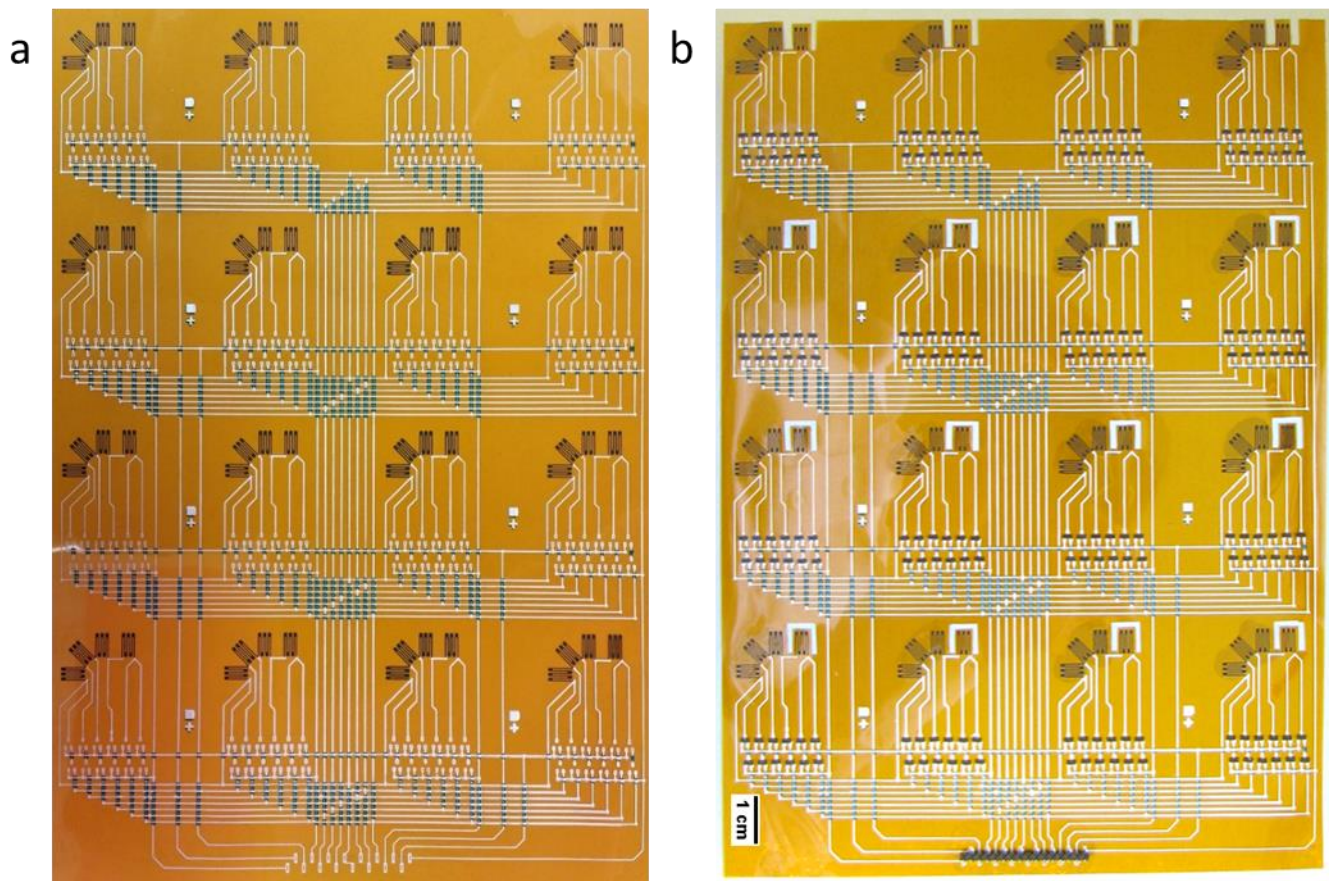


Figure 26. (a) Fully printed 4x4 strain gauge array and (b) a fully printed 4x4 strain gauge array bonded to an aluminum plate with discrete bare-die transistors and data acquisition connector bonded to the substrate.

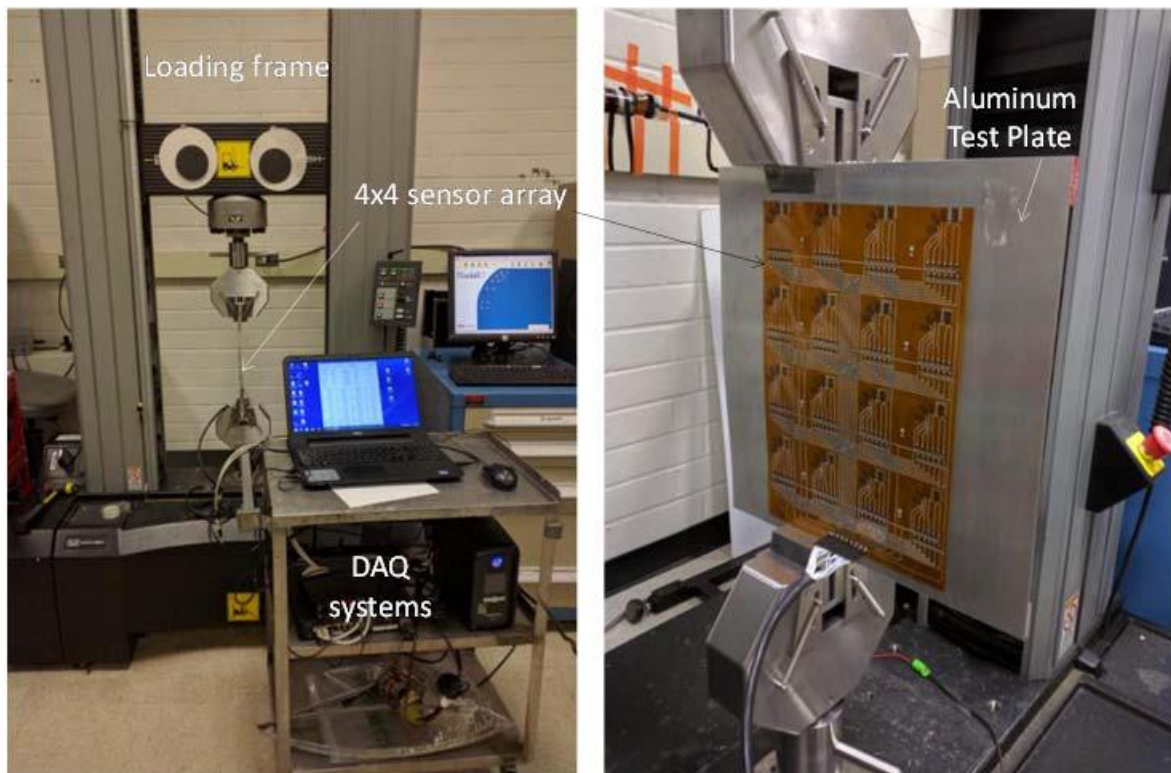


Figure 27. Uniaxial tension test of printed strain sensor array on aluminum test sheet showing the test setup and the printed strain sensor array.

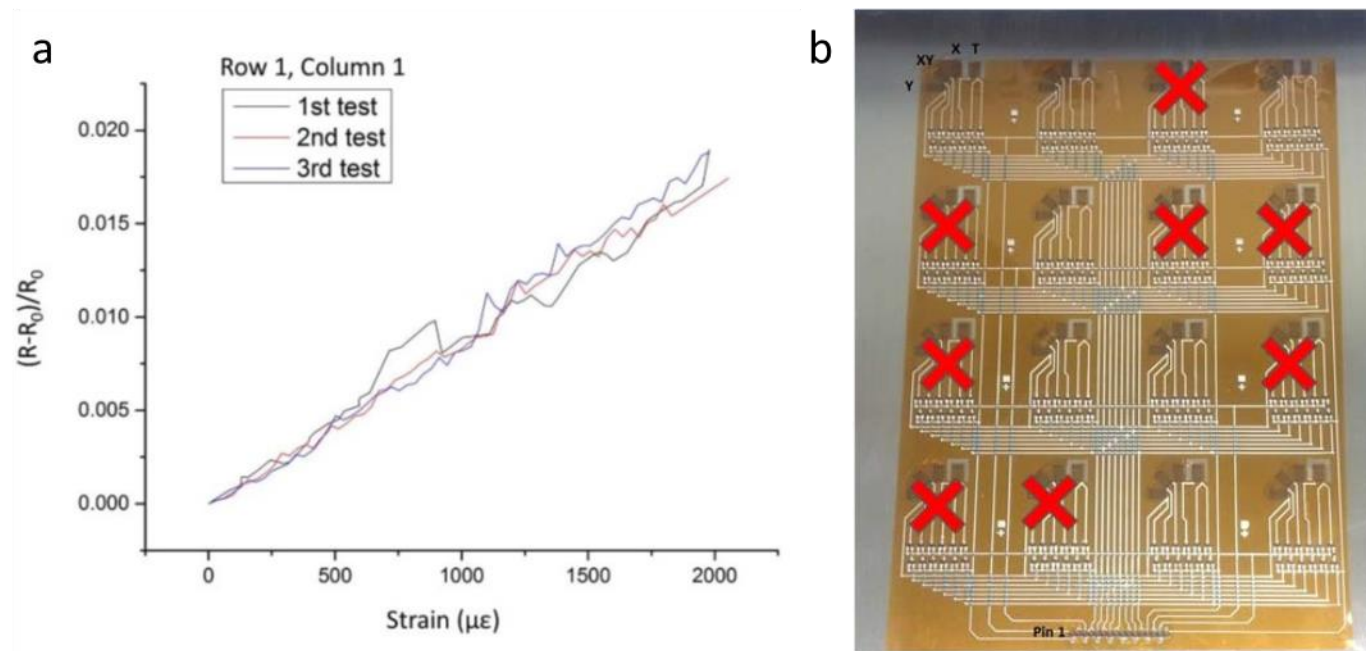


Figure 28. (a) Response from the row 1, column 1 strain sensor during 3 different runs of the uniaxial tension test, and (b) strain gauge rosettes that suffered debonding of at least one transistor during the test cycles.

3.3.3 Screen Printed Transistors

Field effect transistors typically require three different materials, a conductor, a dielectric, and a semiconductor. For the transistors printed here two different silver inks were used for the conductor, barium titanate ink was used for the dielectric and semiconducting single-walled CNTs for the semiconductor. An image of top-gate transistors printed on PET is shown in **Figure 29**. The first printing optimization investigated was the dilution of silver ink used for the source and drain electrodes and the barium titanate ink used as the gate dielectric. Cross-sections of our initial transistors without any ink dilution showed dielectric layers thicker than 10 μm with source and drain layers approximately 8 μm thick, which lead to frequent short circuits and poor transistor performance. These short circuits and poor performance were due to the proximity of the gate to the source and drain, relative to the semiconductor. Optimal dilution of the source and drain and dielectric was then found by comparing the effect of dilution on print thickness, printing resolution, short-circuiting, and transistor performance. For our printing setup, the optimal dilution was found to be 15 wt.% for the source and drain and 10 wt.% for the dielectric with two layers of dielectric printed. These dilutions resulted in source and drain thicknesses of approximately 3 μm and dielectric thicknesses of approximately 7 μm . Any further dilution of the silver ink for source and drain electrodes led to loss of printing resolution with silver ink spreading over into the channel region. Further dilution of the gate dielectric ink led to shorting through the dielectric layer between gate and source and/or gate and drain.

Even with optimized ink dilutions, a significant fraction of transistors printed in a batch (55 in all) had short circuits between the source and gate or source and drain. Cross-sectional SEM images of these transistors have shown a likely cause of shorting to be silver flake-like particles in the silver ink protruding into the dielectric layer, as can be seen in **Figure 30a**. In an effort to prevent these particles from causing short circuits in future prints, a mechanical flattening method was adapted where a 2-kg metal cylinder is rolled across the partially dried source and drain layer of each transistor print, and an example of a SEM cross-sectional view of a transistor using this flattening approach is seen in **Figure 30b**. The flattening method that seemed most effective was after a 10 minute partial cure of source-drain silver ink. This flattening procedure was further analyzed with optical profilometry. Here the optical surface topology shows little change in the average thickness of the ink layer but a significant reduction in the maximum peak heights of the printed layer showing that the flattening procedure influences only the thickest regions of the printed film. Histograms of frequency versus height from the optical profilometry data

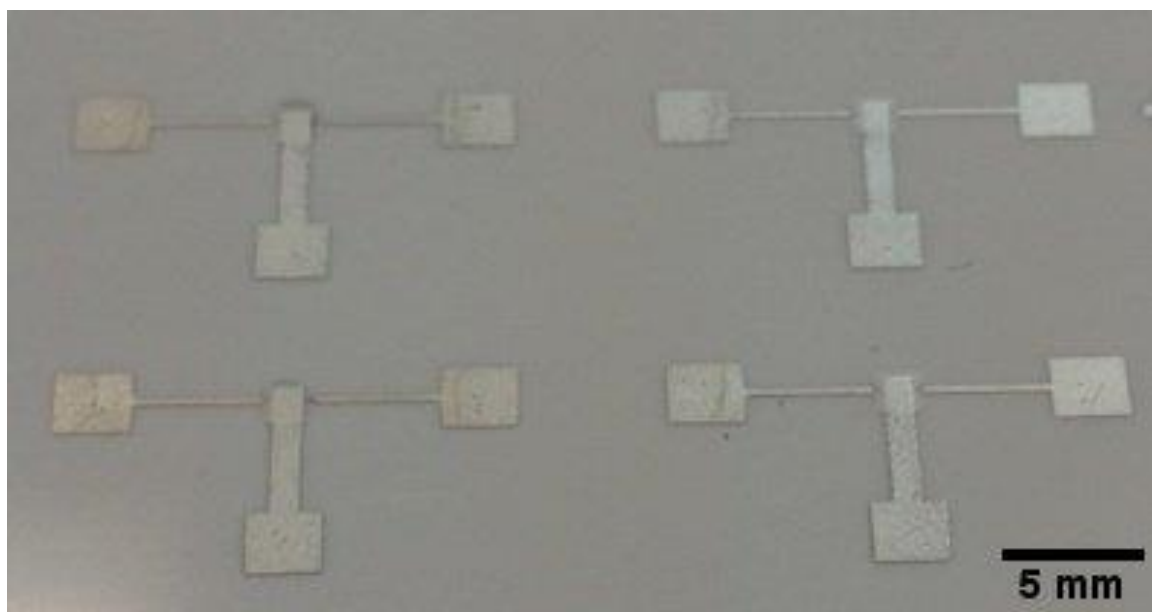


Figure 29. Optical image of top-gate screen-printed transistors on a PET substrate.

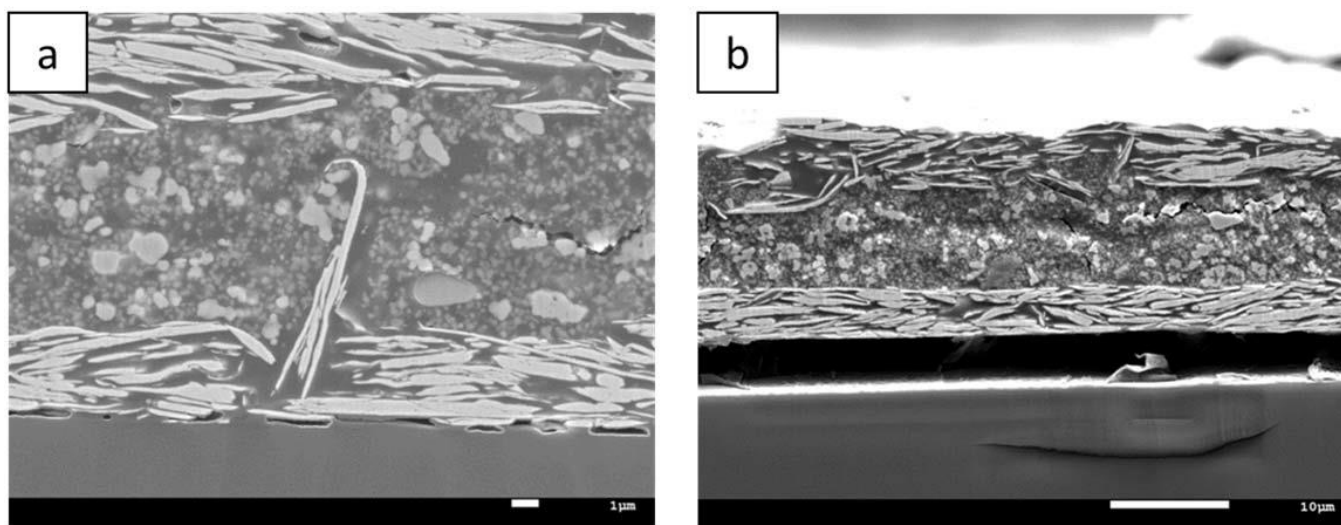


Figure 30. Cross-sectional image of the source and drain of a transistor (a) without a flattened source and drain layer and (b) with a flattened source and drain layer and debonding between the source and drain layer and the substrate.

for as-printed and mechanically flattened silver lines are shown in **Figure 31**. Although the flattening method reduced the number of short circuits in a batch of printed transistors, it did not significantly improve the transistor performance in terms of on-off ratio or on-current.

In addition to flattening of silver ink, thinner layers of dielectric were attempted in order to further improve the transistor performance. While these thinner layers did increase the current on/off ratios for a few devices, they also increased the frequency of short circuits and in fact no functional transistors were possible with gate dielectric thicknesses of less than 5 μm due to excess shorting. The limit on dielectric thickness comes from thickness of the source and drain layer. Upon closer examination by SEM as shown in **Figure 32** below, the gate dielectric is printed with a relatively constant height over source/drain and channel regions of the transistor; however, there is significantly different dielectric thicknesses over each of these regions. More specifically, the dielectric is thinner above the source and drain regions, which leads to higher instances of shorting. In contrast, over the channel region, the dielectric is thicker which degrades on-off switching with gate voltage. For precisely this reason, it is important to have print thicknesses of source and drain electrodes to be as thin as possible.

After optimizing the printing of the source/drain electrodes, gate dielectric, and gate electrode, the next area of printing fabrication to improve was the S-SWCNT deposition. One printing aspect that strongly increased conductivity of transistors by few orders of magnitude was using Al_2O_3 coated PET film in place of uncoated PET film. **Figure 33** shows this strong substrate influence for two comparable transistors printed on these two substrates. In this case, the transistors prepared on the Al_2O_3 coated film had roughly 100,000 fold higher on-current than the transistors printed on uncoated PET. Additionally, the S-SWCNT solution drop-casted onto the alumina surface had a much lower contact angle in the deposition process and were observed to spread out much more evenly, indicating noticeably higher affinity of the solution for the rough, porous Al_2O_3 coated PET than the uncoated PET. There was also a higher off-current for the transistors printed on Al_2O_3 coated PET, which is believed to be due to a small amount of S-SWCNTs deposited outside of the channel region where it is less affected by the gate bias. Optical profilometry images of these two substrates is shown in **Figure 34**. Here the uncoated PET was found to have an average surface roughness of approximately 40 nm while the alumina coating had an average surface roughness of about 2,300 nm. The rougher surface of the Al_2O_3 coated PET is certainly one factor influencing the higher affinity for S-SWCNTs.

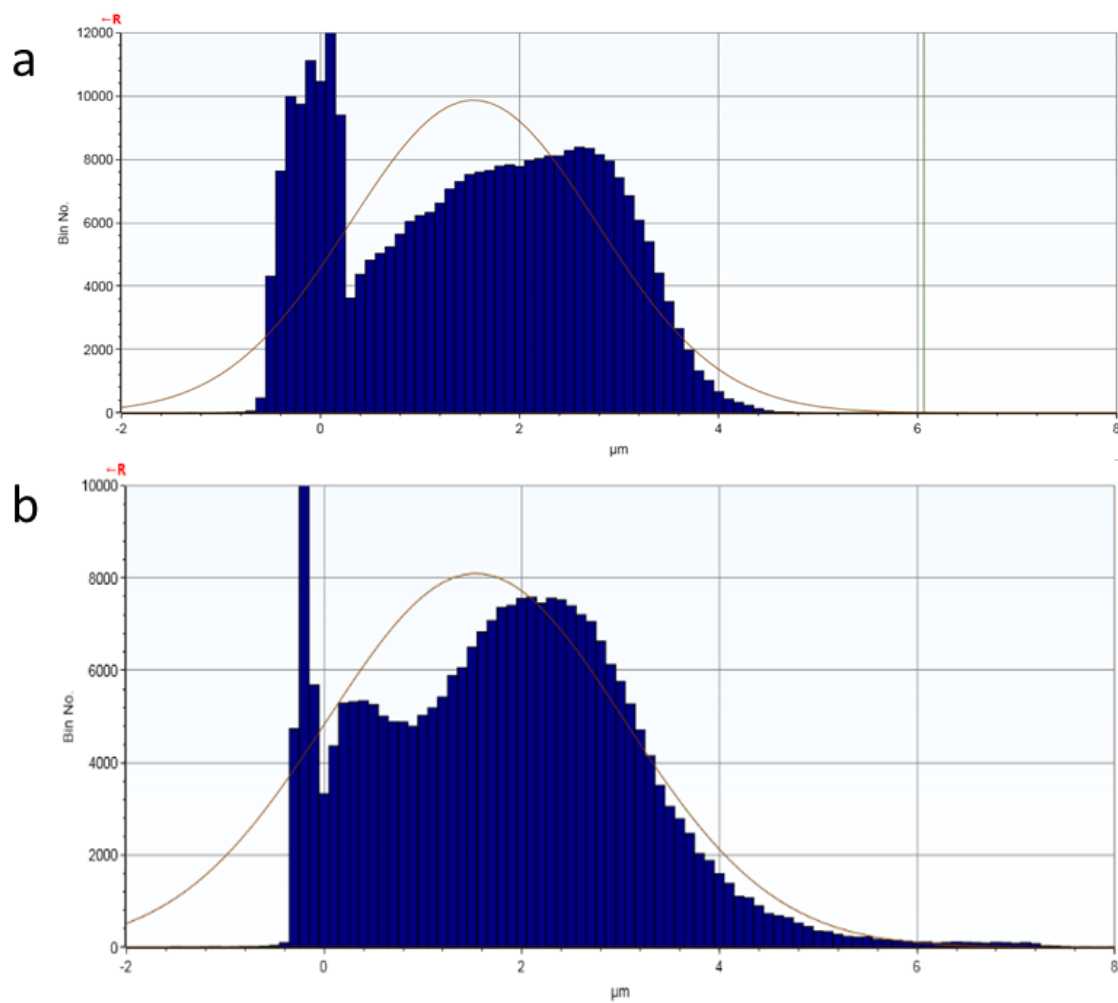


Figure 31. Histograms of frequency versus thickness from optical profilometry of (a) as-printed and (b) mechanically flattened silver ink.

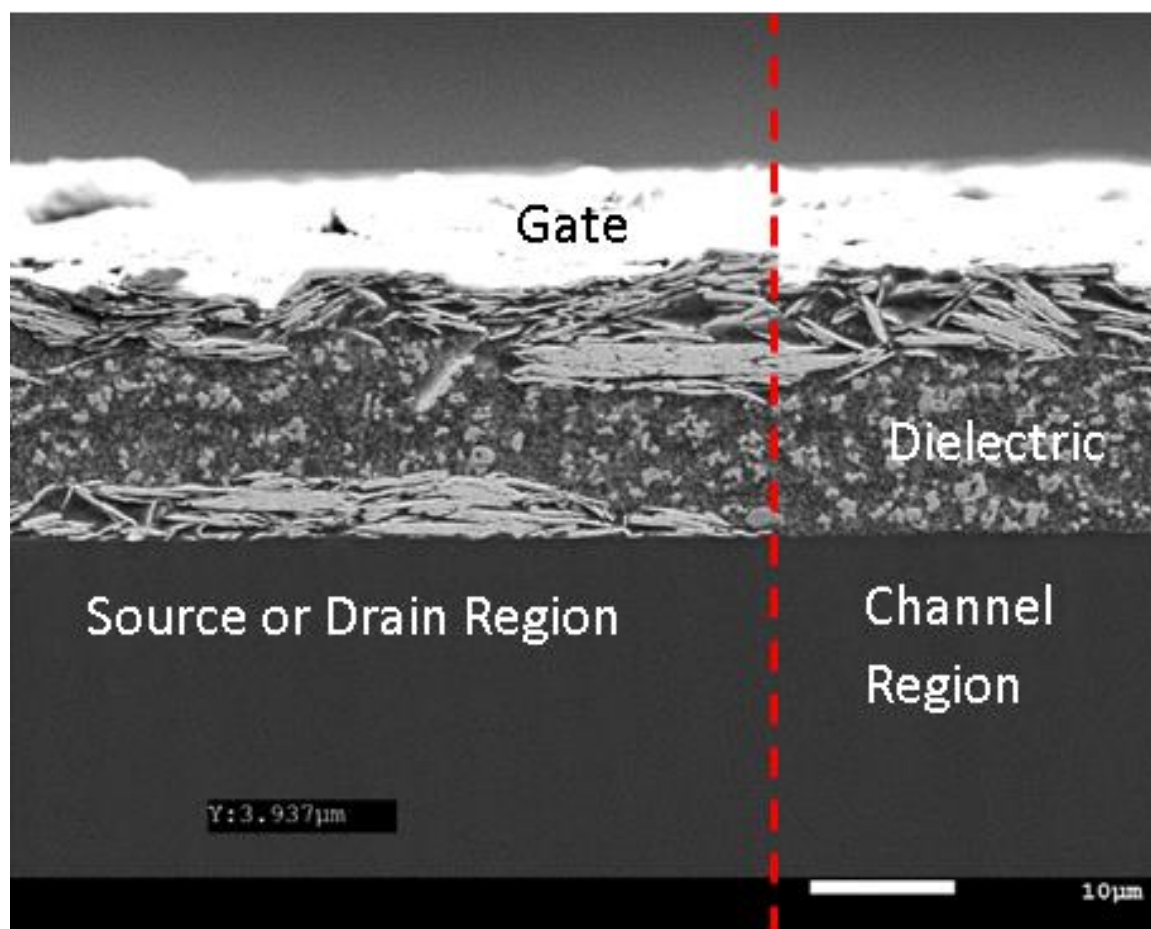


Figure 32. SEM cross-sectional image of a transistors showing variation of the dielectric thickness between the channel region and the source/drain region.

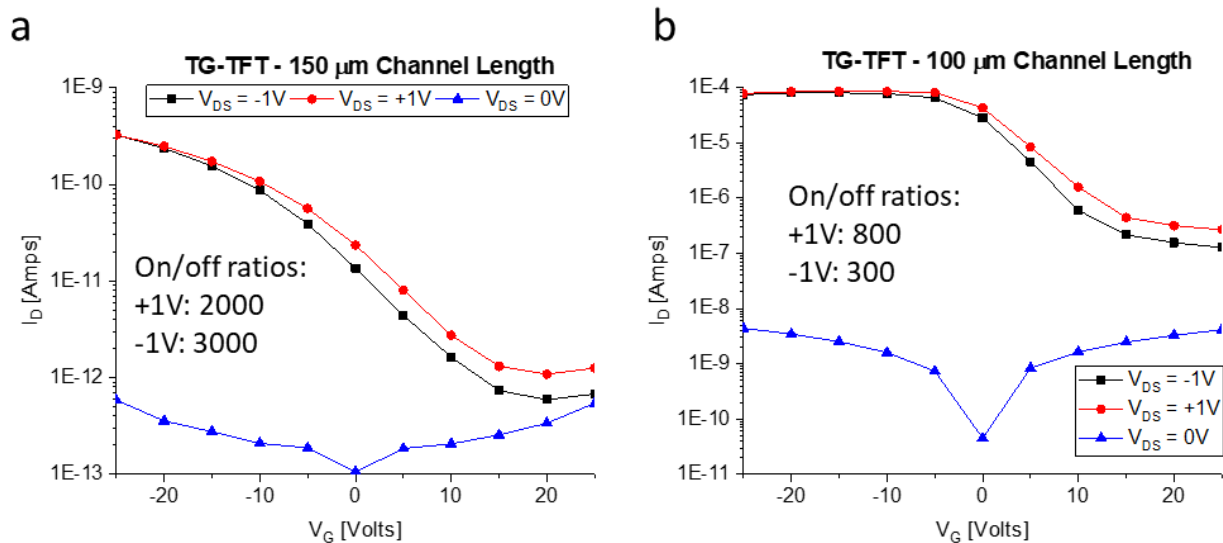


Figure 33. I-V responses of screen-printed transistors on (a) an uncoated PET substrate and (b) an alumina coated PET substrate.

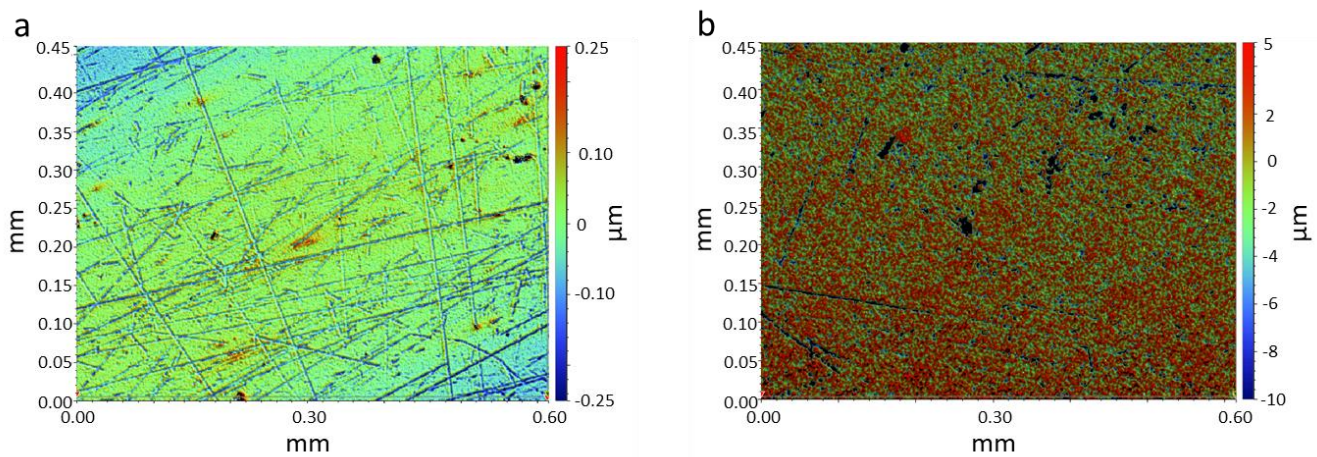


Figure 34. Optical profilometry images of (a) an uncoated PET substrate and (b) an alumina coated PET substrate showing the much more textured surface of alumina coated PET.

The higher mobility observed with transistors prepared on the Al_2O_3 coated PET are certainly promising and are therefore worthy of further investigation. Since the Al_2O_3 coated PET is coated on one side only and there is a mismatch in thermal expansion coefficients of the alumina coating and the PET film, the Al_2O_3 coated PET substrates tend to curl up when undergoing thermal curing of the transistor inks, and the alumina coating de-bonded from the PET film. To prevent this curling, the substrates were taped to a metal plate during heating. These substrates did not curl, and alumina coating did not debond from the PET film. Additionally, these transistors were tested under longitudinal and transverse strain and above 2% strain, the alumina coating cracked and debonded from the PET surface, damaging some of the transistors. SEM cross-sections of the alumina coating before being strained and after transistor printing and being strained are shown in below **Figure 35**.

Due to the limitation of the alumina coating, transistors prepared on uncoated PET were also characterized after strain and fatigue. A cross-sectional SEM image of a transistor as printed is shown in **Figure 36a** showing a void-free interface between the transistor inks and the substrate. Cross-sectional SEM images of transistors after 10,000 $\mu\epsilon$ and 10^5 cycles at 1000 $\mu\epsilon$ are shown in **Figure 36b** and **Figure 36c**, respectively. In **Figure 36b**, a crack can be seen running through the dielectric and gate of the channel region of the transistor as well as some debonding at the interface in the channel region. The debonding is due to poor adhesion of the S-SWCNT solution and thereby the overlying dielectric to the PET substrate. Cracking likely begins after the dielectric debonds from the PET substrate. Similar damage to the transistor is seen in **Figure 36c**. However, in this case the entire channel region has debonded and the crack through the dielectric and gate is $\sim 1\text{-}3\ \mu\text{m}$.

In addition to different substrates, different conductive inks were used to examine their effect on transistor printing. **Figure 37(a)** shows a cross-section of a transistor that was printed using DuPont 5028 Ag as the conductor and **Figure 37(b)** shows a transistor that was printed using Conductive Compounds Ag-530 as the conductor. **Figure 37(a)** has inks from the two different vendors and some compatibility issues were observed. In this case, polymer-rich particles from the silver ink have separated from the rest of the conductive layer. These polymer-rich particles were only found at the interface of the dielectric and source and drain layer, and are believed to have caused short-circuits across the dielectric layer causing failure of many printed transistors. No polymer particles were found when examining transistors prepared using Ag-530 with this dielectric ink. Incompatibilities between the printed materials were also seen when preparing bottom-gate transistors. **Figure 38(a)** and **(b)** show optical

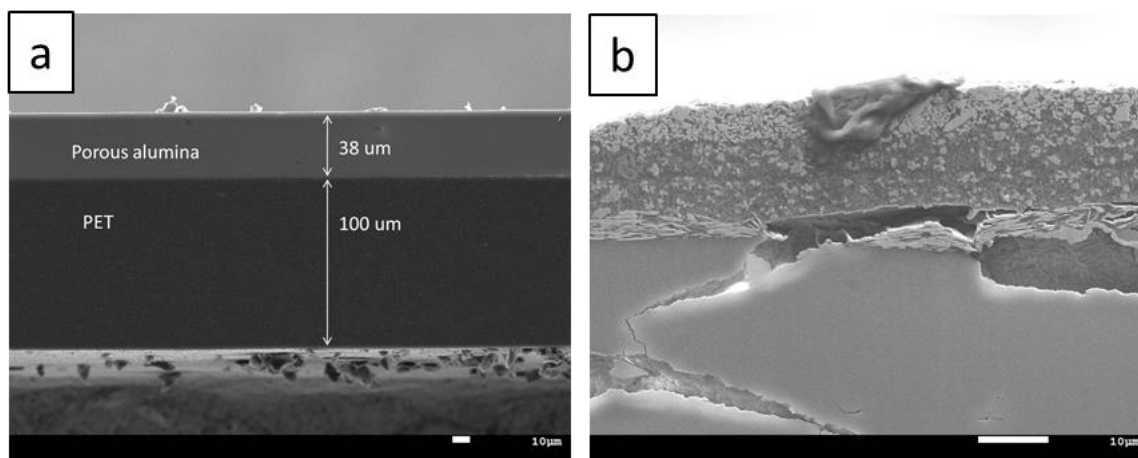


Figure 35. Cross-sectional SEM of (a) unstrained Al_2O_3 coated PET before printing and (b) after transistor printing and 2% strain.

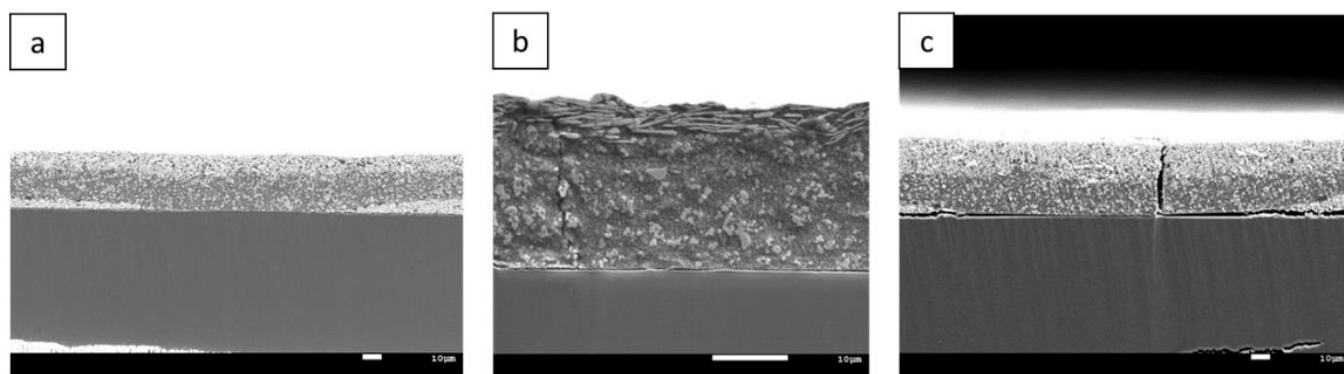


Figure 36. Cross-sectional SEM images of (a) an unstrained transistor, (b) a transistor after one cycle of 10,000 $\mu\epsilon$ strain was applied, and (c) a transistor after 10^5 cycles of 1,000 $\mu\epsilon$ were applied.

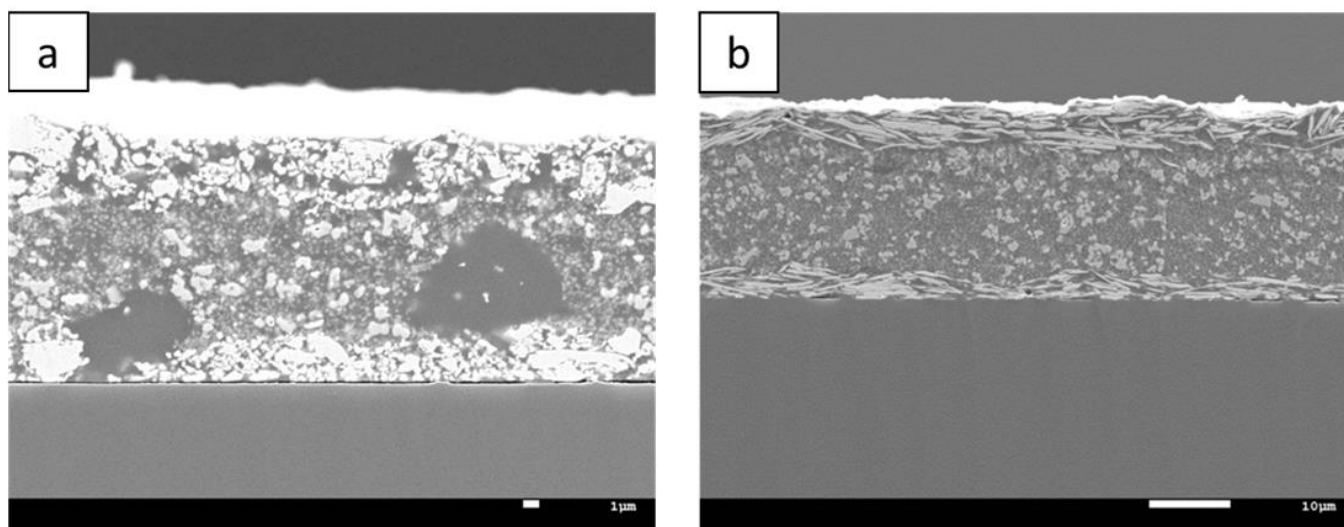


Figure 37. Cross-sectional SEM images of a transistor with (a) incompatible conductive and dielectric inks and (b) more compatible conductive and dielectric inks.

microscopy images of top gate and bottom gate transistors respectively. Since the CNT solution is deposited first for top-gate transistors and quickly evaporates, it doesn't greatly affect the subsequent layers; however, it partially dissolves the source, drain and dielectric layers when deposited last for bottom-gate transistors. This partial dissolution is due to the use of toluene as the suspension media for the CNT solution. Short circuits and large gate-currents occurred when the toluene dissolved through most of dielectric; however, even when the toluene didn't dissolve through the dielectric, the transistors were not functional as the CNTs did not form a connection between the source and drain.

Another approach to increasing transistor mobility was to try different surface treatments of uncoated PET and different S-SWCNT deposition procedures. Similar to prior studies using S-SWCNTs for transistors, oxygen plasma treatment of PET and poly-l-lysine coating procedures were attempted to functionalize the substrate surface for higher S-SWCNT affinity.[42,46,50] Oxygen plasma treatment alone was found to increase the on-current approximately 10-fold, from 1 nA to 10 nA, but did not otherwise appear to affect the performance. Oxygen plasma treatment followed by lysine treatment, increased the on-current roughly 10,000-fold, from 1 nA to 10 μ A but similarly increased the off-current, resulting in current on/off ratios less than 2. In an effort to increase the on-current for devices on oxygen plasma treated substrates, S-SWCNTs deposition was performed by immersing the substrate into the S-SWCNT solution instead of drop-casting the solution onto the substrate. Transistors with immersion-deposited S-SWCNTs showed a 2-3 fold increase in on-current and more consistent on-currents from device to device, but required oxygen plasma treatment or mechanical cutting to remove CNTs deposited outside of the channel region. To try to reduce the off current for devices with oxygen plasma and lysine treated substrates, we tried increasing the amount of rinsing with toluene; however, additional rinsing had no significant effect on transistor performance.

3.4 Conclusions

In summary we presented characterization of screen-printed strain gauges, strain gauge arrays and transistors. Screen printed strain gauges were found to have gauge factors of 8.8 ± 0.3 with linear, hysteresis-free responses up to strain for up to at least 1.1% strain. These gauges also showed the same linear response and gauge factor after 10^5 cycles at 0.2% strain. Characterization via cross-sectional SEM showed a void-free microstructure,

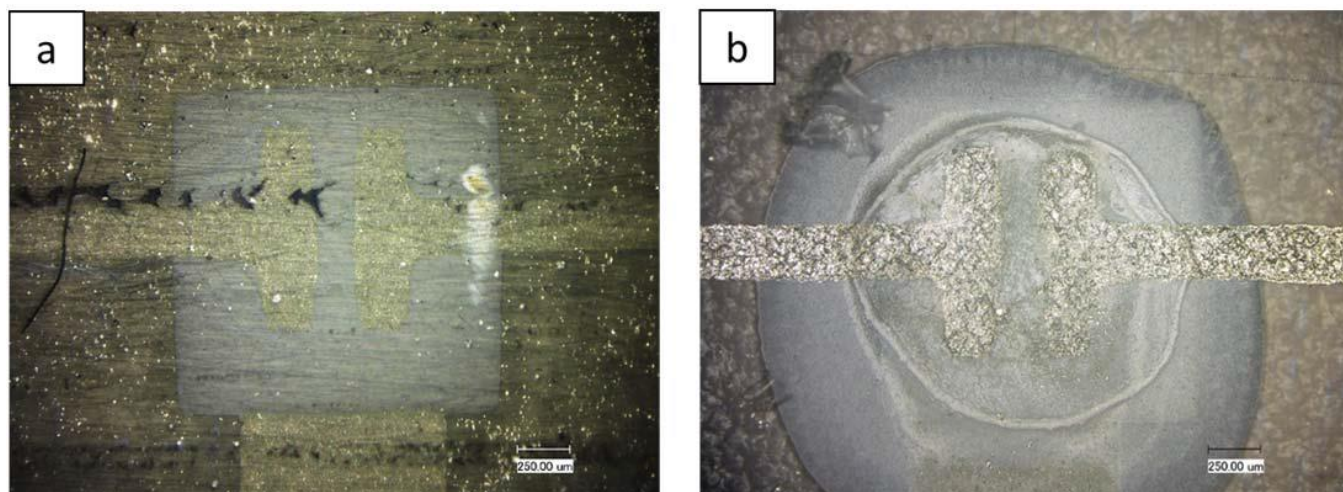


Figure 38. Optical images of transistors, (a) a top-gate transistor and (b) a bottom-gate transistor, showing the effects of the carbon nanotube solution when deposited first for top-gate transistors and last for bottom-gate transistors.

indicating the suitability of these gauges for strain applications. These gauges also showed temperature coefficients of resistance of $2.4 \times 10^{-3} \text{ K}^{-1}$. Overall these gauges showed promising results for use in arrays for structural health monitoring, but their resistances were too large for the processing circuitry.

Arrays of 64 screen printed strain gauges were prepared onto polyimide substrates and through optimization of the printing procedure, resistance tolerances were reduced to $\sim 20\%$. The temperature response of the carbon ink used for these arrays was $0.26 \times 10^{-3} \text{ K}^{-1}$ and the gauges showed linear responses to strain for up to at least 0.25% strain with gauge factors of 18.8 ± 0.7 . The ink used for the gauges in the arrays also showed a void-free microstructure. However, discrete transistors used for multiplexing in the strain gauge arrays debonded under strain. Therefore, flexible transistors, improved adhesion of the discrete transistors, or separate multiplexing circuitry is required to use these arrays in a strain monitoring application.

Transistors were screen printed and characterized and the printing process was changed numerous times to improve their performance and the printing repeatability. Optimization of the dielectric thickness and flattening the silver ink increased the printing repeatability and reduced the number of short circuits. Preparing transistors on alumina coated PET increased the on-current by a factor of $\sim 10,000$, but also increased the off-current. This increase in on-current was likely due to better adhesion of the S-SWCNTs on the rougher alumina surface and provided sufficient on-current that the transistors could be used for multiplexing. However, the alumina coating was damaged upon straining at 2% strain, damaging the printed transistors. Strain and fatigue measurements of transistors on uncoated PET also showed damage to the transistors. In this case, poor adhesion of the S-SWCNTs and overlying dielectric led to debonding in the channel region and cracking of the dielectric and gate layers. Therefore, further improvement of the adhesion of the printed materials to the PET substrate, a thinner, more flexible alumina coating or alternate materials are required for fabrication of transistors suitable for strain applications.

CHAPTER 4

Atomic Layer Deposition of Platinum on Collagen

4.1 Introduction

Conductive and flexible materials that are biocompatible have the potential for a wide range of biomedical applications including tissue engineering, [58–60] implantable neurological electrodes, [61–65] controlled drug delivery [66–70] and electrochemical actuators. [71–73] This class of materials belongs to ecofriendly or “green electronics” [74] materials which are benign to our surrounding environment. “Green” and “transient” technology refers to electronic devices and systems which, after stable operation, are capable of being resorbed within a defined period of time with minimal or non-traceable remains or byproducts. [75,76] While durability is a factor for stable performance of electronic devices, transient or biodegradable materials as well as biocompatible systems are gaining increasing attention in modern electronics. [75] Indeed, in the 21st century, electronic hazards or waste are one of the biggest problems for the environment. [76] This environmental challenge may be remediated using biodegradable transient electronics as they can resorb into the surroundings without any harmful impact. On the other hand, these transient electronics can also be used as biomedical diagnostic devices implanted into the human body, and thus eliminate the need of expensive follow up surgery to extract those devices from the body. [75,76] Following the concept of developing these kind of systems, the choice of green and transient materials is becoming attractive in modern biomaterial based electronics. [74,77] Selection of suitable materials is key to success of green and transient technology. These kind of materials are required to have some unique properties such as biodegradability, bioresorbability, and biocompatibility while being environmentally safe. [74,77,78] The advantages of using these materials are: low cost, energy efficient production due to their natural origin, no long term adverse effects, no need of retrieval as they can resorb by themselves, and above all they can minimize hazardous waste for our environment. [77] Previously, efforts have been made to develop this kind of electronics from transient materials mostly based on polymer (e.g., poly(vinyl alcohol) (PVA), polyvinylpyrrolidone (PVP), polylacticoglycolic acid (PLGA), polylactic acid (PLA), and polycaprolactone (PCL)) or metal (e.g., magnesium (Mg), molybdenum (Mo), iron (Fe) etc.) or semiconductor (e.g., silicon (Si), germanium (Ge), silicon nano-

membranes (Si-NMs) etc.) materials. [76] Partially transient or soluble electronics were developed based on organic substrates such as cotton and silk, where the device remained insoluble in spite of the substrates being soluble. [75] Recently, attempts have been made to develop completely soluble electronics. In those system, silicon (Si) substrate based fabrication was used due to the high solubility of silicon in body-fluids and even in water. [77] In silicon-based transient electronics, silicon dioxide (SiO_2), magnesium (Mg) and magnesium oxide (MgO) were used as gate dielectric, conductors and inter-layer dielectric, respectively. [77] Although these electronics are soluble, they are mostly inorganic substrate-based devices; as a result biocompatibility could be an issue for those devices used for implantable diagnostic devices where biocompatibility is a significant factor of the success of any such device. Additionally, silicon-based electronics materials or their byproducts may still leave some impact on our environment. Considering these aspects, potential usage of collagen as a substrate material is proposed in our study. Collagen has a triple helix structure composed of polypeptide chains and is an important biomaterial that is used in numerous biomedical applications. [78,79] Additionally, the structure of collagen contains the amino acids glycine and proline in the highest abundance. Collagen is a flexible biomaterial which is also biodegradable/bioresorbable, [80] biocompatible [80] and piezoelectric [78]. For these unique properties of collagen, it might be a good choice for applications in implantable electronics. Further, collagen is of natural origin and collagen-based electronics would be able to minimize any negative environmental impact. Flexible, biocompatible materials are desired in bioelectronics. Collagen is used in different biomedical applications due to its excellent biocompatibility and bioresorbability. However, it is not electrically conductive; therefore, deposition of a conductive metal film is required to turn collagen into an electrically conductive biomaterial, facilitating the fabrication of collagen-based flexible biocompatible electronics. On the other hand, transient electronics also require very thin layers of material film for its hopefully early dissolution into the surrounding environment.

Compared to different available thin film deposition techniques, atomic layer deposition (ALD) offers a unique approach to conformally deposit a very thin film (few Å or nanometers thick) of metal or metal oxide on high aspect ratio structural substrates; the stoichiometry as well as the thickness of such deposited thin film can be precisely tuned. [81,82] Low temperature (room or near room temperature) ALD processes are also necessary to functionalize heat-sensitive biomaterial organic substrates avoiding denaturation from higher temperature processing. Several attempts have been reported for coating biomaterials using ALD thin films after recognizing

the possibility of low temperature ALD reactions. [83] Previously, low temperature (ranging from 80-200°C) ALD of Pt was reported on different organic substrates including Nylon-6, polyethylene naphthalate (PEN) and polyethylene terephthalate (PET) polymer, cotton, paper, and human hair. [84–86] In this work, we report a Pt-ALD process at 150°C for the first time on a bio-resorbable collagen biomaterial and this enables ultrathin conductive Pt films conformally coated on collagen fibers, producing a flexible and conductive biomaterial which could potentially be used in a variety of applications such as implantable biosensor fabrication and electrogenic tissue regeneration.

4.2 Methods and Materials

4.2.1 Sample Preparation

All ALD processes were carried out in a custom built, horizontal hot wall tubular ALD reactor modified for low temperature ALD with a new mass flow controlled inert gas flow line and fast filling line (**Figure 39**). The reactor chamber consists of a 48 cm long quartz tube with an internal diameter of 38 mm. This reactor is heated using a tube furnace (1000 Series Marshall™ Tubular Furnace) connected with a proportional-integral-derivative temperature controller (OMEGA® CN9000A Series Miniature Autotune Microprocessor Controllers). The delivery lines consist of ¼-in stainless steel tubing and several pneumatic and manual valves. The reactor chamber is continuously evacuated using a vacuum pump (Fisherbrand™ Maxima™ C Plus Vacuum Pump, Model M8C) and the chamber pressure is monitored downstream of the reactor.

Deposition was performed at 150°C and 500 mTorr with the stainless-steel precursor bubblers at 50°C and the delivery lines in between the bubblers and reactor at 70-80°C. (Trimethyl)methylcyclopentadienylplatinum(IV) [MeCpPtMe₃] (99.999%-Pt PURATREM, Strem Chemicals Inc.) and ozone (1000 ppm generated just upstream of the reactor from 99.99% oxygen from Praxair using a custom made UV lamp system) were used as precursor and co-reactant, respectively for the Pt-ALD process. For TiO₂ deposition, TDMAT (Sigma Aldrich, 99.999%) was used as the titanium precursor and ozone was used as the oxidizer. Computer controlled pneumatic valves were used for sequential introduction of precursor and oxidizer while argon (99.999% from Praxair) was used for the precursor carrier gas and purging gas. Immediately following TiO₂ seed layer deposition, a Pt-ALD film was deposited on collagen without vacuum break. A commercially available collagen barrier membrane (Biomend®, Zimmer, USA) was used as the substrate in this study, and a highly-doped p-type Si(100) wafer (University Wafer,

Inc., USA) was used as a reference for measurement of the Pt thickness. Pt thickness on the reference silicon substrate was measured using spectral ellipsometry (Model M44, J.A. Woollam Co., Inc.). The ALD process on collagen samples is schematically represented in **Figure 40**. Non-coated collagen served as the control group, while collagen coated with 400 ALD cycles of Pt refers to Coll-Pt400, and Coll-TiO₂-Pt200 and Coll-TiO₂-Pt400 stand for 200 and 400 ALD cycles of Pt respectively on collagen samples with a ~9 nm seed layer of TiO₂ deposited at room temperature.

4.2.2 Surface Characterization

High-resolution field emission SEM (JEOL JSM-6320F, JEOL USA, Inc.) was used to analyze The surface morphology of the pristine collagen and Pt-coated collagen substrates. The collagen surface after ozone exposure was analyzed using an Electron-Beam Lithography system (Raith 100) for SEM. Prior to SEM, a sputter coater was used to deposit a gold coating to make the samples conductive. The chemical composition of the surfaces of the control collagen and ALD Pt-coated collagen substrates was examined using X-ray photoelectron spectroscopy (Kratos AXIS-165, Kratos Analytical Ltd., United Kingdom) equipped with a monochromatic Al Ka (1486.6 eV) X-ray source operated at 15 kV and 10 mA. In addition to SEM, the surface of the native collagen and Pt-coated collagen was imaged using a Keyence VHX6000 optical microscope at 500x magnification using Keyence's depth scanning mode.

4.2.3 Electrical Characterization

Ag-530 conductive silver ink (Applied Ink Solutions) was manually screen printed onto the thin films to provide consistent probe locations, reduce contact resistance and protect the films from damage during electrical measurements. Screen printing was done using a Gold Print SPR-25 screen printer, a 70 durometer (Shore A) squeegee blade, and a printing offset of 3 mm. The screen used had wire diameters of 228.6 μm , with 325 wires per inch set at a mesh angle of 45°. The line pattern used had four lines with line widths of 0.5 mm, line spacing of 1 mm and line lengths of 5 mm. After printing, the silver ink was dried in a laboratory oven at 100°C for two hours with filtered air flow (15.6 L/min) across the heating elements supplied via an aquarium pump (Hydrofarm) connected to a 5-micron air filter.

Two-probe resistance measurements were performed with a Keysight E4980AL precision LCR meter and a Micromanipulator probe station with tungsten probes in Micromanipulator 210 probe holders (**Figure 41**).

Measurements were done using a 10 mV, 20 Hz signal with a 1.5V DC bias. Probe resistance and contact resistances were measured and subtracted to determine resistance of the platinum films. Probe resistance was measured as 0.4 Ω by directly connecting the tips of the probes. Contact resistance was calculated using Equation (1) below, where R_{14} , is the resistance between contacts one and four, R_{12} is the resistance between contacts one and two, R_{23} is the resistance between contacts two and three and R_{34} is the resistance between contacts three and four.

$$R_c = \frac{R_{14} - (R_{12} + R_{23} + R_{34})}{2} \quad (1)$$

Volume resistivity was calculated using Equation (2) below, where R is the average of R_{12} , R_{23} , and R_{34} minus the probe resistance and contact resistance, w is the width of the sample, t is the film thickness, and l is the spacing between the contacts.

$$\rho = R \frac{wt}{l} \quad (2)$$

Strain was applied by bending samples over various curved surfaces ranging from 10.5 cm to 1.7 cm in diameter and the resistance was measured before and after strain. Strain from the curvature was calculated using Equation (3) where γ is the distance of the film from the neutral axis, ρ is the radius of curvature, t is the film thickness, and r is the radius of the curved surface. This equation neglects the effect of the ALD films on the location of the neutral axis as the effect is negligible since the thickness of the ALD films is less than 40 nm while the substrate thickness is $\sim 265 \mu\text{m}$.

$$\epsilon = \frac{\gamma}{\rho} = \frac{\frac{t}{2}}{r + \frac{t}{2}} \quad (3)$$

The collagen samples were also connected to a light-emitting diode (LED) circuit with a 3 volt battery to test for the presence of a stable conductive coating on the collagen surface and to study the flexibility of the existing conductive coating.

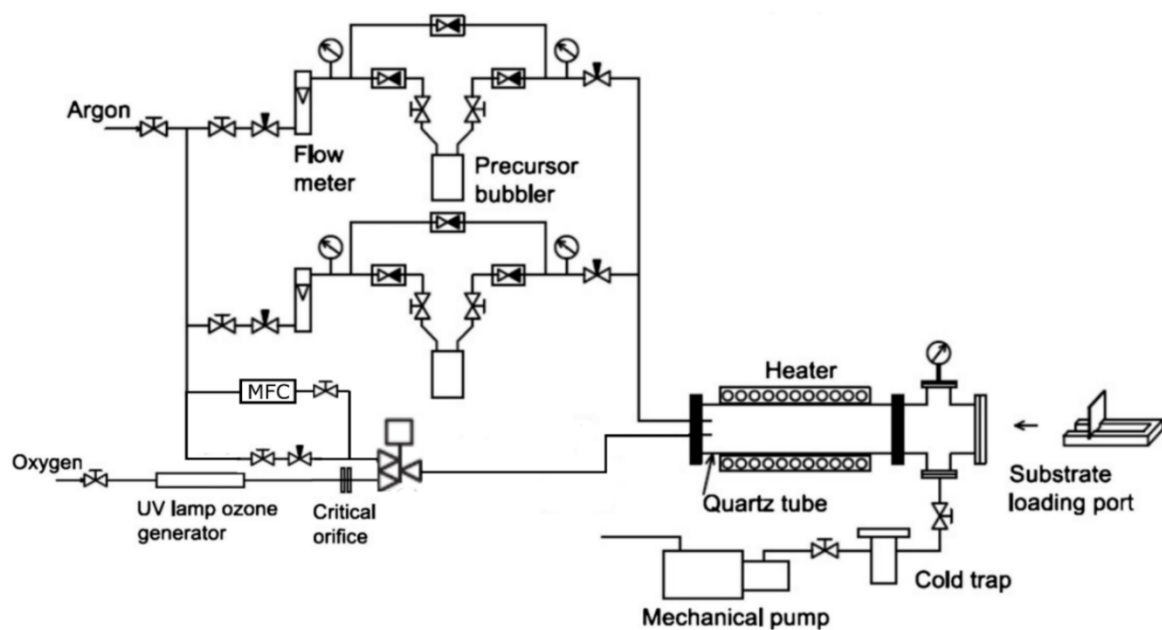


Figure 39. Schematic of the custom-built ALD reactor used for deposition onto the collagen membrane.

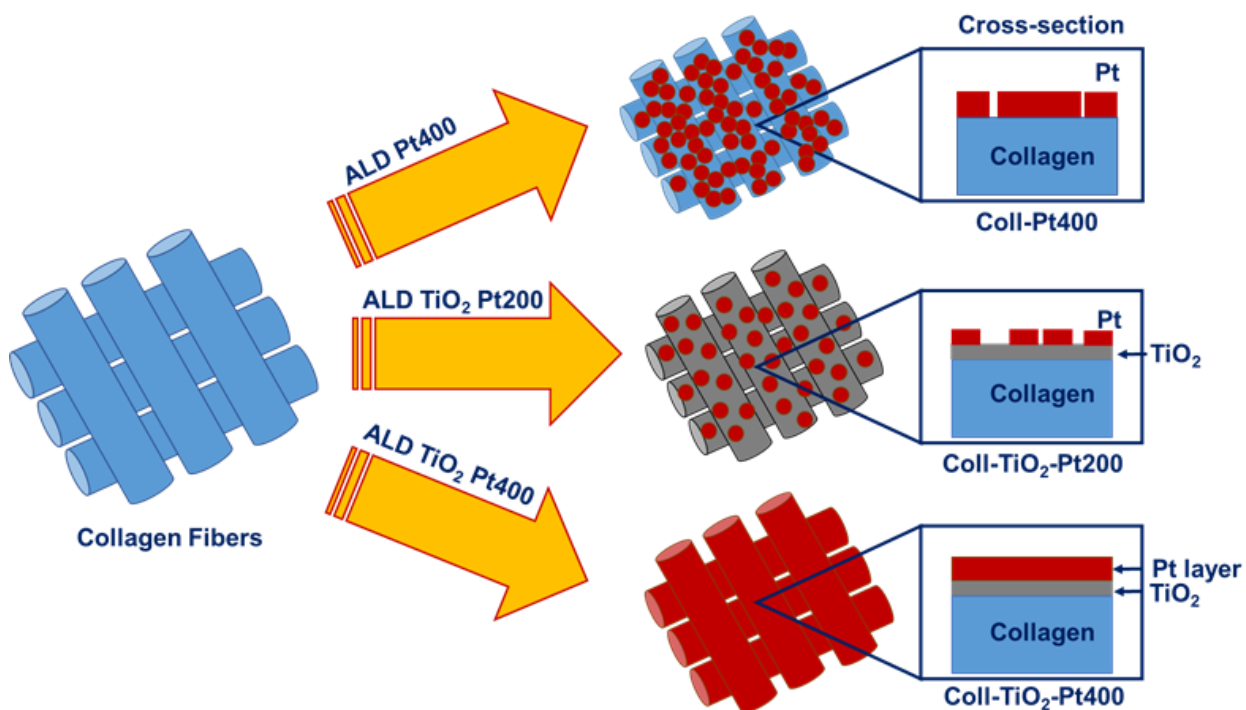


Figure 40. Schematic representation of the ALD process for preparing different collagen sample groups.

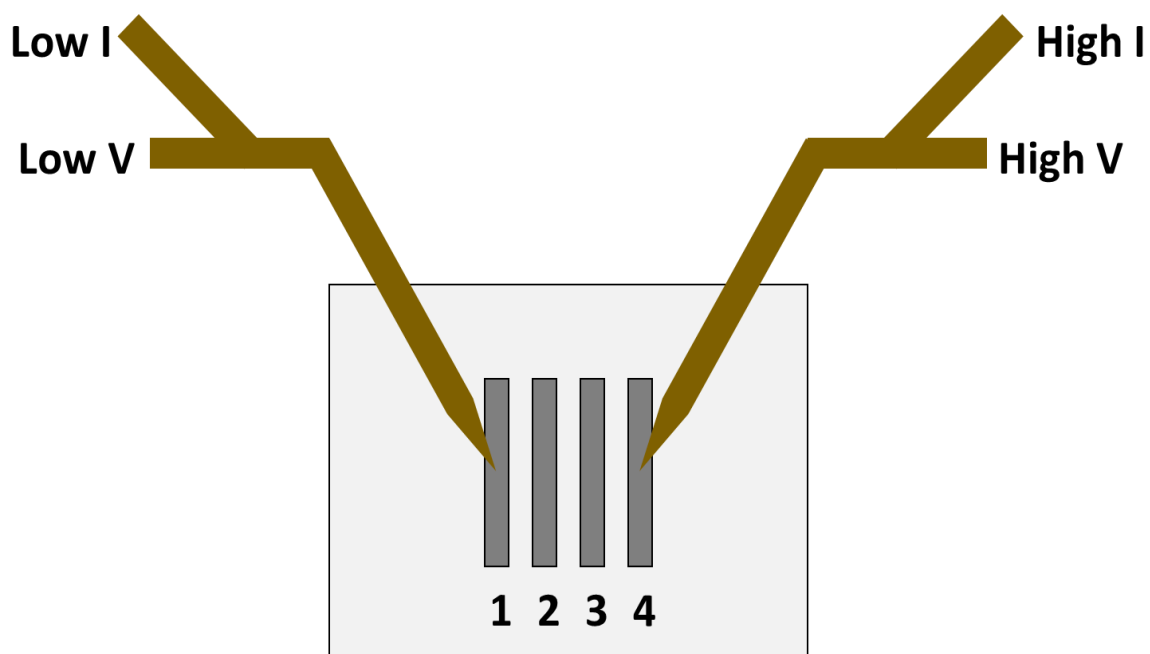


Figure 41. Diagram of the electrical measurement setup. 1, 2, 3, and 4 indicate the contact numbers for the screen-printed silver ink contacts. Low V and High V indicate the low and high potential connections to the LCR meter, and Low I and High I indicate the low and high current connections to the LCR meter.

4.3 Results

Thickness of the ALD deposited Pt thin film on reference Si samples, used while performing ALD on collagen samples, is reported in **Table VI**. In this process, 200 ALD cycles deposited around 11 nm of Pt film on the reference Si sample and 400 ALD cycles deposited ~26 nm of Pt film on the reference sample. Surface features of the collagen samples were investigated using optical microscopy before and after the Pt ALD process was carried out. ALD Pt coated collagen surfaces exhibited different surface characteristics compared to the non-coated collagen surface (**Figure 42**). Although difficult to discern, the non-coated control surface shows a textured or woven, fiber surface with peaks and valleys similar to the Coll-Pt-400 group. In contrast, a near flat surface was found for both Coll-TiO₂-Pt200 and Coll-TiO₂-Pt400 groups. These two groups have a seed layer of TiO₂ thin film on their surfaces and Pt ALD was performed on top of this TiO₂ layer. This layer could fill the gaps of the surfaces, and as a result, a smoother surface was obtained. SEM was performed to have in-depth understanding of surface morphology at the nanoscale and to assess the effect of heating and ozone on the morphology of the collagen fibers. SEM micrographs for all the collagen sample groups are displayed in **Figure 43**. For the non-coated control, the surface structures were fibrous and the characteristic “banding” pattern of individual collagen fibrils, the make up

Sample	Pt film thickness on monitor Si [nm]	Average Volume Resistivity [Ω cm]	Standard Deviation of Volume Resistivity [Ω cm]
Control	-	$>10^{12}$	-
Coll-TiO ₂ -Pt200	11.2 \pm 0.9	$>10^{12}$	-
Coll-Pt400	26.7 \pm 0.4	6.65 $\times 10^{-3}$	2.85 $\times 10^{-3}$
Coll-TiO ₂ -Pt400	27.8 \pm 1.4	2.95 $\times 10^{-3}$	3.06 $\times 10^{-5}$

TABLE VI. ELECTRICAL RESISTIVITY OF THE CONTROL NON-COATED AND ALD PT COATED COLLAGEN SAMPLE GROUPS AND THE CORRESPONDING PT FILM THICKNESS AS MEASURED ON REFERENCE SI SAMPLES.

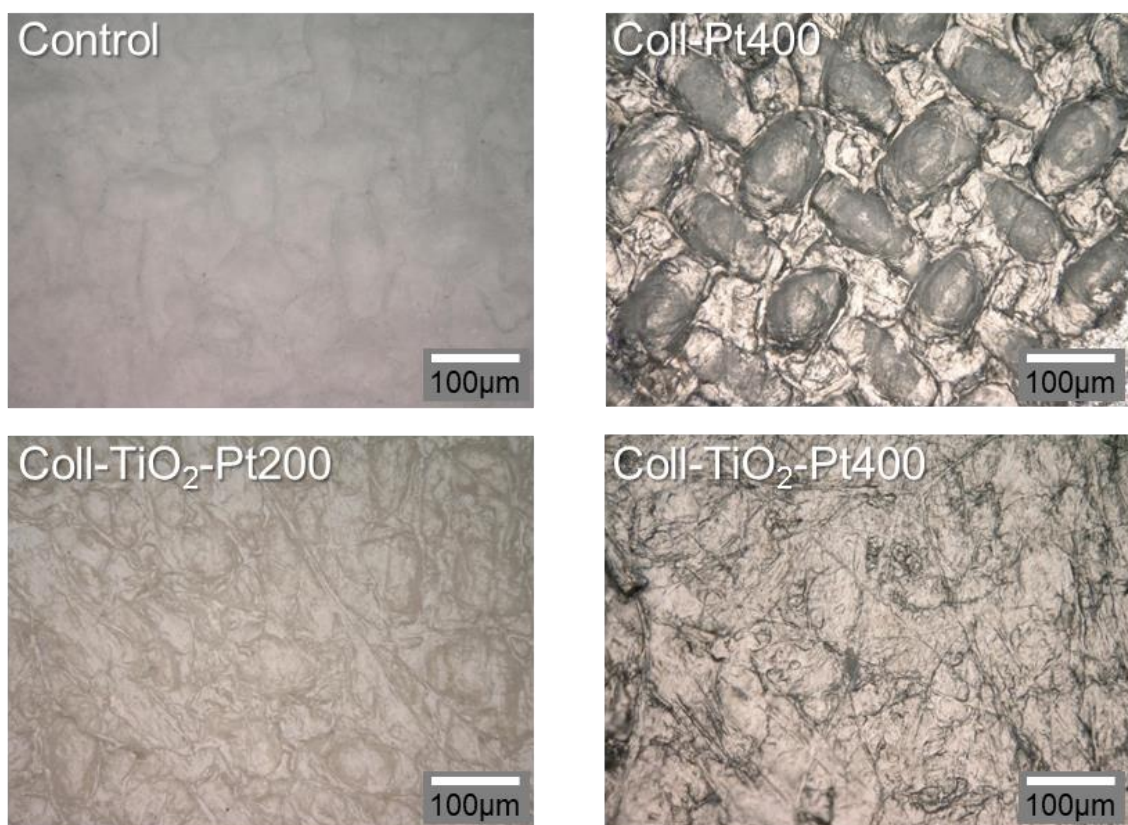


Figure 42. Optical microscopy images of collagen films coated with platinum or titanium dioxide and platinum at 500x magnification showing the surface features of the collagen samples. The control sample is a collagen membrane as received. The Coll-Pt400 sample has 400 ALD cycles of platinum on a collagen. The Coll-TiO₂-Pt200 and Coll-TiO₂-Pt400 samples have ~9 nm of TiO₂ and 200 and 400 ALD cycles of Pt, respectively.

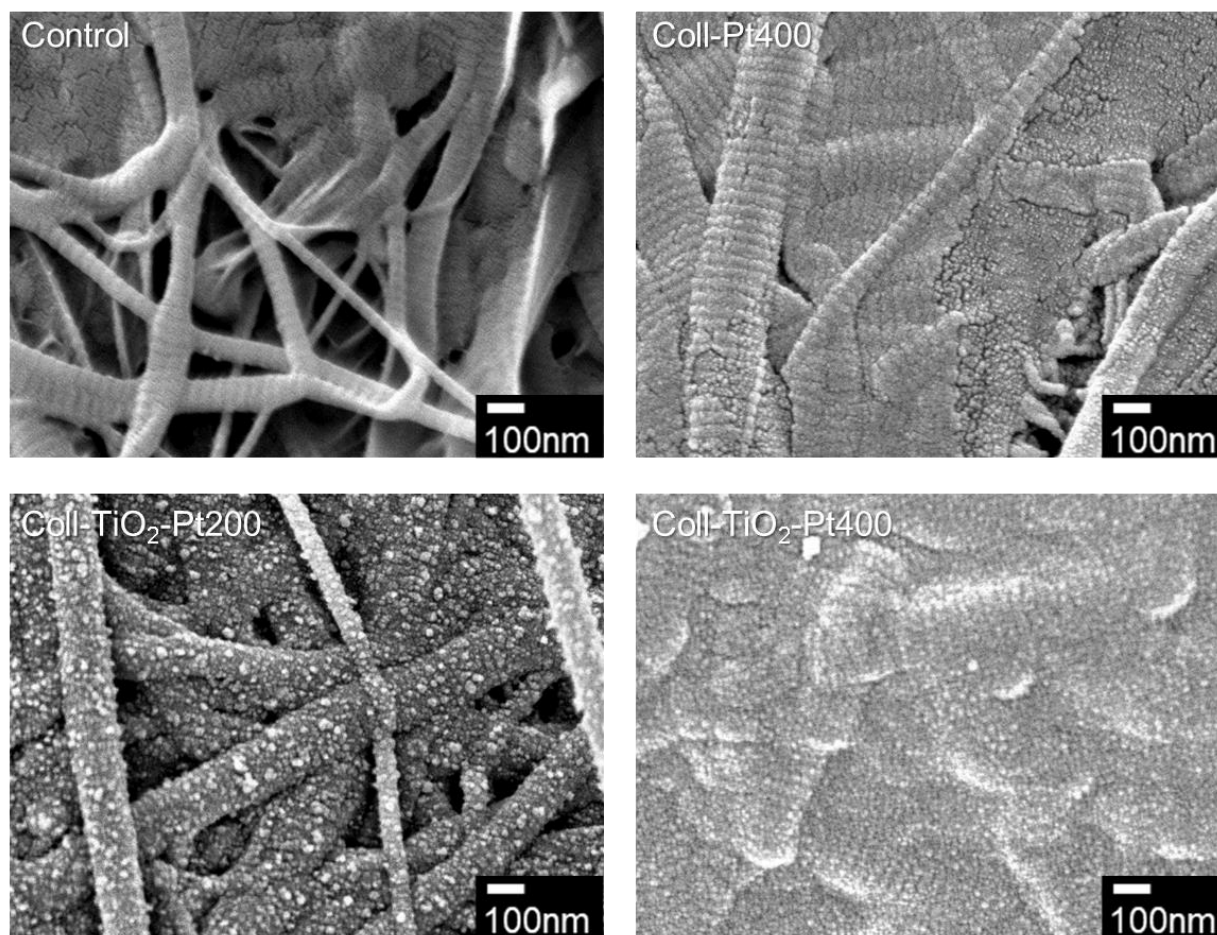


Figure 43. SEM images of the collagen films with ALD Pt or ALD TiO_2/Pt at 50,000X magnification showing the surface morphology at the nanoscale. The control is the pristine collagen sample, Coll-Pt400 has 400 ALD cycles of Pt, Coll- TiO_2 -Pt200 and Coll- TiO_2 -Pt400 are coated with ~ 9 nm of TiO_2 and 200 ALD and 400 ALD cycles of Pt, respectively.

of the larger anatomic fibers, was clearly visible. This collagen based membrane is manufactured from type I collagen fibers purified from bovine tendon. [87] Similar characteristic striping of collagen fibrils was reported before from the electron micrograph of untreated bovine tendon collagen tissue. [88] ALD Pt-coated collagen samples exhibited significantly different surface morphology as compared to the non-coated control. A conformal and uniform ALD coating with different Pt nucleation and different surface coverage was observed among the coated samples. In Coll-Pt400, the characteristic bands were still noticeable, and a conformal Pt film was observed although the surface coverage does not appear to be 100%. For the Coll-TiO₂-Pt200 group, the island growth behavior of Pt was observed on collagen fibers coated with a seed layer of TiO₂ thin film and the Pt nuclei do not appear to be connected. On the other hand, a continuous, conformal Pt film was obtained for the Coll-TiO₂-Pt400 group with 100% surface coverage. This result supports our observation from optical microscopy where the Coll-TiO₂-Pt400 appeared smooth and uniform in color due to the continuous Pt coating which filled the gaps of the collagen membrane.

The SEM results indicated that the TiO₂ seed layer acted as a buffer layer to promote the nucleation of Pt on the collagen surface. Additionally, it revealed that 400 ALD cycles of Pt seem to be required to obtain a continuous Pt film that fully covers the collagen/titania nano-film surface with the conditions used. A collagen molecule consists of amide functional groups. Reactivity of the MeCpPtMe₃ precursor towards organic amide groups has not been well-studied. However, it was previously reported that a thin layer of alumina (Al₂O₃) promoted the nucleation of Pt on Nylon-6 consisting of amide backbone. [84] The Al₂O₃ layer was deposited at higher temperature, i.e., at 200°C through ALD and it was reported to promote Pt nucleation on Nylon-6. [84] A 3 nm-thick Al₂O₃ film deposited using plasma assisted ALD was also reported to facilitate Pt growth on PEN, PET, paper and cotton. [85] On the other hand, ALD TiO₂ thin films deposited at 100°C from titanium tetrachloride (TiCl₄) and water, was reported to promote Pt nucleation on Silicon (Si(001)) due to the hydrophilicity of the TiO₂ film. [89] Xu et al also showed that hydrophilic OH-terminated silicon surface resulted in much higher surface coverage of Pt thin film compared to H-terminated hydrophobic surface. [90] Therefore surface hydrophilicity appears to be one of the main factors in nucleation of Pt as hydrophilic surfaces offer a higher number of nucleation sites to facilitate the ALD process. [90,91] Recently we developed a room temperature ALD process to deposit amorphous TiO₂ thin film on collagen surface. [92] Amorphous TiO₂ film was reported to be hydrophilic due the abundant hydroxyl or -

OH group present on the film surface. [93] Consequently, our amorphous TiO_2 seed layer could help with better nucleation of Pt on the collagen surface. Furthermore, previous reports indicated that after 400 cycles of the Pt ALD process, 100% surface coverage of Pt film was achieved on Si samples. [86,90,94] Therefore our finding is in general agreement with previously published reports.

SEM micrographs of the collagen film after 5 and 10 minutes of ozone exposure and heating at 150°C are shown in **Figure 44**. As seen in this figure, the collagen fibers show the same characteristic banding as the control sample (**Figure 43**) even after heating and ozone exposure. Additionally, no significant change was observed in the morphology or size of the fibers to indicate the heating or ozone affected the collagen fibers. Therefore, the ALD process as well as extended ozone exposure do not appear to damage the collagen fibers.

ATR-FTIR was employed in absorbance mode to study the chemical composition of the collagen samples (**Figure 45a**). The principle behind the FTIR technique is that there are different absorption intensities of the incident IR from the covalent bonds of different biomolecules present in specimen, and depending on the molecular bonds and structure, chemical information can be obtained from the resultant IR absorption intensity and wavenumber positions. [95] As shown in **Figure 45a**, all collagen sample groups exhibited absorption of IR for scan region from $3900\text{--}600\text{ cm}^{-1}$. Predominant amide peaks were identified for all groups and these amide groups are functional groups for collagen type I. Amide peaks observed at wavenumbers $1700\text{--}1650\text{ cm}^{-1}$, $1600\text{--}1500\text{ cm}^{-1}$, $1300\text{--}1200\text{ cm}^{-1}$ correspond to Amide I, Amide II and Amide III, respectively, while $3330\text{--}3300\text{ cm}^{-1}$, $3080\text{--}2900\text{ cm}^{-1}$ can be attributed to Amide A and Amide B, respectively. [95,96] Peaks observed at 1035 cm^{-1} and 1079 cm^{-1} are attributed to $\nu(\text{C-O})$ and $\nu(\text{C-O-C})$. [95] No major peak shift or significantly different peak was observed for our ALD-Pt coated groups compared to the non-coated control. This finding suggests that our ALD process is capable of functionalizing the collagen substrate without significantly altering the intrinsic properties or biomolecular structures of collagen.

X-ray photo electron spectroscopy was used in surface characterization, specifically with the aim of evaluating the quality of the Pt thin film deposited on the collagen surface using the ALD process at 150°C . The XPS spectra of the Coll- TiO_2 -Pt sample group is displayed in **Figure 45b**. Figure 3b shows the two major peaks of the Pt core-level energy region of XPS spectra. The peaks at 74.2 eV and 71 eV are attributed to metallic $\text{Pt}_{5/2}$ and $\text{Pt}_{7/2}$, respectively. Deconvolution of peaks of other structures were reported to result in typically 72.3 eV and 73.8

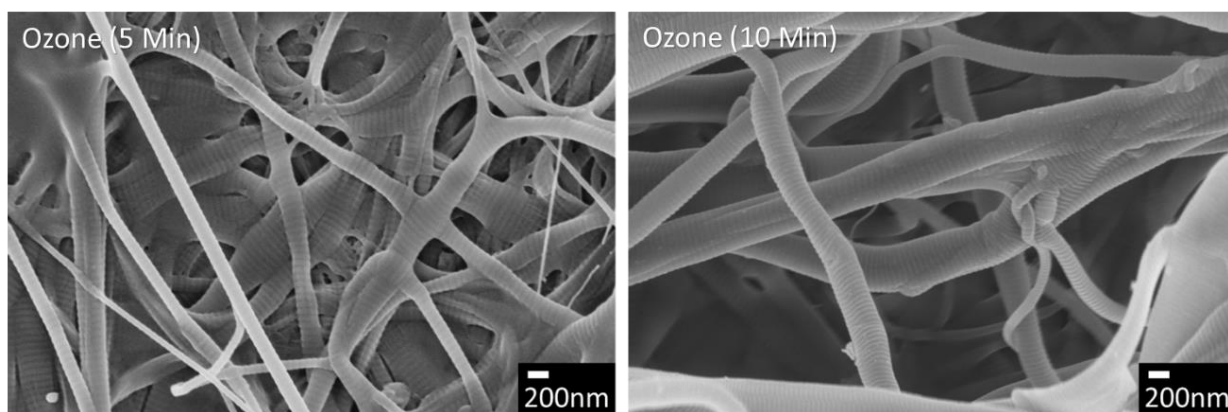


Figure 44. SEM images of the collagen films after 5 and 10 minutes of ozone exposure at 20,000X magnification showing the morphology of the collagen fibers.

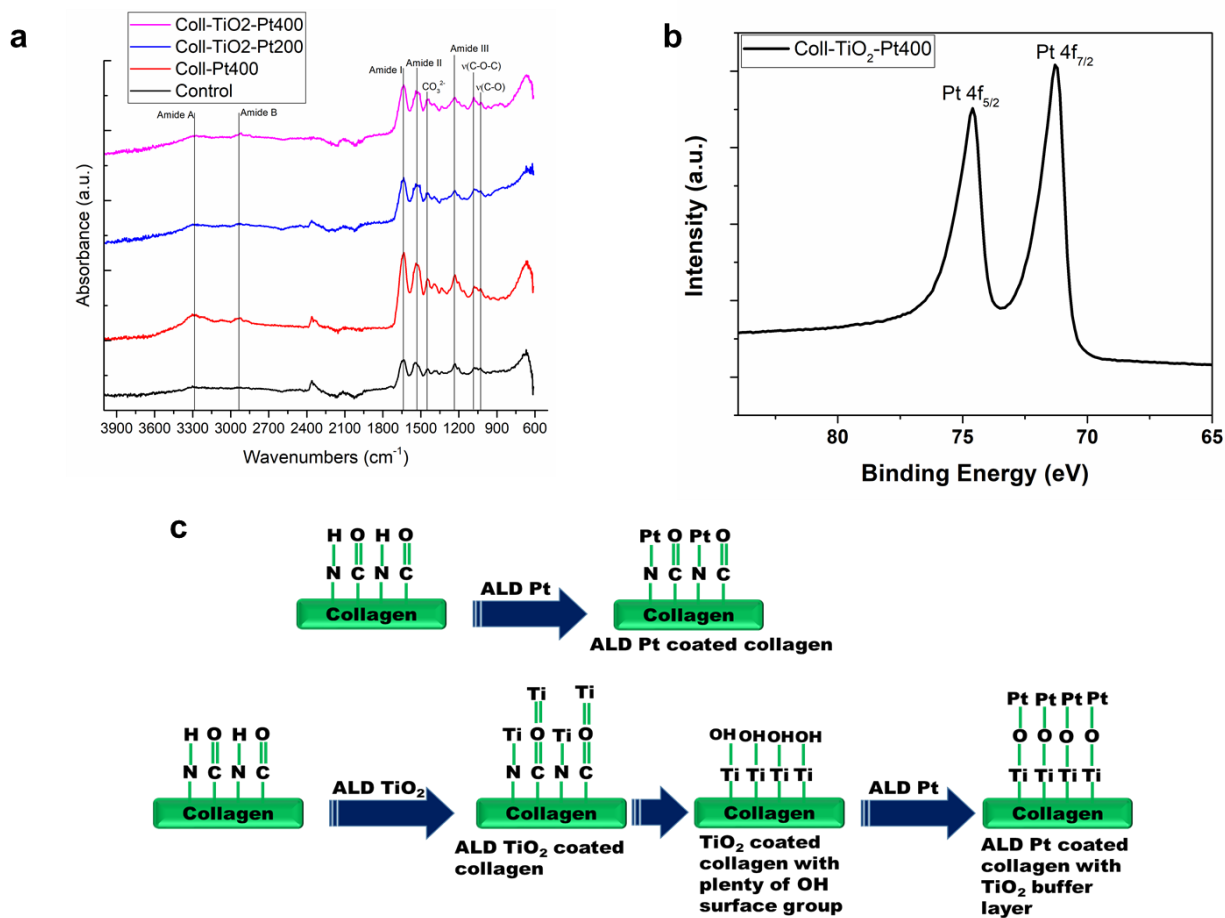


Figure 45. Chemical analysis of collagen samples. (a) ATR-FTIR spectrum of collagen sample groups. (b) X-ray photoelectron spectra of the Coll-TiO₂-Pt400 group showing Pt core level energy region. (c) Proposed chemical bonding of ALD-Pt coating with the collagen molecule.

eV peaks, likely due to the formation of PtO_x . [86,94] Therefore our XPS result indicates that our ALD Pt film is a high purity metallic film despite being deposited at 150°C on an organic substrate, i.e., collagen.

A chemical structure was proposed in **Figure 45c** for ALD Pt coated collagen with and without the ALD TiO_2 buffer layer. Platinum was previously reported to chemically bind with DNA by forming a favorable bond with nitrogen atoms (at N7 sites) of the adenine and guanine base of the DNA molecule. [97,98] Therefore, the Pt ALD coating might bind with the available surface nitrogen of the collagen membrane. On the other hand, the bonding might be different when a TiO_2 buffer layer was present between the Pt coating and collagen. As reported earlier, the ALD TiO_2 coating on collagen most likely formed new titanium (Ti) mediated bonds with nitrogen and carbonyl groups of the collagen molecule, presumably substituting hydrogen (H) in the $\text{N-H}\cdots\text{O}=\text{C}$ bond with Ti. [99] In our previous work, we reported that this ALD TiO_2 coating on collagen deposited at room temperature was amorphous in nature. [92] Also, amorphous TiO_2 thin film was reported to have plenty of surface hydroxyl (OH) groups. [93] Therefore, in post-ALD TiO_2 , the Pt coating could bind with the oxygen (O) atoms of the available surface OH groups of the TiO_2 coated collagen, as previously suggested in the chemisorption process of MeCpPtMe_3 on -OH functionalized surfaces. [100]

Pt growth initiation and nucleation behavior could also be visually observed as depicted in **Figure 46a**. The control collagen membrane is white while darkening of sample was observed after performing different ALD treatments on the collagen surfaces. After 400 cycles of ALD Pt (i.e., Coll-Pt400), the white collagen became darker suggesting nucleation of Pt on the collagen surface. For Coll- TiO_2 -Pt200, the sample is slightly darker compared to control but not as dark as Coll-Pt400. This was expected because ALD is a cyclic process and consequently 200 ALD cycles resulted in a smaller film thickness (~ 2 times less in this case) as compared to 400 ALD cycles. Finally, for the Coll- TiO_2 -Pt400 group, a uniformly coated dark sample surface was observed suggesting 100% surface coverage with the highest level of Pt nucleation. These observations from our visual inspection corroborated our finding through optical and electron microscopy. Darkening of the sample due to Pt film growth was also reported previously for Nylon-6 substrate after performing Pt ALD on the surface. [84]

A simple test was performed involving a LED to qualitatively prove the presence of a conductive metal film on the collagen surface (**Figure 46b**). Collagen itself is a non-conductive organic biomaterial and as a result it could not complete the circuit to light up the LED. For Coll- TiO_2 -Pt200, lower growth of Pt was observed on the

collagen surface, and these samples were also not conductive enough to light up the LED. Although for Coll-Pt400, growth of Pt was observed, the LED lit up few times on some portions of the sample surface, while most of the time it would not light up the LED. This indicated that the Pt film on Coll-Pt400 was not fully continuous to be conductive. On the other hand, the LED lit up for the Coll-TiO₂-Pt400 sample group. This indicated that a continuous conductive Pt thin film on the surface of Coll-TiO₂-Pt400 was achieved.

After determining that some of the platinum coatings on the collagen surfaces were conductive, two-probe resistance measurements were performed on the native collagen, Coll-Pt400, and Coll-TiO₂-Pt400 samples to measure the resistivity quantitatively. The resistance of the native collagen, and Coll-TiO₂-Pt200 were above 10^{18} Ω , the upper range of our LCR meter; however, the resistances of the Coll-Pt400 and Coll-TiO₂-Pt400 samples were well within the range of our LCR meter. The average volume resistivity and standard deviation of the volume resistivity of three measurements from three different points on these samples is shown in **Table VI**. The volume resistivity was calculated using the thickness of Pt measured from silicon substrates. The larger standard deviation of the volume resistivity for the Coll-Pt400 as compared to Coll-TiO₂-Pt400 is likely due to larger variation in resistance among R_{12} , R_{23} , and R_{34} as depicted in **Equation 2 (Figure 41)** and is indicative of a less uniform Pt coating. In addition to the Pt on collagen, the resistivity of 400 cycles of Pt were also measured on silicon. This silicon sample had an average volume resistivity of 31.8 $\mu\Omega$ cm, approximately 10 times lower than the Coll-TiO₂-Pt400 sample, with a standard deviation of 15.1 $\mu\Omega$ cm. The lower volume resistivity on silicon is likely due to the smooth, non-porous surface which allows for more interconnection between the Pt coating; therefore, it is important to compare the resistivity with platinum deposited on similar substrates. The volume resistivity of 12 nm of Pt on Nylon-6 is reported as 175 $\mu\Omega$ cm. [84] This resistivity of Pt coated Nylon-6 is lower than our Pt coated collagen likely due to the more ordered, less porous structure of Nylon-6 compared to collagen.

To characterize the flexibility of the platinum coatings, their resistances were measured before and after bending at different radii of curvature as shown in the inset of **Figure 46c**. The radii of curvature ranged from 10.5 to 1.7 cm and induced strains as high as 1.5%. The results of these resistivity measurements after bending, are shown in **Figure 46c**. Less than one percent change in volume resistivity was measured after straining up to approximately 8200 microstrain for the Coll-Pt400 sample; however, a 1.4% increase and 11.1% increase were measured after straining at 9700 and 15100 microstrain, respectively. For the Coll-TiO₂-Pt400 sample, 5%, 10%,

and 20% increases were measured after straining at approximately 4200, 8200, and 15100 microstrain. The larger increases in resistivity with microstrain for the Coll-TiO₂-Pt400 sample is due to the 9-nm thick TiO₂ coating. This TiO₂ coating increases the film thickness by approximately 37% and may affect the adhesion of the coating. Both thicker films and lower adhesion strengths have been shown to cause cracking or failure of thin films at lower strains. [101] In comparison to the work by Mundy et al, which showed only a 7% decrease in conductivity for a radius of curvature of 6.0 mm or ~7.7% strain, our results show similar decreases below 1% strain. [84] The larger change for our samples could be due to a number of different factors including the different seed layer used for the platinum deposition, the larger thickness of our seed layer, the less ordered structure of the collagen compared to Nylon-6, and the different deposition conditions used. Additionally, the work by Lee et al showed only a 2% change in resistance after 1000 cycles of bending at a radius of 3 mm or ~8.4% strain for Pt deposited on cotton fibers. [86] Despite the larger change in resistivity of our films, they remained quite conductive as demonstrated by our Coll-TiO₂-Pt400 providing sufficient conductivity to illuminate a LED while in a flexed state (**Figure 46d**).

4.4 Conclusions

Successful ALD of Pt thin film was achieved at 150°C on a collagen biomaterial for the first time. It was found that 400 ALD cycles of Pt was sufficient to obtain 100% surface coverage of Pt on the collagen. A 9 nm seed layer of amorphous TiO₂ layer, deposited using room temperature ALD prior to Pt ALD, was shown to promote higher nucleation to achieve a continuous Pt thin film. Surface chemical analyses confirmed the presence of a pure metallic Pt film on collagen surface. A simple LED test qualitatively confirmed the existence of a conductive thin film on the collagen surface. Furthermore, electrical measurements showed that resistivity of 295 $\mu\Omega$ cm was achieved for Pt coated collagen sample with a TiO₂ seed layer, while control non-coated collagen was highly resistive (resistivity > 10¹² Ω cm). Therefore, our low temperature ALD-Pt process is suitable to functionalize heat sensitive biomaterials by successful deposition of a conductive metal thin film. This novel flexible and conductive biomaterial can potentially be used in wide range of applications. Consequently, future work will focus on its application as electrodes in tissue engineering, bioimplants, and as a basis for biosensor devices.

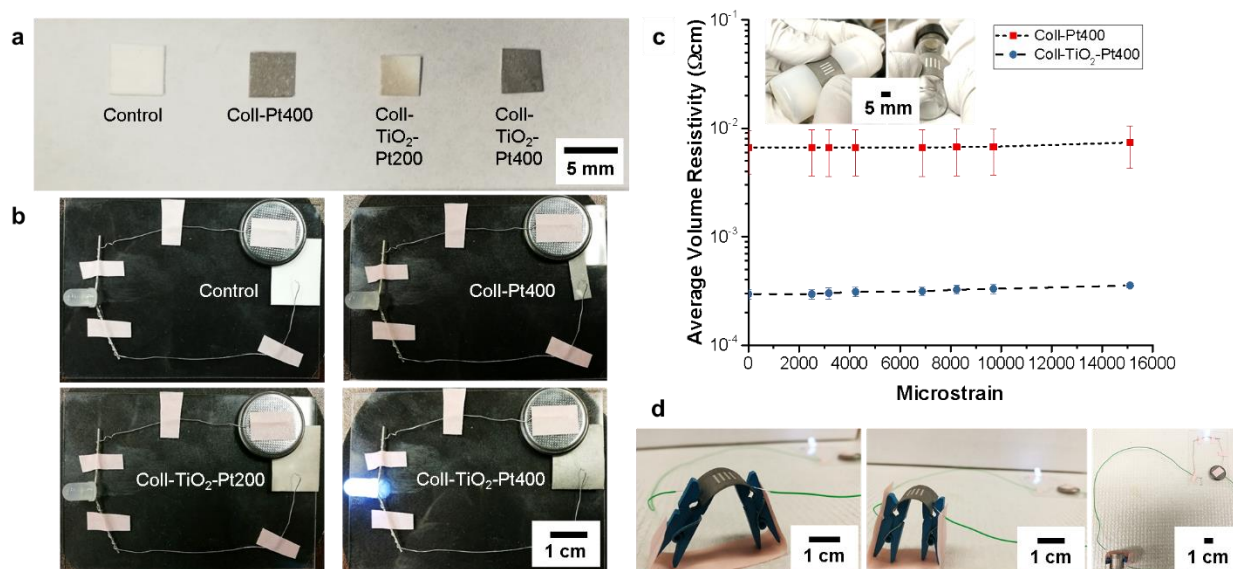


Figure 46. (a) Photograph of all the collagen sample groups showing color difference due to Pt nucleation on collagen surfaces. (b) Photograph of electrical conductivity test using LED light showing only Coll-TiO₂-Pt400 provided sufficient conductivity to illuminate the LED, but sufficient conductivity was not provided by the other sample groups. (c) Average volume resistivity versus microstrain for the Coll-Pt400 and Coll-TiO₂-Pt400 samples. Error bars indicate the standard deviation of the volume resistivity from three measurements on each sample. Inset photographs show the bending of ALD-Pt coated collagen samples. (d) Photograph of the flexible Coll-TiO₂-Pt400 sample that provided sufficient conductivity to illuminate the LED while the sample was in a flexed state.

CHAPTER 5

On the Selective Atomic Layer Deposition of Zirconium Oxide on Electroplated-Based Copper Substrates

5.1 Introduction

Selective atomic layer deposition (SALD) is vital for downscaling nanoelectronics as it provides a means of self-aligned and bottom-up fabrication. Together these allow for sub-5nm critical dimensions as alignment is no longer an issue, while reducing the number of fabrication steps and overall cost.[102–104] Atomic layer deposition (ALD) is one of the main deposition methods of interest due to its ability to deposit uniform, pin-hole free layers with precise thickness control. However, for ALD to be an ideal bottom-up fabrication process, materials need to be selectively deposited. Selectivity of ALD can be performed with either area-deactivation or area-activation of the substrate. Area-activation SALD primarily relies on the generation of a seed layer on the growth area which serves as nucleation sites for subsequent ALD while area-deactivation SALD typically relies on self-assembled monolayers (SAMs) or polymers to prevent deposition on the non-growth area. In area-activation SALD, oxides serve as the non-growth area; however, as metal oxides and nitrides often nucleate on these oxides, area-activation SALD is best suited for deposition of metals.[103,105] Area-deactivation via SAMs represents the majority of literature on SALD and with careful selection of the molecules used, this approach can be used for both metals and metal oxides.[103] The downside of using SAMs or polymers is that they generally have low thermal stability and may be difficult to remove if excessively heated.[103,104] Additionally, SAMs typically require long assembly times to form a well-packed monolayer and precursor adsorption on SAMs can reduce selectivity.[103,106] Furthermore, both SAMs and polymers must be removed after deposition.[103] On the other hand, area-deactivation SALD using thermally stable materials intrinsic to the design of interest such as metals can provide a more efficient approach. This approach does require selective adsorption of precursor or co-reactant on specific materials of the patterned surfaces but eliminates the removal step making the overall SALD process much more efficient.

Several materials including HfO_2 [107], ZrO_2 [108], TiO_2 [109], and Ru[110] have been selectively deposited by exploiting longer nucleation times of the precursors on metals than on silicon. Of these materials, ZrO_2 is of particular interest due to its potential use in capacitors[111], field effect transistors[112,113], solid oxide fuel

cells[114], protective coatings[115] and catalysis[116]. For ZrO_2 , selective deposition is believed to be due to an electron-beam evaporated copper surface having minimal surface oxides, which thereby had minimal nucleation sites for ALD.[108] Although evaporated copper is suitable for small-scale fabrication, high-volume manufacturing typically relies on electrolytically plated copper.[117] In comparison to evaporated copper, electroplated copper is typically lower purity due to additives and electrolytes from the plating process.[117] Impurities such as sulfur and chlorine are expected from the plating process, but their effect on the SALD process has not been studied.[117]

Reduction of copper oxides has been studied using numerous chemicals including CO [118,119], H_2 [120], ethyl alcohol[121–124], methanol[121], isopropanol[121] and formic acid[121]. Of these chemicals, ethyl alcohol (EtOH) was chosen as it has been demonstrated to be capable of reducing copper oxides while serving as an oxygen source for ALD of metal oxides[107,108]. With EtOH vapor supplied at room temperature, CuO is reported to reduce at a rate of $\sim 0.01\text{--}0.02$ nm/sec with a reactor temperature of 200°C [122,123]. Satta et al. also report reducing cuprous oxide (Cu_2O) at a faster rate, ~ 1 nm/sec, and so it is expected that Cu_2O is of less concern when trying to reduce a copper surface to an oxide free, metallic Cu [122]. Considering these reduction rates, thicker layers of CuO could dramatically increase the amount of time needed for reduction, while thicker Cu_2O would have less effect.

Previous work from our lab has demonstrated SALD of ZrO_2 on patterned silicon and electron beam evaporated Cu substrates, where gaseous diffusion of reaction byproducts was believed to influence selectivity[108]. In this present work, we report SALD of zirconia on separate electroplated copper and Si substrates and show an increased selectivity by optimizing EtOH vapor exposure to the substrates prior to deposition, referred to as pretreatment. The likely pathway for selective deposition is ethanol reduction of the copper oxides on the surface, and at the same time, ethoxy and hydroxyl formation on the silicon surface[125,126] and oxidation of the zirconium precursor. However, as indicated in our previous work, reaction byproducts also influence selectivity. The thickness of the ZrO_2 films on Si and Cu were measured via ellipsometry. The presence of Zr on these substrates was probed and analyzed through XPS and selectivity was quantified using the area of the Zr 3d peaks. Changes in selectivity with EtOH pretreatment times were attributed to reduction of the copper oxides and byproduct formation.

5.2 Methods and Materials

SALD of ZrO_2 was performed in a custom built hot-wall ALD reactor (patent #10214817) at 200°C [127] and 400 mTorr. The reactor design is described in detail elsewhere[127]. Substrates for deposition consisted of 2

cm x 2 cm pieces of p-type, highly doped, 1-5 Ω -cm <100> silicon and electroplated copper on silicon. The electroplated copper samples were composed of 10 nm of Ta and 100 nm of Cu deposited via physical vapor deposition and 500 nm of electroplated Cu on silicon. Prior to deposition the substrates were rinsed with deionized water (17.7 M Ω -cm) for 10 seconds and thoroughly dried with N₂ (99.99%, Praxair). The samples were then loaded into the reactor with the copper sample in front of the silicon sample with respect to flow through the reactor. Prior to deposition, the substrates were treated in-situ with continuous flow of ethanol vapor for 0 to 60 minutes at 200°C. After this pretreatment, 2 minutes of Ar purge were used for every 5 minutes of ethanol flow.

The zirconium precursor, tris(dimethylamino)cyclopentadienyl zirconium (ZyALD™), was kept in a stainless steel bubbler at 50°C and supplied with Ar (99.99% Ar, Praxair) as the carrier gas and the overall flow was adjusted to maintain a deposition pressure of 400 mTorr. Ethanol (200 proof, Decon Labs #2716) was used as the co-reactant and was kept in a glass wash bottle in an ice bath with N₂ (99.99%, Praxair) as the carrier gas with a back pressure of 5 psig. Ethanol was supplied through a 100 μ m aperture and the system pressure was ~750 mTorr with only ethanol flowing. An individual ALD cycle consisted of a zirconium precursor pulse of 2 seconds followed by 15 seconds of Ar purge, a 15 second ethanol pulse and 30 seconds of Ar purge.

The zirconia film thickness on silicon and copper was measured using spectral ellipsometry (Model M-44, J.A. Woollam Co.). X-ray photoelectron spectroscopy (Kratos AXIS-165, Kratos Analytical Ltd.) was performed with a monochromatic Al K α X-ray source, an accelerating voltage of 12 kV and an emission current of 10 mA. Survey scans were acquired with dwell times of 400 msec, a pass energy of 80 eV, 1 eV steps and 1 sweep. High-resolution scans were acquired with dwell times of 800 msec, a pass energy of 20 eV, 0.1 eV steps and 5 sweeps. X-ray photoelectron spectroscopy (XPS) spectra were aligned to have the carbon 1s peaks at 284.8 eV.

5.3 Results

To provide comparison to our previous research on SALD of ZrO₂ on electron beam evaporated copper, survey and high-resolution X-ray photoelectron spectra of electron beam evaporated and electroplated copper were collected. As there are significant differences between the copper deposition processes, large differences were expected in the deposited copper. For example, the XPS survey scans showed ~3 at.% less copper, ~9 at.% more carbon, and ~7 at.% less oxygen on the electroplated copper compared to the electron beam evaporated copper. The larger carbon content and lower copper content is most likely due to the additional processing steps and use of

organic additives in the plating process[128] while the lower oxygen content may likely be due to less carbonate (CO_3) as indicated by the spectral profile of the C1s region as explained more fully below.

High-resolution X-ray photoelectron spectra for the C1s, O1s, Cu LMM, and Cu 2p regions are shown in **Figure 47** and peak-fitting parameters from Biesinger[129] and Zhu et al.[130] were used for analysis. From the deconvolution of the C 1s region, electroplated copper has less CO_3 at ~289.3 eV, but more C-OH and C=O at 286.1 eV and 287.7 eV, respectively. Deconvolution of the O 1s region of these samples show mixtures of Cu_2O , CuO and $\text{Cu}(\text{OH})_2/\text{CuCO}_3$ and for these species more detailed analysis was done using the Cu LMM and Cu 2p regions. These regions show that the electroplated copper was ~20% Cu(0), ~62% Cu_2O , ~4% CuO, and ~15% $\text{Cu}(\text{OH})_2/\text{CuCO}_3$ and the electron beam evaporated copper was ~33% Cu(0), ~52% Cu_2O , ~3% CuO, and ~12% $\text{Cu}(\text{OH})_2/\text{CuCO}_3$. After examining the differences between the copper substrates, SALD of ZrO_2 was performed on electroplated copper.

Thickness of deposited ZrO_2 films measured via spectral ellipsometry versus number of ALD cycles is shown in **Figure 48a** for the silicon and electroplated Cu coated silicon substrates. All these samples were treated with 5 minutes of continuous EtOH flow prior to ALD. ZrO_2 thickness on silicon was found to increase linearly with the number of ALD cycles at a rate approximately 0.33 Å/cycle. ZrO_2 thickness on Cu for 100 or fewer cycles was measured to be zero and above 100 cycles, thickness increased at a rate of approximately 0.33 Å/cycle. These growth rates are similar to the growth rate of ALD on electron beam evaporated Cu (0.40 Å/cycle)[108] and less than half the rate when using the same precursor but with ozone as the oxygen source (0.87 Å/cycle)[131]. Based on the results of Figure 2, selective deposition was observed up to 100 ALD cycles with a 5-minute ethanol pretreatment. In addition, spectral ellipsometry modeling of ZrO_2 and copper oxides was performed. Although copper oxide is reported to form a binary layer with CuO as the top layer and Cu_2O as the bottom layer, in contact with metallic Cu,[122,132] best-fit results in all ALD samples were obtained using an ellipsometric model with only CuO. After a DI rinse and N_2 dry a CuO thickness of ~1 nm was measured. However, as our samples were loaded into the deposition reactor at 200°C and unloaded into ambient air, further oxidation by ambient exposure may be expected. The impact of ambient exposure of the Cu substrate during loading and unloading was examined by measuring the CuO thickness using spectral ellipsometry before and after loading Cu substrates into the reactor. With loading and unloading Cu substrates without cooling the reactor, a CuO thickness of ~5 nm was measured. In

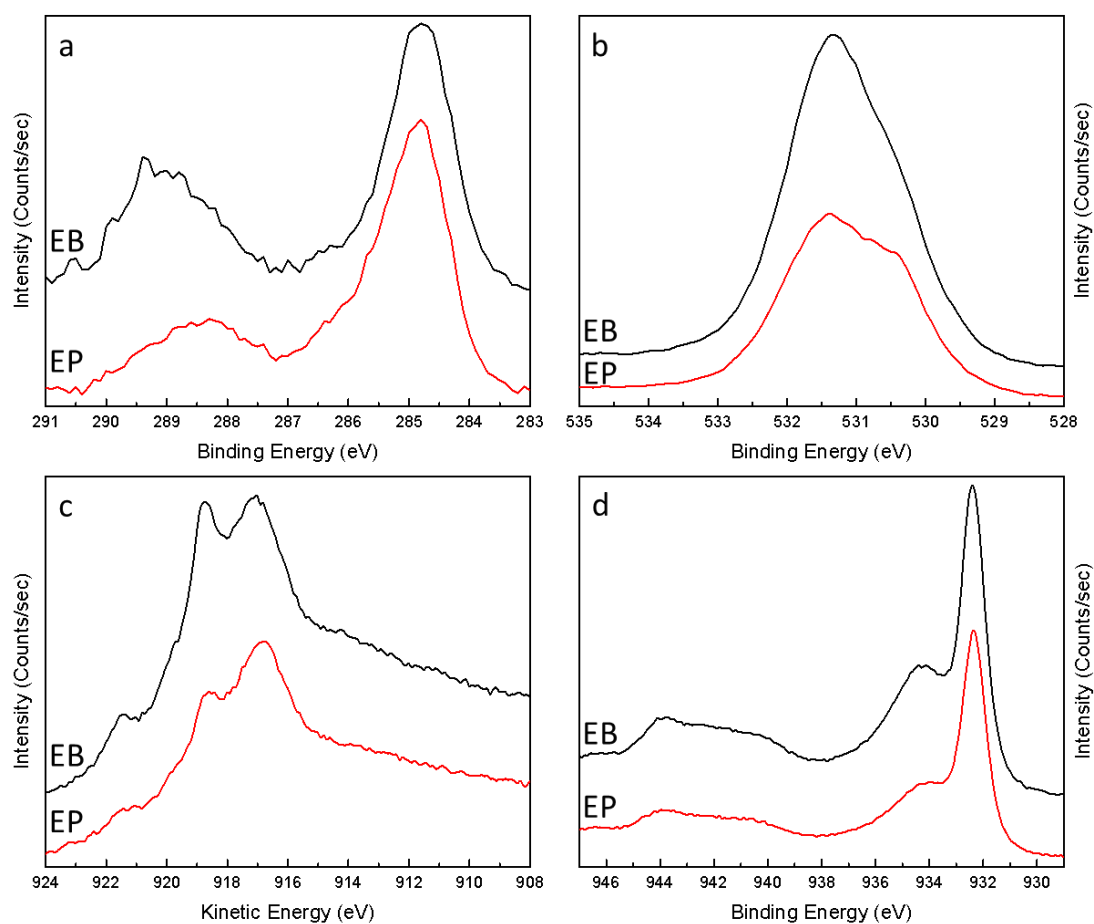


Figure 47. High-resolution X-ray photoelectron spectra of the electron beam evaporated (EB) and electroplated copper (EP) substrates after a DI H₂O rinse and N₂ dry. (a) C 1s. (b) O 1s. (c) Cu LMM. (d) Cu 2p.

contrast, ~2 nm of CuO was measured after loading the Cu substrate into the reactor, cooling the reactor to ~66 °C at 200 mTorr with 30 sccm of Ar flow, and then unloading it.

Thus, we estimate ~4 nm additional Cu forms upon unloading samples from the hot reactor in cases where there is no ZrO₂ deposition. Since the oxidation due to unloading occurs after deposition, this should not significantly affect the SALD process, and so the reactor was not cooled prior to unloading other samples. After pretreatment and ALD of zirconia, the CuO thickness measured decreased with both 5-minute EtOH pretreatment and increasing ALD cycles. This decrease in CuO thickness is attributed to reduction of the CuO from the EtOH pretreatment and cyclic EtOH exposure during the ALD process. As variation in the loading and unloading time might affect the CuO thickness, the work presents only preliminary general trends in the CuO thickness with the processing conditions used.

The XPS spectra for Si and electroplated Cu coated Si substrates with different number of ALD cycles and a 5-minute EtOH pretreatment are also shown in **Figure 48**. From the XPS survey scans of the electroplated Cu-coated Si substrate shown in **Figure 48b**, Cu 2p: 933 eV and 953 eV, 3p: 76 eV, 3s: 123 eV, O 1s: 531 eV, and C 1s: 285 eV were detected. The Cu peaks are from the electroplated Cu substrate and thin Cu oxide layer. Oxygen is likely from the copper oxides and carbonate present while carbon is from adventitious carbon and carbonate. For 0 to 70 ALD cycles, no Zr was detected on the electroplated Cu, but was detected on Si, indicating selective deposition as previously observed in our work for electron beam evaporated Cu[108]. The similarity of selectivity observed here was unexpected for two reasons. One, there were additional impurities on the electroplated Cu due to the additional processing steps and additives used in the electroplating process. But apparently these differences identified through XPS do not significantly affect the SALD process. Secondly, gaseous diffusion of byproducts from the silicon to the copper substrate which is believed to play a role in selectivity[108] on electron beam evaporated Cu is highly unlikely in the present studies.

Further analysis of XPS shows Zr was detected on the Cu samples with 100 or more ALD cycles showing less selectivity than indicated by spectral ellipsometry which showed no evidence of a ZrO₂ layer at 100 cycles. This difference is believed to be due to a very thin or non-uniform ZrO₂ film on the Cu samples after 100 ALD cycles which can be detected by XPS but not ellipsometry. The Zr peaks observed by XPS after 100 cycles were 3d: 183 eV and 185 eV and 3p: 333 eV and 347 eV. After 200 cycles, Zr 3d and 3p peak intensities increased and

Zr 3s: 432 eV and 4p: 31 eV peaks become visible, indicating a thicker ZrO₂ film on copper. Overall, Zr peak intensities were found to increase with the number of ALD cycles while Cu peak intensities decreased as indicative of increasing ZrO₂ thickness.

Figure 48c shows the XPS survey scans on Si with different ALD cycles after a 5-minute EtOH pretreatment. The peaks detected from the survey of the Si substrate with 0 ALD cycles are Si 2p: 99 eV, 2s: 150 eV, C 1s: 285 eV and O 1s: 532 eV. Si peaks are attributed to both the substrate and a ~1.5 nm native silicon oxide. Oxygen peaks are also likely from the native silicon oxide, while the carbon peak is attributed to adventitious carbon. After 50 cycles of ZrO₂ ALD, Zr peaks 4p: 31 eV, 3d: 183, 185 eV, 3p: 333, 347 eV and 3s:432 eV are visible. The intensities of these peaks increase with the number of ALD cycles, while the Si peaks decrease as indicative of increasing ZrO₂ thickness. Zr peak intensities were greater on Si than on Cu after 100 cycles indicating lower selectivity above 70 ALD cycles.

Zirconia ALD on silicon and Cu substrates was further studied using different EtOH pretreatment times and 100 ALD cycles. **Figure 49** shows the XPS spectra for 100 ALD cycles of ZrO₂ deposited on Si and Cu substrates after EtOH pretreatment times of 0 to 60 minutes. The characteristic Zr 3d peaks from these XPS spectra were used to determine the effect of pretreatment time on selectivity. The area of the Zr 3d peaks on silicon was divided by the area of the Zr 3d peaks on Cu. ZrO₂ ALD was performed on these samples at the same time and XPS was performed on these samples in the same run. This ratio versus pretreatment is shown in **Figure 50**. From this figure, selectivity was found to increase to a maximum with a ~30-minute EtOH pretreatment, while it actually decreased with longer pretreatment times. The maximum selectivity reached was ~6X more ZrO₂ deposited on the Si substrate compared to the Cu substrate. The lowest selectivity was found using no pretreatment where ~20% more ZrO₂ was deposited on Cu than on Si. This is likely due to an increase in the active sites on Si with a 5-minute EtOH pretreatment versus no pretreatment. Adsorption and redox reaction of EtOH on the Si surface leads to formation of hydroxyl and ethoxy groups[125,126] which increases the number of active sites resulting in increased growth of ALD ZrO₂ on Si with the EtOH pretreatment. However, the EtOH adsorption likely saturates within ~5 minutes as additional exposure appeared to have little effect on the ZrO₂ growth. The increase in selectivity with pretreatment time is attributed to reduction of copper oxides and was consistent with our ellipsometry measurements, which showed decreasing CuO thickness with EtOH pretreatment time. The decrease in selectivity

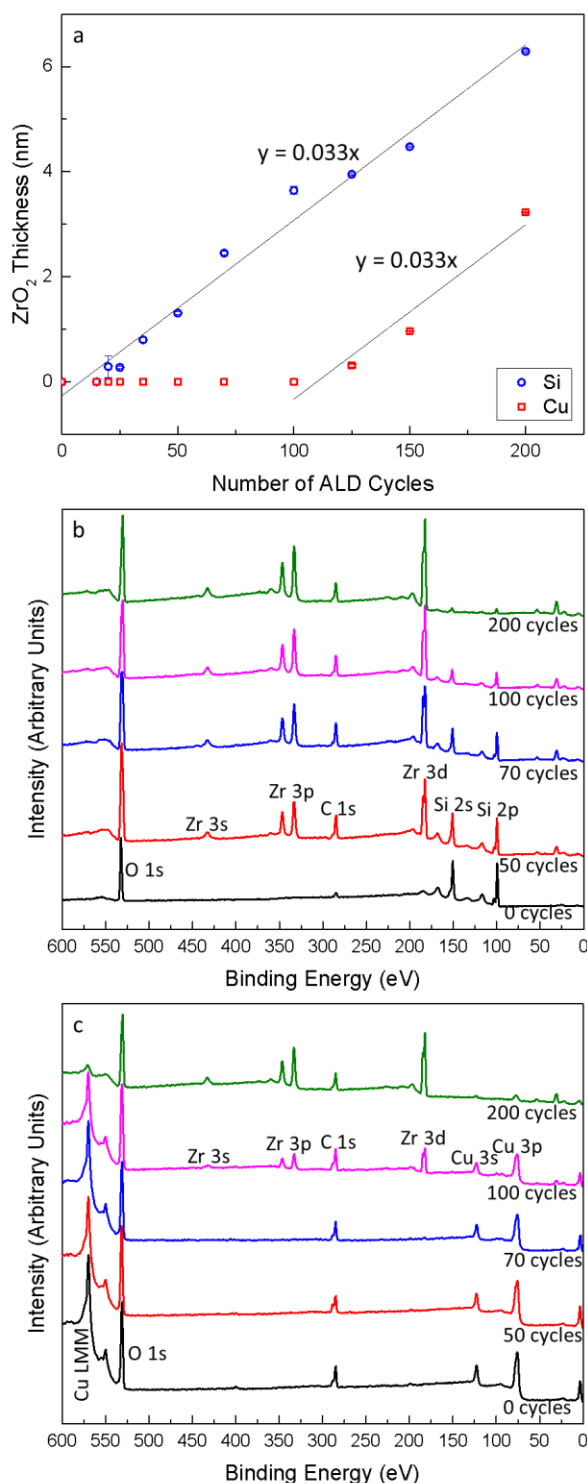


Figure 48. (a) ZrO₂ film thickness on silicon and electroplated copper coated silicon substrates versus number of ALD cycles, where film thickness was measured via spectral ellipsometry and error bars indicate the uniformity of the film across the samples. Deposition consisted of a 5-minute ethanol pretreatment and 2-minute Ar purge followed by 2 s ZyALD:15 s Ar and 15 s ethanol:30 s Ar pulses at 200°C. (b-c) X-ray photoelectron spectra of samples prepared with a 5-minute ethanol pretreatment and 0 to 200 ALD cycles of ZrO₂. (b) Spectra for electroplated copper coated silicon substrates. (c) Spectra for silicon substrates.

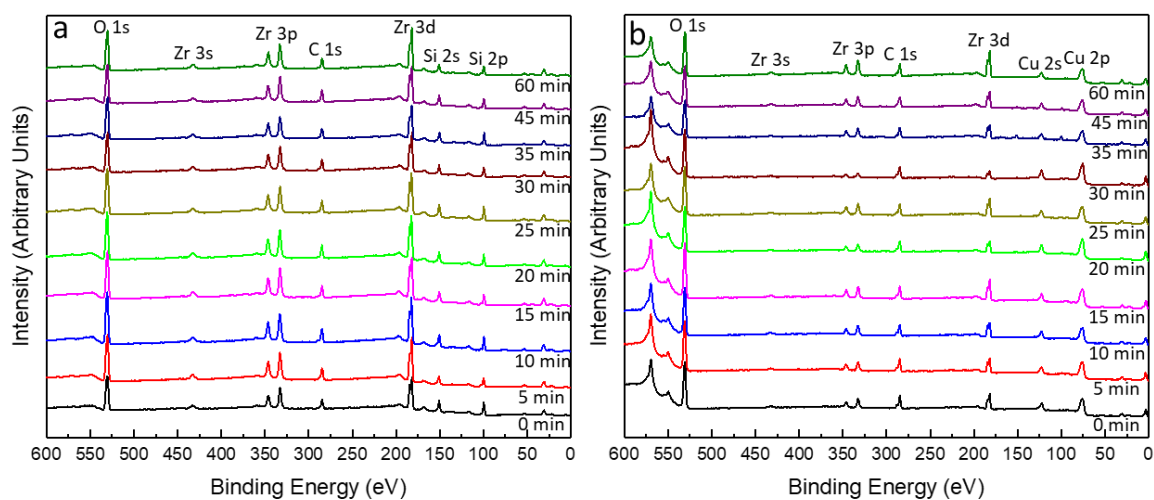


Figure 49. X-ray photoelectron spectra of samples prepared with different ethanol pretreatment times and 100 ALD cycles of ZrO_2 . (a) Spectra for silicon substrates. (b) Spectra for electroplated copper coated silicon substrates.

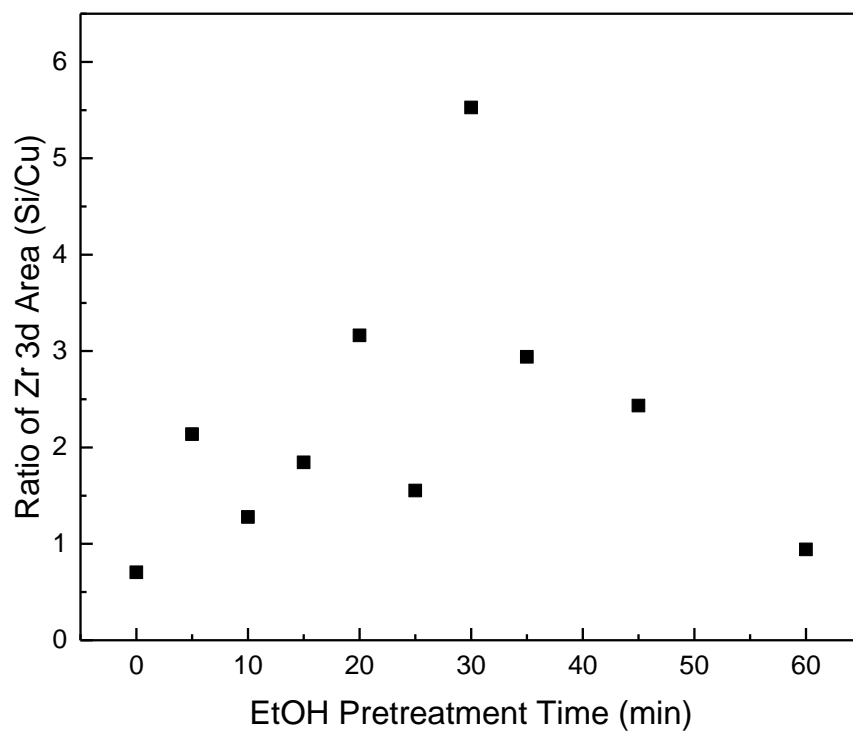


Figure 50. Ratio of Zr 3d Area (Si/Cu) vs. ethanol pretreatment time.

with pretreatment times beyond ~30 minutes is attributed to byproduct formation on the copper surface; this is corroborated by thermodynamic analyses of these electronic material systems.[133,134]

To investigate this byproduct formation on the electroplated copper surface, XPS spectra were acquired after 60 minutes of EtOH pretreatment and are shown in **Figure 51**. This pretreatment was performed at 200°C. Afterwards, the reactor was cooled to 30°C and the sample was transferred to the XPS chamber within approximately 30 minutes of ambient air exposure from the transfer. The XPS spectra after this EtOH treatment are quite similar to the spectra for copper after EtOH treatment by Chabal et al.[124] From the carbon spectra, less C-O-C/C-O-H (283.2 eV) and CO₃ (289.3 eV), but similar amounts C-C (284.8 eV) and C=O (287.9 eV) are observed. Additionally, a significant decrease in the oxygen peak was observed and from peak-fitting the O 1s, Cu 2p and Cu LMM regions, the oxide is predominately Cu₂O with small amounts of CuO and Cu(OH)₂. These results indicate that the heating and ethanol treatment reduces the copper oxides, carbonates and C-O-C/C-O-H bonds. However, identification of byproducts is difficult due to volatility of some plausible species like acetaldehyde and CO₂ as well as ambient exposure during transfer to the XPS system. Acetaldehyde and ethyl species may be present based on the C-C and C=O bonds observed by XPS. Both acetaldehyde and ethyl species have been reported to form from EtOH reduction of Cu.[135,136] Comprehensive thermodynamic analyses within the framework introduced for the selective growth of electronic materials[133,134] have also corroborated these results. Formation of byproducts such as H₂O and CO₂ are also thermodynamically favorable and have been reported to form from the reaction of EtOH and oxides on Cu at 200°C[122,135] Furthermore, H₂O and CO₂ form carbonates on the Cu surface[136]. This is also in agreement with the work of Pena et al. who found carbonates can deposit on the copper surface during EtOH reduction, if byproducts are not removed from the reactor.[124] In the present studies, there is continuous gas flow purging of the reactor during EtOH pretreatment and so less carbonates likely form. This is consistent with our observed decrease in carbonates after ethanol treatment. Nonetheless, byproducts which adhere to the copper surface can still serve as nucleation sites for ZrO₂ ALD since there is a continuous decrease in selectivity with pretreatment times longer than 30 minutes; these byproducts were found to increase with ethanol pretreatment time.[133,134]

Similar to our work on electron beam evaporated Cu, reduction of Cu oxides on electroplated Cu can be explained as adsorption of EtOH on the Cu oxides and oxidation of the EtOH. Partial oxidation of EtOH forms

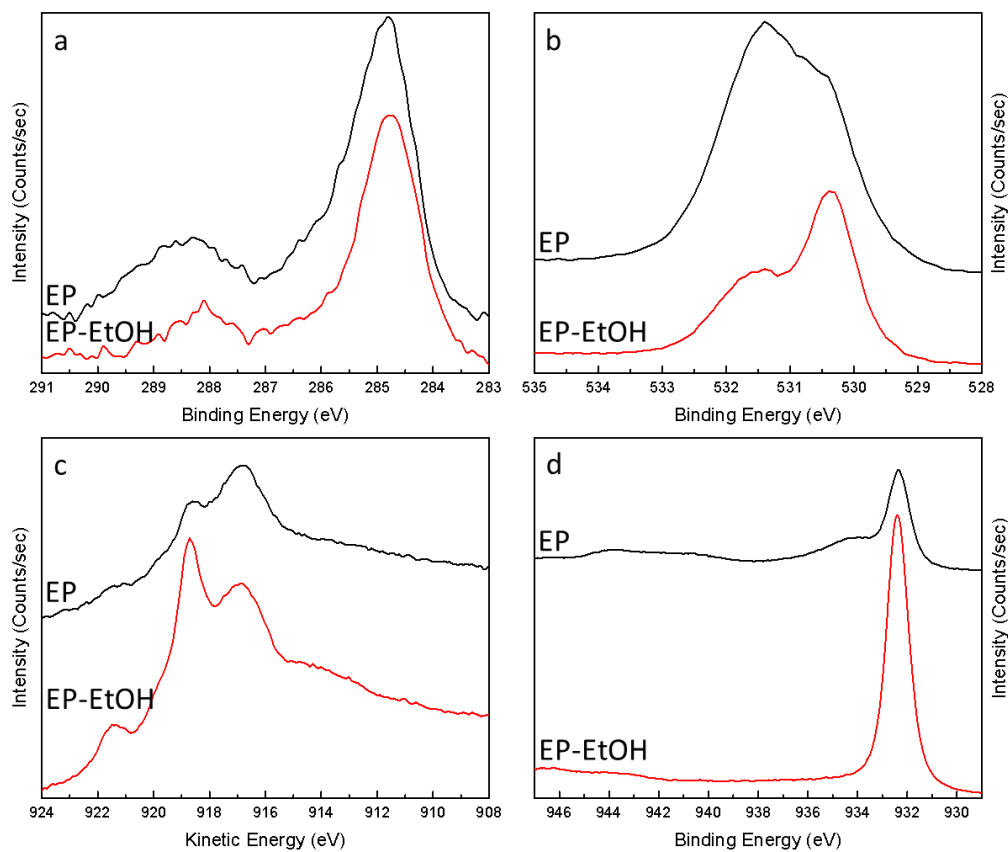


Figure 51. X-ray photoelectron spectra of electroplated copper after DI water rinse (EP) and after 60 minutes of in-situ ethanol treatment at 200°C (EP-EtOH). (a) C 1s. (b) O 1s. (c) Cu LMM. (d) Cu 2p.

acetaldehyde and H_2O , whereas complete oxidation of EtOH forms CO_2 and H_2O [135]. As selectivity varied for different pretreatment times, EtOH exposure to the substrates prior to deposition clearly affected the nucleation time for ALD of ZrO_2 . Partial reduction of Cu oxides prior to ALD reduces the number of active sites available, while excessive pretreatment causes accumulation of some byproducts on the Cu surface which increase the number of active sites; this is also supported from thermodynamic analyses.[133,134] Loss of selectivity with ALD cycles greater than 70 cycles is likely due to the increased time available for relatively slow, yet unknown nucleation mechanism(s) for the ZrO_2 on the Cu substrate. Based on these studies, SALD of ZrO_2 on electroplated Cu may be significantly enhanced further, well beyond 70 cycles, via optimization of the ALD reactor, precursor delivery, and alternate selection of ALD precursor and oxidizer.

Thermodynamic analyses with different alcohols indicate that alcohols with shorter hydrocarbon chain are predicted to perform better in the Cu reduction during zirconia area-selective ALD, assuming everything else is the same,[133,134] in agreement with related data reported in the literature.[126] Yet, the highest value of oxygen/carbon ratio in the alcohol with the shortest hydrocarbon chain, i.e., methanol, can result in insufficient copper oxide reduction during zirconia SALD. Overall, important factors in an SALD system involve the relative amounts of carbon and oxygen in the ALD reactor (including oxygen from system base pressure elements and feed impurities) as well as the deposition conditions.

5.4 Conclusions

Thin ZrO_2 films were selectively deposited on Si and not on electroplated Cu using tris(dimethylamino)cyclopentadienyl zirconium and ethanol at 200 °C. Deposition was selective between Si and electroplated Cu substrates for at least 70 ALD cycles. Through optimization of the ethanol pretreatment time, the selectivity of the deposition for 100 ALD cycles was increased to have approximately 6 times more ZrO_2 deposited on the silicon substrate than on the copper substrate. Increase in selectivity with ethanol pretreatment time up to ~30 minutes was attributed to increasing reduction of the copper oxides coupled with minimized byproduct formation on the substrate. The decrease in selectivity after ~30 minutes of pretreatment is attributed to byproduct formation and deposition on the Cu surface. As decreasing the copper oxides on the electroplated copper substrate improves selectivity, it is necessary to minimize the oxides and byproduct formation on the same Cu surface. Minimizing the oxides and byproducts could be accomplished for example, with EtOH pulses followed by inert gas

purges introduced in a cyclic manner.[124,133] In addition to introducing the EtOH pretreatment in a cyclic manner, further improvement in selectivity is possible with careful optimization of the ALD recipe and reactor design.

CHAPTER 6

Selective Atomic Layer Deposition of Zirconium Oxide on Chemically Mechanically Polished Copper

6.1 Introduction

Selective atomic layer deposition (SALD) has the potential to reduce the number of processing steps involved in device fabrication, reducing the overall cost and complexity of fabrication. SALD can be achieved through different methods which can be largely classified into area-activation SALD or area-deactivation SALD. These processes are similar to the conventional atomic layer deposition (ALD) process, but often with a few additional steps. For area-activation SALD, seed layers of material are deposited where ALD growth is desired while little or no growth occurs without the seed layer. Area-deactivation SALD most commonly relies on self-assembled monolayers (SAMs) which are patterned and prevent growth where they are deposited. For area-activation, the materials which can be deposited and used for the non-growth areas are often limited. In area-deactivation SALD, the deactivating materials typically must be removed after the deposition process. An improved approach is to use a material already present in the device fabrication to prevent deposition, eliminating the need for removal.

In our previous work we demonstrated SALD of zirconia (ZrO_2) on electron beam evaporated[108] and electroplated copper. Electroplated copper has largely become the material of choice for interconnects in integrated circuits.[137] The change from aluminum to copper has been driven by integrated circuit scaling and performance needs. Copper has lower resistivity, higher thermal conductivity, lower activation energy and is more resistant to electromigration failures[138,139]. Together these allow for smaller dimensions and higher current densities while providing higher performance. Other than being used in complimentary metal-oxide-semiconductor (CMOS) technology, electroplated copper can be used as metal coatings on optical fibers for making high temperature optical sensors[140], and to create contacts in silicon solar cells.[141]

Despite the advantages of copper, it is quickly oxidizing in air at low temperatures and does not form a self-protective oxide layer to prevent further oxidation. Furthermore, copper is more difficult to pattern using conventional etching techniques.[139] To eliminate the need to etch copper, techniques such as the damascene

process are used which also reduce the number of processing steps compared to fabrication of aluminum interconnects.[139,142] In the damascene process, a dielectric is deposited and etched, then a barrier film and copper seed layer are deposited, and last copper is electroplated and chemically mechanically polished (CMP).[142] The electroplating process fills in the trenches and VIAs etched in the dielectric and the copper is often over-plated to ensure these areas are filled. CMP is then used to remove the excess copper and planarize the surface. However, both the electroplating and CMP processes can introduce impurities into or onto the copper, affecting the SALD process.

In the electroplating process, the copper seed layer serves as the cathode and the flow of electrical current through a copper electrolyte causes copper ions to deposit onto this seed layer. In addition to the electrolyte, there are a number of additives in the electroplating process which control the deposition rate and location in order to establish void-free filling of trenches and VIAs. [143] These additives are primarily suppressors/brightening agents, accelerators, and levelers.[143] In copper-sulfate based plating, suppressors such as polyethylene glycol or polypropylene glycol are used and combine with chloride ions to reduce the deposition rate.[143] Accelerators such as bis(sodiumsulfopropyl) disulfide are used to form electroactive species which increase deposition and levelers such as thiourea or benzotriazole are used control surface morphology and even out current distribution to produce a uniform plated surface.[143] These and other additives can introduce impurities into the copper film such as hydroxides, complex metal ions and hydrogen gas bubbles.[117,137] However with careful control of the plating process, these impurities can be avoided, and in our work on electroplated copper, no impurities were detected by X-ray photoelectron spectroscopy (XPS) on commercially plated copper substrates. Therefore, little difference in selectivity was found between electron beam evaporated and electroplated copper.

The final part of the damascene technique is the CMP process. In the CMP process, a slurry of chemicals and abrasives in conjunction with an abrasive pad are used to chemically and mechanically remove material to create a uniform surface. The chemical slurry is generally composed of three main components: abrasive particles, a chemical for dissolving material removed from the surface, and a chemical for limiting the dissolution of the polished material. For polishing of copper, silica is commonly used as an abrasive[144] while ferricyanide and benzotriazole (BTA) are commonly used for the dissolution chemical, and dissolution inhibitor, respectively[138]. In addition to ferricyanide based slurries, numerous other chemicals have been investigated for use in CMP

slurries[145]; however, the chemicals most likely to remain on the surface after the CMP process are the dissolution inhibitors, such as BTA, which form complexes with the copper or copper oxide[146,147]. As the CMP process is the last part of the damascene technique, selectivity after this process is essential in order to use the copper in the SALD process. Yet, the effect of impurities from the CMP process on selectivity have not been studied.

Here we report on the chemical species and oxides observed via XPS of the CMP copper substrate, their effect on the SALD of ZrO_2 , further characterization of the SALD process, and techniques for increasing selectivity. The thickness of the deposited ZrO_2 films on silicon and copper were measured via spectral ellipsometry. Differences in chemical species, oxides and selectivity were analyzed via XPS, where ratios of the atomic percentage of Zr were used to quantify selectivity.

6.2 Methods and Materials

SALD of zirconia was performed using a custom built hot-wall reactor which is described in detail elsewhere.[127] Deposition was performed at 200°C with a deposition pressure of approximately 400 mTorr. Tris(dimethylamino)cyclopentadienyl zirconium (ZyALD^{TM}) was used as the zirconium precursor and was kept in a stainless steel bubbler at 50°C . Zr precursor was supplied using Ar (99.999% Ar, Praxair) as the carrier gas. Ethanol (200 proof, Decon Labs #2716) was used as the co-reactant and supplied with N_2 (99.999%, Praxair) as the carrier gas with a back pressure of 5 psig. During deposition, ethanol was kept in a glass wash bottle in an ice bath. Flow of ethanol was restricted using a 100 μm aperture and produced a system pressure of ~ 1500 mTorr with only ethanol flowing. Each ALD cycle consisted of a zirconium precursor pulse of 7 seconds, 20 seconds of Ar purge, 15 seconds of ethanol pulse, and 55 seconds of Ar purge.

Substrates for deposition consisted of 2 cm x 2 cm pieces of silicon, electroplated copper on silicon and electroplated copper on silicon that had been chemically mechanically polished. Silicon substrates were <100>, p-type, highly doped, with resistivities of 1-5 $\Omega\text{-cm}$ (WaferPro, C04007). Electroplated copper substrates consisted of 500 nm of electroplated Cu on top of 100 nm of Cu and 10 nm of Ta deposited via physical vapor deposition on silicon. Electroplated copper substrates that had been through the CMP process were used directly after the polishing process and after treatments used to try to remove benzotriazole, the dissolution/corrosion inhibitor used during the polishing process. The first treatment was in-situ ethanol treatment at 200°C and ~ 1500 mTorr for 60 minutes. The

second treatment was heating to 335°C in a tube furnace (Lindberg, Model 54032) at 640 mTorr for 60 min with N₂ (99.99%, Praxair) flow through the furnace.

Before treatment of the substrates or deposition for non-treated samples, substrates were rinsed with deionized water (17.7 MΩ-cm) and dried with N₂ (99.99%, Praxair). Following treatment or the pre-deposition rinse, the substrates were loaded into a quartz boat and inserted into the reactor with the copper sample in front of the silicon sample with respect to flow through the reactor. Additionally, a dummy sample with the same dimensions as the Cu and Si samples was placed in front of these samples with respect to flow. Substrates were allowed ~10 minutes to reach the deposition temperature of 200°C before being treated in-situ with ethanol vapor. This in-situ treatment was performed before deposition with ethanol vapor introduced as a continuous flow for 5 minutes.

Spectral ellipsometry was used to measure the zirconia film thickness on silicon and copper substrates (Model M-44, J.A. Woollam Co.). X-ray photoelectron spectroscopy (Kratos AXIS-165, Kratos Analytical Ltd.) was performed with a monochromatic Al K_α X-ray source. Survey scans were performed with a dwell time of 400 msec, an emission current of 10 mA, an accelerating voltage of 12 kV, a pass energy of 80 eV and 1 sweep. High-resolution scans were performed with the same emission current and accelerating voltage, a dwell time of 800 msec, a pass energy of 20 eV and 2-5 sweeps. X-ray photoelectron spectroscopy (XPS) spectra were aligned to have the carbon 1s peaks at 284.8 eV. XPS peak fitting was performed using CasaXPS with fitting parameters for the Cu L₃M_{4,5}M_{4,5}, Cu 2p, C 1s, and O 1s regions from the work of Biesinger[129] and Zhu[130] and a Shirley background correction.

6.3 Results

The SALD window was characterized by measuring the thickness of ZrO₂ deposited on silicon substrates via spectral ellipsometry after 70 ALD cycles with different precursor and oxidizer pulse times. The spectral ellipsometry measurements of the ZrO₂ thickness were divided by the number of ALD cycles to determine the growth per cycle and the growth rates from these saturation studies are shown in **Figure 52**. ZrO₂ growth appears to plateau for precursor pulse times of 6 seconds or longer when a 15 second oxidizer pulse is used. While a plateau in ZrO₂ growth is observed for oxidizer pulse times of 10 seconds or longer when precursor pulse times of 7 seconds are used. Therefore, precursor pulse times of 7 seconds and oxidizer pulse times of 15 seconds were used for the ALD process. In both of these saturation studies, the second slot with respect to flow through the reactor was

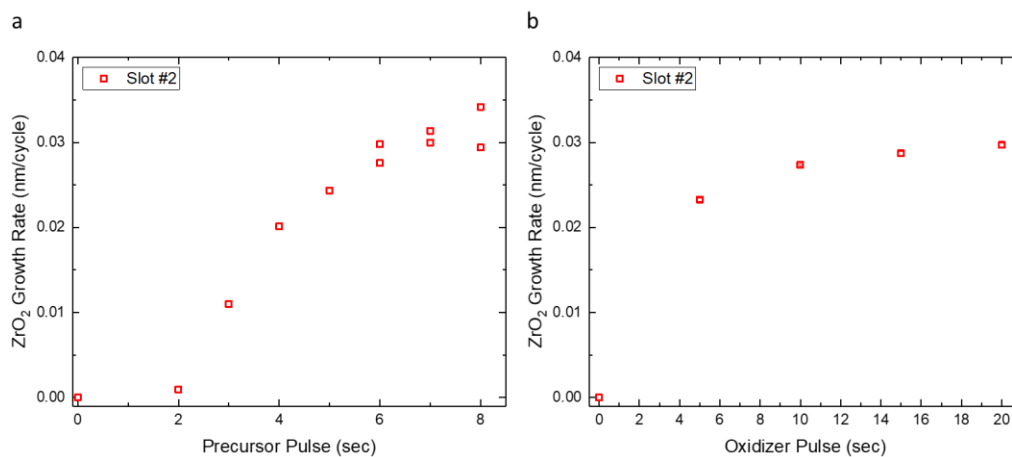


Figure 52. Spectral ellipsometry measurements of ZrO₂ thickness and growth rate on silicon substrates from 70 ALD cycles. (a) ZrO₂ growth rate versus precursor pulse times when an oxidizer pulse time of 15 seconds was used. (b) ZrO₂ growth rate versus oxidizer pulse times when a precursor pulse time of 7 seconds was used.

measured as flow stagnation and less uniform growth was measured for substrates in the first slot. Other than these saturation studies, the first slot was always occupied by a dummy sample with the same dimensions as the other substrates. The influence of precursor and oxidizer purge times were not investigated; however, 20 seconds of purge time for the zirconium precursor and 55 seconds of purge time for the oxidizer appeared sufficient as the deposition pressure had returned to 400 mTorr after purging.

XPS surveys of electroplated (EP) and chemically mechanically polished (CMP) copper substrates after a deionized water rinse and N₂ dry are shown in **Figure 53**. The peaks observed, and their locations are given in **Table VII**. Little difference was observed between the peak locations from the different Cu substrates. However, a

Substrate	Cu 2p _{3/2} (eV)	Cu 3p (eV)	Cu 3s (eV)	C 1s (eV)	O 1s (eV)	N 1s (eV)
EP	952.5, 932.5	76	123	284.8	531	-
CMP	952.5, 932.5	76	123	284.8	531	399

TABLE VII. PEAKS OBSERVED FROM X-RAY PHOTOELECTRON SPECTRA OF THE COPPER SUBSTRATES SHOWN IN FIGURE 1. SPECTRA WERE ALIGNED TO HAVE THE CARBON 1S PEAK AT 284.8 EV.

nitrogen 1s peak: ~399 eV was observed for the chemically mechanically polished (CMP) sample. The nitrogen peak is likely due to the heterocyclic amine, benzotriazole (BTA)[148]. BTA is introduced during the polishing process for corrosion inhibition, surface passivation and as a dissolution inhibitor.[148] Atomic percentages of Cu, C, O, and N from the XPS surveys are shown in **Table VIII**. The larger carbon content in the CMP sample may be

Substrate	Cu (At. %)	C (At. %)	O (At. %)	N (At. %)
EP	15.7	33.1	51.2	0.0
CMP	17.4	38.4	41.6	2.6

TABLE VIII. ATOMIC PERCENTAGES CALCULATED FROM THE SURVEYS. EP: ELECTROPLATED CU SUBSTRATE. CMP: CHEMICALLY MECHANICALLY POLISHED CU SUBSTRATE.

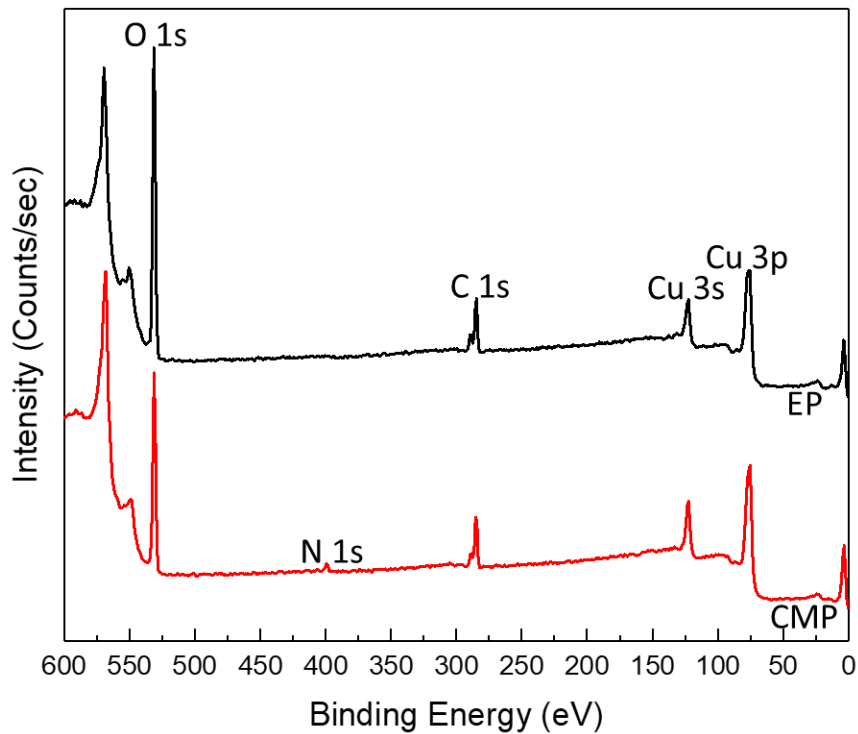


Figure 53. X-ray photoelectron spectra of the copper substrates. EP: Spectra for the electroplated Cu substrate. CMP: spectra for the chemically mechanically polished Cu substrate. Spectra were aligned to have the carbon 1s peak at 284.8 eV and all samples were rinsed with DI water and dried with N₂ prior to XPS.

from additives in the CMP process, the BTA coating, or from variation in handling prior to XPS. The larger copper and lower oxygen content in the CMP sample are likely due to the corrosion inhibition properties of the BTA coating which reduce oxidation in the ambient air, resulting in a more metallic copper surface.

High resolutions scans of the C 1s region are shown in **Figure 54a**. The adventitious carbon peak is used for charge correction at a binding energy of 284.8 eV. Deconvolution of the carbon peaks show a mix of adventitious carbon (C-C at 284.8 eV, C-OH at 286.3 eV, C=O at 287.7 eV, and C-O-C at 288.6 eV)[129], graphitic carbon (C=C at 284.2 eV)[149] and carbonate (CO_3 at 289.3 eV)[130]. Graphitic carbon may be from carbon contamination[149] or the BTA coating while carbonate has been reported to form on copper after exposure to CO_2 and H_2O . [124] Despite the BTA coating on the CMP sample, the largest difference in the C 1s region was the larger amount of carbonate on the EP sample (~14% vs. 7% of the C 1s peak area).

A high-resolution scan of the O 1s region from the copper substrates is shown in **Figure 54b**. Both substrates show a mix of Cu_2O (lattice at 530.3 eV, defective at 531.4 eV), CuO (lattice at 529.5 eV, defective at 531.2 eV) and $\text{Cu}(\text{OH})_2/\text{CuCO}_3$ at 531.4 eV.[129] However less $\text{Cu}(\text{OH})_2/\text{CuCO}_3$ (~50% vs. 56% of the O 1s peak area) and more Cu_2O (~49% vs. 40% of the O 1s peak area) are observed on the CMP substrate compared to the EP substrate. Less carbonate is consistent with the C 1s region and less carbonate/hydroxide may be expected due to the hydrophobicity of the Cu-BTA surface film.[150]

High resolution scans of the Cu 2p and Cu $\text{L}_{3\text{M}_{4.5}\text{M}_{4.5}}$ regions are shown in **Figure 54c** and **Figure 54d**, respectively. As differentiation of the Cu species using the Cu 2p region is difficult when both Cu(II) and Cu(I) are present, the Cu 2p region was only used to find the approximate amounts of Cu(II) and Cu(0) + Cu(I). The amount of Cu(II) was found using the area of the satellite between ~937 and 945 eV and the amount of Cu(0) + Cu(I) was found using the area of the Cu $2\text{p}_{3/2}$ peak. Further differentiation of the Cu species was done using the Cu $\text{L}_{3\text{M}_{4.5}\text{M}_{4.5}}$ region. Deconvolution and peak fitting of the Cu $\text{L}_{3\text{M}_{4.5}\text{M}_{4.5}}$ region is shown in **Figure 55** where Cu(0), Cu_2O , CuO, and $\text{Cu}(\text{OH})_2/\text{CuCO}_3$ were included in the peak fitting and their contributions to the Cu Cu $\text{L}_{3\text{M}_{4.5}\text{M}_{4.5}}$ region are shown in **Table IX**. Similar to the O 1s and C 1s regions, a smaller amount of hydroxide/carbonate and oxide was observed on the CMP Cu substrate. The smaller amount of Cu_2O and larger amount of CuO relative to the Cu LMM region on the CMP Cu substrate are likely due to a thinner oxide layer due to the BTA coating limiting oxidation. The amounts of Cu(0) + Cu(I) and Cu(II) from the Cu $\text{L}_{3\text{M}_{4.5}\text{M}_{4.5}}$ region are in agreement with the areas from the

Substrate	Cu ₂ O (%)	Cu(0) (%)	CuO (%)	Cu(OH) ₂ (%)
EP	62	19	4	15
CMP	34	40	17	9

TABLE IX. CONTRIBUTIONS TO THE CU L₃M_{4.5}M_{4.5} PEAKS FROM CU₂O, CU(0), CUO, AND CU(OH)₂ CALCULATED FROM FITTING THE PEAKS SHOWN IN FIGURE 54.

Cu 2p region. However, it is important to note that this quantification uses peak fitting parameters from standards composed of only one chemical state. Therefore, variation in these values due to mixtures of the chemical states may reduce the accuracy of the quantification.

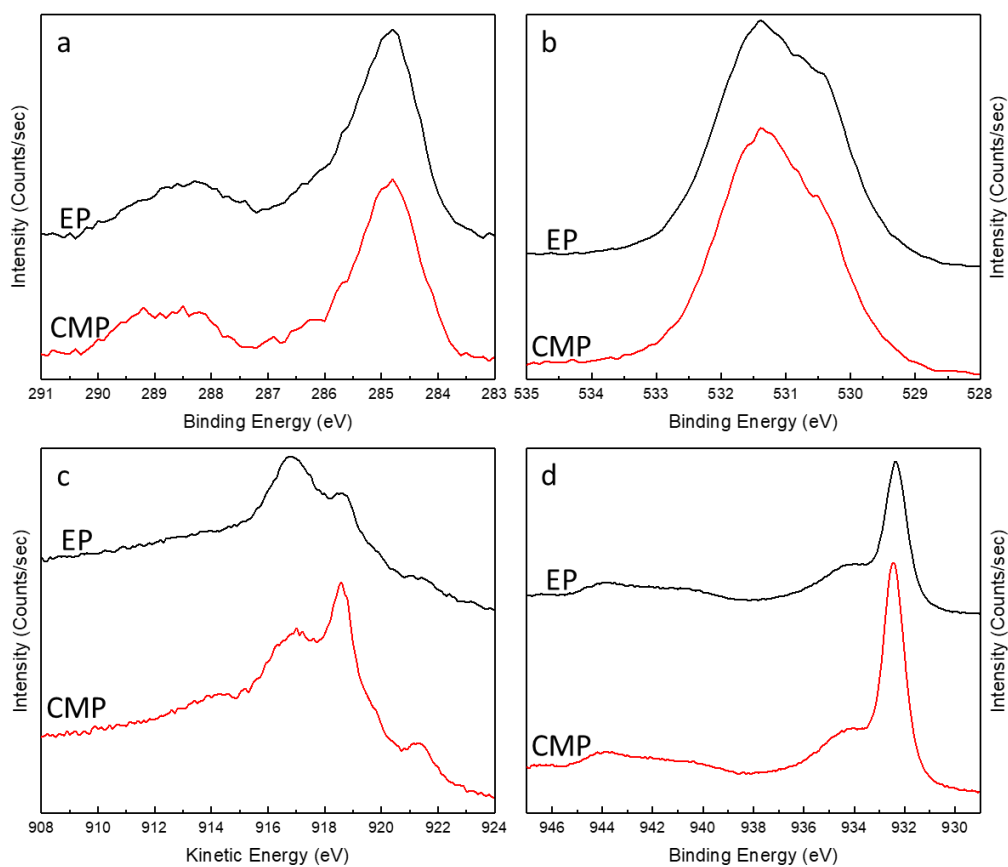


Figure 54. X-ray photoelectron spectra from electroplated (EP) and chemically mechanically polished (CMP) Cu substrates. (a) C 1s. (b) O 1s. (c) Cu LMM. (d) Cu 2p.

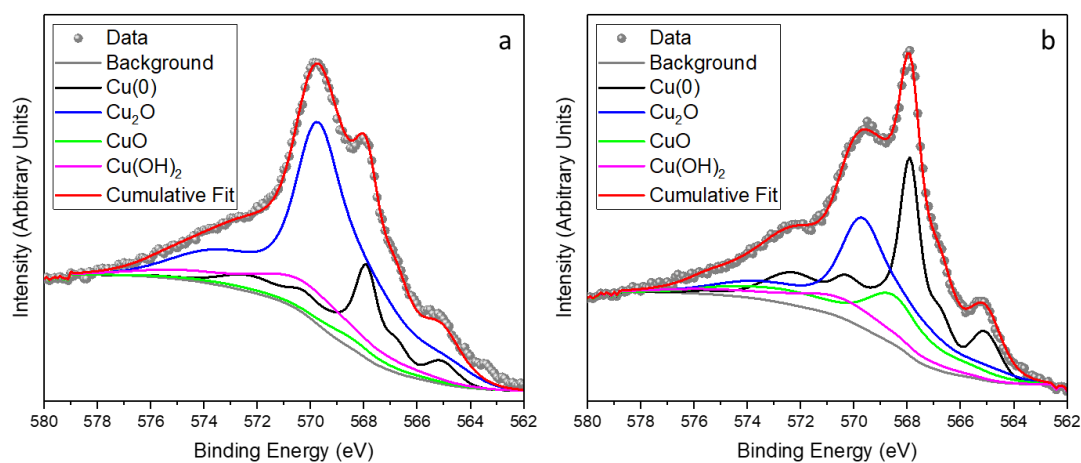


Figure 55. High-resolution X-ray photoelectron spectra of the copper $\text{Cu L}_{3.5}\text{M}_{4.5}\text{M}_{4.5}$ region with peak fitting. (a) Spectra for the electroplated Cu substrate. (b) Spectra for the chemically mechanically polished Cu substrate. Spectra were aligned to have the carbon 1s peak at 284.8 eV and all samples were rinsed with DI water and dried with N_2 prior to XPS.

After examining the chemical species present on the CMP copper substrates, 50 and 70 ALD cycles of ZrO_2 were deposited onto these substrates and silicon reference samples after 5-minute EtOH treatments at 200°C . XPS spectra for these samples are shown in **Figure 56**. Zr 3d and 3p peaks are visible on the CMP copper substrates after 50 ALD cycles and Zr 3s, 3p and 3d peaks with higher intensity can be seen after 70 ALD cycles. Whereas Zr 4s, 3d, 3p and 3s peaks are visible on the silicon substrates after 50 and 70 ALD cycles of ZrO_2 . Comparing the peaks and peak intensities on the Si and Cu substrates shows that there is some selectivity on the CMP Cu with 50 ALD cycles. This selectivity was quantified using the atomic percent Zr on Si divided by the atomic percent Zr on Cu, and was found to be ~ 7 for 50 ALD cycles and ~ 2.5 for 70 ALD cycles. This result contrasts with our work on electron beam evaporated [108] and electroplated copper which showed no ZrO_2 for up to 70 ALD cycles. Additionally, a N 1s peak is visible on the CMP copper substrate after 50 ALD cycles which suggests that the BTA coating isn't removed by the 5-minute EtOH treatment or the ZrO_2 ALD process.

As our work on electroplated copper showed that differences in copper oxides do not significantly affect the SALD process, we studied the effect of prolonged EtOH treatment and heating at on the copper surface and BTA-Cu complex. BTA has been extensively studied and has been found to desorb from the Cu surface at temperatures above approximately 300°C . [124] However, the effect of EtOH treatment on BTA has not been reported. EtOH treatment was performed for 60 minutes at 1500 mTorr and 200°C and the heat treatment was performed by heating the substrate at 335°C and 640 mTorr with N_2 flow for 60 minutes. The atomic percentages of Cu, C, O, and N from XPS survey scans of the treated and untreated CMP substrates are shown in **Table X**. Both

Substrate	Cu (At. %)	C (At. %)	O (At. %)	N (At. %)
CMP	17.4	38.4	41.6	2.6
CMP-EtOH	36.1	31.7	29.3	2.9
CMP-HT	46.7	20.9	32.4	0.0

TABLE X. ATOMIC PERCENTAGES CALCULATED FROM THE SURVEYS. CMP: CHEMICALLY MECHANICALLY POLISHED CU SUBSTRATE AFTER DI H_2O RINSE AND N_2 DRY. CMP-ETOH: CHEMICALLY MECHANICALLY POLISHED CU SUBSTRATE AFTER ETOH TREATMENT. CMP: CHEMICALLY MECHANICALLY POLISHED CU SUBSTRATE AFTER HEAT TREATMENT.

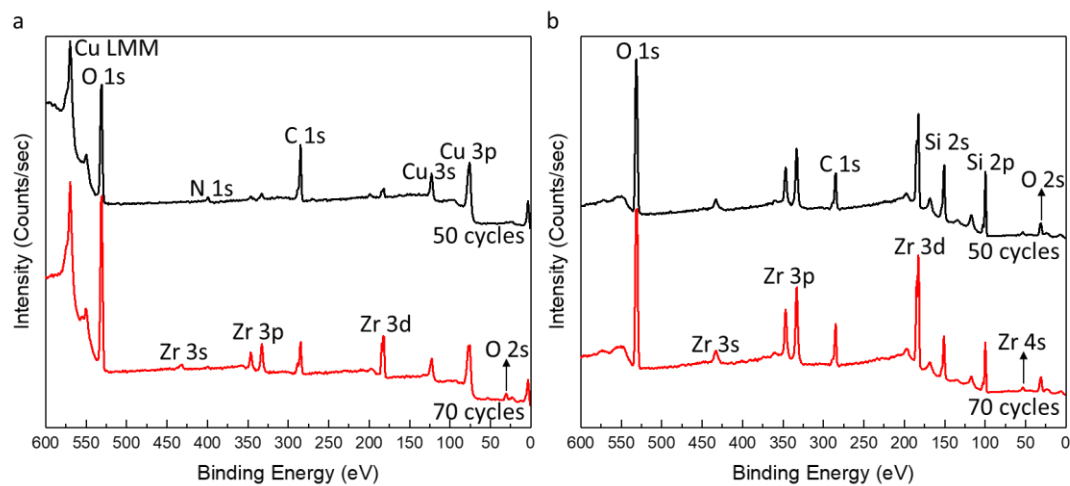


Figure 56. X-ray photoelectron spectra after 50 and 70 ALD cycles of ZrO_2 on (a) CMP copper and (b) Si substrates after a 5-minute in-situ EtOH treatment at 200°C

treatments reduced the amount of carbon and oxygen, increasing the amount of metallic copper present, but the heat-treatment appears to be more effective at removing the BTA coating as no nitrogen was detected. High resolution XPS spectra from the CMP Cu substrate before and after these different treatments are shown in **Figure 57**. Seen again here, both treatments reduce the carbon and oxygen present on the surface, but here we also see less carbonate in **Figure 57a** at ~ 289.3 eV. However, the heat treatment appears to be more effective at removing the BTA coating as the nitrogen peak is entirely removed. The heat treatment also appears to produce a more metallic copper surface as indicated by the larger Cu content and larger Cu LMM peak at ~ 918.7 eV on the kinetic energy scale in **Figure 57c**. The less metallic surface for the EtOH treated CMP substrate may be due to byproducts from the EtOH reduction of the copper oxides, which remain in the reactor for some time, and oxidize the sample after the EtOH treatment. This result is supported by our work on electroplated copper which has shown that prolonged EtOH treatments deposit byproducts on Cu substrates which serve as nucleation sites and reduce selectivity. Therefore, ZrO_2 ALD was performed using the heat-treated CMP substrates. XPS survey spectra from 70 ALD cycles of ZrO_2 on the heat-treated CMP Cu and reference Si substrates are shown in **Figure 58**. After the heat treatment and 70 ALD cycles, very little Zr was observed on the CMP substrate with only the Zr 3p and 3d peaks visible. Selectivity compared to the reference silicon sample showed $\sim 13\times$ more Zr deposited on the silicon substrate compared heat treated CMP substrate. Therefore, the BTA coating on the CMP substrate appears to be the main cause of lower selectivity on the CMP substrate and further improvement in the selectivity of this process may be achieved with further optimization of the surface treatment or ALD process.

6.4 Conclusions

SALD of ZrO_2 was performed using tris(dimethylamino)cyclopentadienyl zirconium and ethanol at 200°C on CMP Cu and Si substrates. XPS showed that the CMP substrate has more $\text{Cu}(\text{OH})_3/\text{CuCO}_3$ and more Cu_2O compared to electroplated Cu and a N 1s peak at ~ 399 eV due to BTA used in the polishing process. ZrO_2 ALD on the CMP substrate showed lower selectivity than was observed on electroplated and electron beam evaporated copper. Heating the CMP substrate at 335°C and 640 mTorr with N_2 flow for 60 minutes removed the N 1s peak, reduced the amount of oxide, carbonate and carbon. Consequently, higher selectivity was observed on this treated CMP substrate and is mainly attributed to the removal of the BTA coating. Further improvement in the selectivity

on the CMP substrate may be achieved with optimization of the treatment process for removing BTA, EtOH treatment following removal of BTA and/or the ALD process.

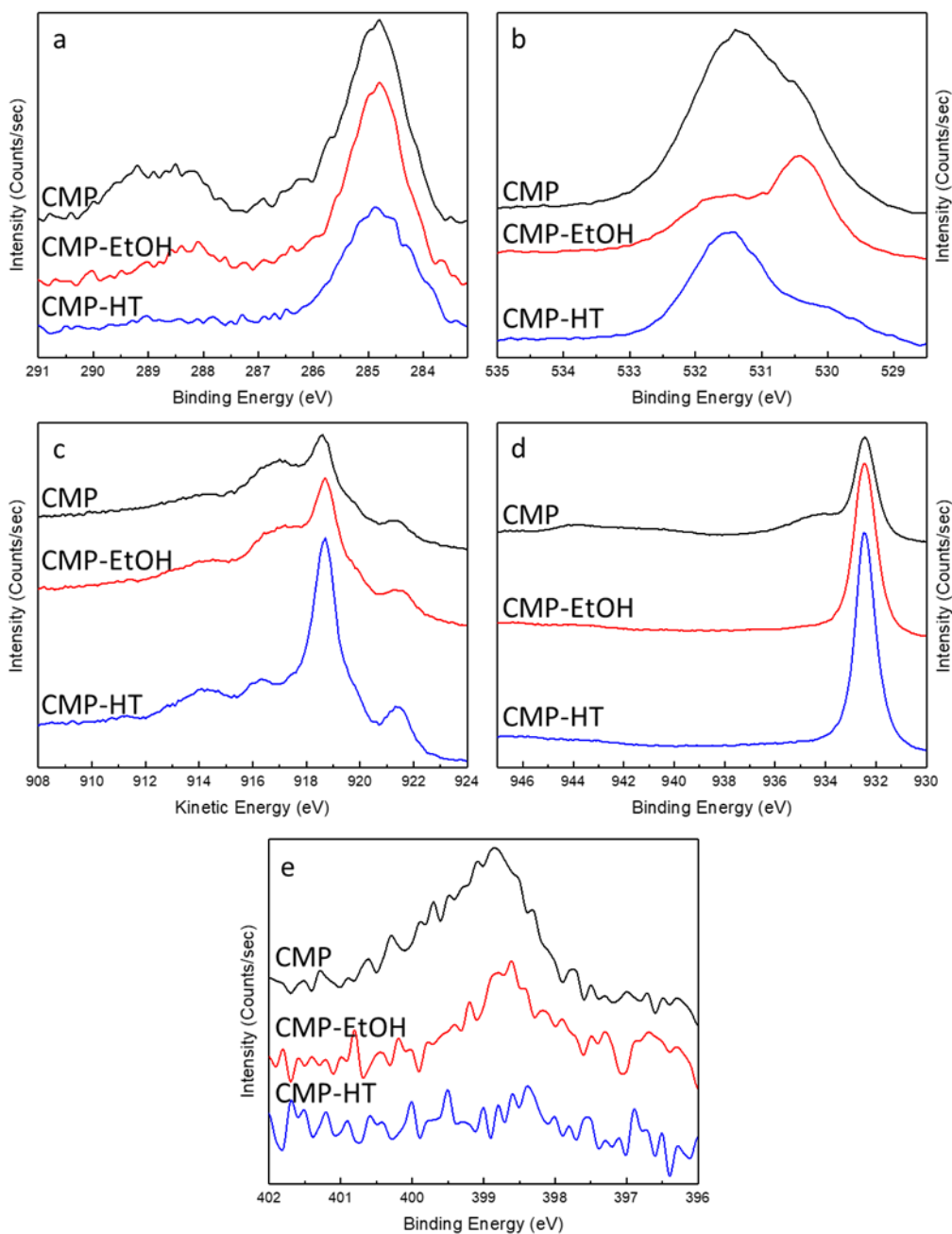


Figure 57. X-ray photoelectron spectra from CMP Cu substrates with different treatments. CMP: Spectra for the CMP Cu substrate after a DI H₂O rinse and N₂ dry. CMP-EtOH: Spectra for the CMP Cu substrate after 60 minutes of EtOH treatment at 200°C and 1500 mTorr with EtOH/N₂ flow. CMP-HT: Spectra for the CMP Cu substrate after 60 minutes of heating at 335 °C and 640 mTorr with N₂ flow. Spectra were aligned to have the carbon 1s peak at 284.8 eV (a) C 1s. (b) O 1s. (c) Cu LMM. (d) Cu 2p. (e) N 1s.

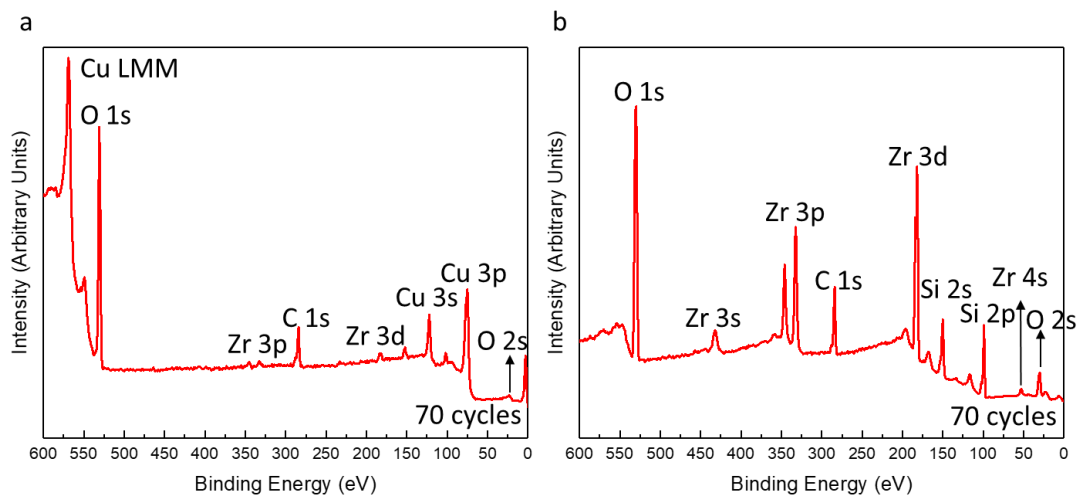


Figure 58. X-ray photoelectron spectra after 70 ALD cycles of ZrO_2 on (a) CMP copper and (b) Si substrates after a 60-minute heat treatment at 335°C and 640 mTorr and a 5-minute in-situ EtOH treatment at 200°C .

CITED LITERATURE

- [1] C.S. Smith, Piezoresistance effect in germanium and silicon, *Physical Review*. 94 (1954) 42.
- [2] Y. Kanda, Piezoresistance effect of silicon, *Sensors and Actuators A: Physical*. 28 (1991) 83–91. doi:10.1016/0924-4247(91)85017-I.
- [3] G.R. Witt, The electromechanical properties of thin films and the thin film strain gauge, *Thin Solid Films*. 22 (1974) 133–156.
- [4] V. Correia, C. Caparros, C. Casellas, L. Francesch, J.G. Rocha, S. Lanceros-Mendez, Development of inkjet printed strain sensors, *Smart Materials and Structures*. 22 (2013) 105028. doi:10.1088/0964-1726/22/10/105028.
- [5] J.C. Yeo, H.K. Yap, W. Xi, Z. Wang, C.-H. Yeow, C.T. Lim, Flexible and Stretchable Strain Sensing Actuator for Wearable Soft Robotic Applications, *Advanced Materials Technologies*. 1 (2016) 1600018. doi:10.1002/admt.201600018.
- [6] K.I. Arshak, A.K. Ray, C.A. Hogarth, D.G. Collins, F. Ansari, An analysis of polymeric thick-film resistors as pressure sensors, *Sensors and Actuators A: Physical*. 49 (1995) 41–45. doi:10.1016/0924-4247(95)01012-P.
- [7] L. Fraigi, L. Malatto, Thick-film weldable strain gauges, *Sensors and Actuators A: Physical*. 46 (1995) 222–224. doi:10.1016/0924-4247(94)00894-N.
- [8] M. Maiwald, C. Werner, V. Zoellmer, M. Busse, INKtelligent printed strain gauges, *Sensors and Actuators A: Physical*. 162 (2010) 198–201. doi:10.1016/j.sna.2010.02.019.
- [9] J.T. Muth, D.M. Vogt, R.L. Truby, Y. Mengüç, D.B. Kolesky, R.J. Wood, J.A. Lewis, Embedded 3D Printing of Strain Sensors within Highly Stretchable Elastomers, *Advanced Materials*. 26 (2014) 6307–6312. doi:10.1002/adma.201400334.
- [10] Y. Zhang, N. Anderson, S. Bland, S. Nutt, G. Jursich, S. Joshi, All-printed strain sensors: Building blocks of the aircraft structural health monitoring system, *Sensors and Actuators A: Physical*. 253 (2017) 165–172. doi:10.1016/j.sna.2016.10.007.
- [11] D. Zhao, T. Liu, M. Zhang, R. Liang, B. Wang, Fabrication and characterization of aerosol-jet printed strain sensors for multifunctional composite structures, *Smart Materials and Structures*. 21 (2012) 115008. doi:10.1088/0964-1726/21/11/115008.
- [12] Č. Žlebič, M. Kisić, N. Blaž, A. Menićanin, S. Kojić, L. Živanov, M. Damjanović, Ink-jet printed strain sensor on polyimide substrate, in: *Electronics Technology (ISSE), 2013 36th International Spring Seminar On, IEEE, 2013*: pp. 409–414.
- [13] B.F. Gonçalves, J. Oliveira, P. Costa, V. Correia, P. Martins, G. Botelho, S. Lanceros-Mendez, Development of water-based printable piezoresistive sensors for large strain applications, *Composites Part B: Engineering*. 112 (2017) 344–352. doi:10.1016/j.compositesb.2016.12.047.
- [14] H. Enser, P. Kulha, J.K. Sell, M. Schatzl-Linder, B. Strauß, W. Hilber, B. Jakoby, Printed strain gauges embedded in organic coatings - Analysis of gauge factor and temperature dependence, *Sensors and Actuators A: Physical*. 276 (2018) 137–143. doi:10.1016/j.sna.2018.03.042.
- [15] D. Zymelka, T. Yamashita, S. Takamatsu, T. Itoh, T. Kobayashi, Printed strain sensors for early damage detection in engineering structures, *Japanese Journal of Applied Physics*. 57 (2018) 05GD05. doi:10.7567/JJAP.57.05GD05.
- [16] A. Koivikko, E. Sadeghian Raei, M. Mosallaei, M. Mantysalo, V. Sariola, Screen-Printed Curvature Sensors for Soft Robots, *IEEE Sensors Journal*. 18 (2018) 223–230. doi:10.1109/JSEN.2017.2765745.
- [17] J.K. Sell, H. Enser, M. Schatzl-Linder, B. Straus, B. Jakoby, W. Hilber, Nested, meander

- shaped strain gauges for temperature compensated strain measurement, in: 2017 IEEE SENSORS, IEEE, Glasgow, 2017: pp. 1–3. doi:10.1109/ICSENS.2017.8234099.
- [18] C.A. Gutierrez, E. Meng, Low-cost carbon thick-film strain sensors for implantable applications, *Journal of Micromechanics and Microengineering*. 20 (2010) 095028. doi:10.1088/0960-1317/20/9/095028.
- [19] S. Yao, Y. Zhu, Wearable multifunctional sensors using printed stretchable conductors made of silver nanowires, *Nanoscale*. 6 (2014) 2345. doi:10.1039/c3nr05496a.
- [20] G. Dumstorff, C. Pille, R. Tiedemann, M. Busse, W. Lang, Smart aluminum components: Printed sensors for integration into aluminum during high-pressure casting, *Journal of Manufacturing Processes*. 26 (2017) 166–172. doi:10.1016/j.jmapro.2017.02.006.
- [21] T. Pinto, L. Cai, C. Wang, X. Tan, CNT-based sensor arrays for local strain measurements in soft pneumatic actuators, *International Journal of Intelligent Robotics and Applications*. 1 (2017) 157–166. doi:10.1007/s41315-017-0018-6.
- [22] H. Song, J. Zhang, D. Chen, K. Wang, S. Niu, Z. Han, L. Ren, Superfast and high-sensitivity printable strain sensors with bioinspired micron-scale cracks, *Nanoscale*. 9 (2017) 1166–1173. doi:10.1039/C6NR07333F.
- [23] Y. Hu, T. Zhao, P. Zhu, Y. Zhang, X. Liang, R. Sun, C.-P. Wong, A low-cost, printable, and stretchable strain sensor based on highly conductive elastic composites with tunable sensitivity for human motion monitoring, *Nano Research*. 11 (2018) 1938–1955. doi:10.1007/s12274-017-1811-0.
- [24] M. Mohammed Ali, D. Maddipatla, B.B. Narakathu, A.A. Chlahawi, S. Emamian, F. Janabi, B.J. Bazuin, M.Z. Atashbar, Printed strain sensor based on silver nanowire/silver flake composite on flexible and stretchable TPU substrate, *Sensors and Actuators A: Physical*. 274 (2018) 109–115. doi:10.1016/j.sna.2018.03.003.
- [25] A.P. Kondratov, A.M. Zueva, R.S. Varakin, I.P. Taranec, I.A. Savenkova, Polymer film strain gauges for measuring large elongations, *IOP Conference Series: Materials Science and Engineering*. 312 (2018) 012013. doi:10.1088/1757-899X/312/1/012013.
- [26] M. Prudenziati, J. Hormadaly, *Printed Films: Materials Science and Applications in Sensors, Electronics and Photonics*, Elsevier, 2012.
- [27] T.D. Gupta, T. Gacoin, A.C.H. Rowe, Piezoresistive Properties of Ag/Silica Nano-Composite Thin Films Close to the Percolation Threshold, *Advanced Functional Materials*. 24 (2014) 4522–4527. doi:10.1002/adfm.201303775.
- [28] A. Moorthi, B.B. Narakathu, A.S.G. Reddy, A. Eshkeiti, H. Bohra, M.Z. Atashbar, A novel flexible strain gauge sensor fabricated using screen printing, in: *Sensing Technology (ICST), 2012 Sixth International Conference On*, IEEE, 2012: pp. 765–768.
- [29] S. Lee, J. Koo, S.-K. Kang, G. Park, Y.J. Lee, Y.-Y. Chen, S.A. Lim, K.-M. Lee, J.A. Rogers, Metal microparticle – Polymer composites as printable, bio/ecoresorbable conductive inks, *Materials Today*. 21 (2018) 207–215. doi:10.1016/j.mattod.2017.12.005.
- [30] A. Bessonov, M. Kirikova, S. Haque, I. Gartsev, M.J.A. Bailey, Highly reproducible printable graphite strain gauges for flexible devices, *Sensors and Actuators A: Physical*. 206 (2014) 75–80. doi:10.1016/j.sna.2013.11.034.
- [31] M. Hrovat, J. Holc, D. Belavič, S. Šoba, An evaluation of some commercial thick film resistor materials for strain gauges, *Journal of Materials Science Letters*. 13 (1994) 992–995.
- [32] C. Canali, D. Malvasi, B. Morten, M. Prudenziati, A. Taroni, Strain sensitivity in thick-film resistors, *IEEE Transactions on Components, Hybrids, and Manufacturing Technology*. 3 (1980) 421–423.
- [33] M. Prudenziati, B. Morten, A. Taroni, Characterization of thick-film resistor strain gauges on enamel steel, *Sensors and Actuators*. 2 (1981) 17–27. doi:10.1016/0250-

6874(81)80025-X.

- [34] F. Yin, D. Ye, C. Zhu, L. Qiu, Y. Huang, Stretchable, Highly Durable Ternary Nanocomposite Strain Sensor for Structural Health Monitoring of Flexible Aircraft, *Sensors*. 17 (2017) 2677. doi:10.3390/s17112677.
- [35] DuPont, DuPont 7082 Carbon Conductor, (2012).
<http://www.dupont.com/content/dam/dupont/products-and-services/electronic-and-electrical-materials/documents/prodlib/7082.pdf> (accessed March 11, 2018).
- [36] DuPont, DuPont 5028 Silver Conductor, (2014).
<http://www.dupont.com/content/dam/dupont/products-and-services/electronic-and-electrical-materials/documents/prodlib/5028.pdf> (accessed March 11, 2018).
- [37] M. Beygi, S. Mutlu, B. Güçlü, A microfabricated strain gauge array on polymer substrate for tactile neuroprostheses in rats, *Journal of Micromechanics and Microengineering*. 26 (2016) 084006. doi:10.1088/0960-1317/26/8/084006.
- [38] E.-S. Hwang, Y.-J. Kim, Flexible Polysilicon Strain Gauge Array, *Japanese Journal of Applied Physics*. 42 (2003) L810–L813. doi:10.1143/JJAP.42.L810.
- [39] Y. Kervran, O. De Sagazan, S. Crand, N. Coulon, T. Mohammed-Brahim, O. Brel, Microcrystalline silicon: Strain gauge and sensor arrays on flexible substrate for the measurement of high deformations, *Sensors and Actuators A: Physical*. 236 (2015) 273–280. doi:10.1016/j.sna.2015.08.001.
- [40] T. Yamashita, S. Takamatsu, H. Okada, T. Itoh, T. Kobayashi, Ultra-Thin Piezoelectric Strain Sensor Array Integrated on a Flexible Printed Circuit Involving Transfer Printing Methods, *IEEE Sensors Journal*. 16 (2016) 8840–8846. doi:10.1109/JSEN.2016.2578936.
- [41] S.M. Won, H.-S. Kim, N. Lu, D.-G. Kim, C. Del Solar, T. Duenas, A. Ameen, J.A. Rogers, Piezoresistive Strain Sensors and Multiplexed Arrays Using Assemblies of Single-Crystalline Silicon Nanoribbons on Plastic Substrates, *IEEE Transactions on Electron Devices*. 58 (2011) 4074–4078. doi:10.1109/TED.2011.2164923.
- [42] X. Cao, H. Chen, X. Gu, B. Liu, W. Wang, Y. Cao, F. Wu, C. Zhou, Screen Printing as a Scalable and Low-Cost Approach for Rigid and Flexible Thin-Film Transistors Using Separated Carbon Nanotubes, *ACS Nano*. 8 (2014) 12769–12776. doi:10.1021/nn505979j.
- [43] Cheong Min Hong, S. Wagner, Inkjet printed copper source/drain metallization for amorphous silicon thin-film transistors, *IEEE Electron Device Lett.* 21 (2000) 384–386. doi:10.1109/55.852958.
- [44] R. Parashkov, E. Becker, G. Ginev, T. Riedl, H.-H. Johannes, W. Kowalsky, All-organic thin-film transistors made of poly(3-butylthiophene) semiconducting and various polymeric insulating layers, *Journal of Applied Physics*. 95 (2004) 1594–1596. doi:10.1063/1.1636524.
- [45] H.-Y. Tseng, V. Subramanian, All inkjet-printed, fully self-aligned transistors for low-cost circuit applications, *Organic Electronics*. 12 (2011) 249–256. doi:10.1016/j.orgel.2010.11.013.
- [46] P.H. Lau, K. Takei, C. Wang, Y. Ju, J. Kim, Z. Yu, T. Takahashi, G. Cho, A. Javey, Fully Printed, High Performance Carbon Nanotube Thin-Film Transistors on Flexible Substrates, *Nano Lett.* 13 (2013) 3864–3869. doi:10.1021/nl401934a.
- [47] M. Hambsch, K. Reuter, M. Stanel, G. Schmidt, H. Kempa, U. Fügmann, U. Hahn, A.C. Hübler, Uniformity of fully gravure printed organic field-effect transistors, *Materials Science and Engineering: B*. 170 (2010) 93–98. doi:10.1016/j.mseb.2010.02.035.
- [48] A. de la Fuente Vornbrock, D. Sung, H. Kang, R. Kitsomboonloha, V. Subramanian, Fully gravure and ink-jet printed high speed pBTTT organic thin film transistors, *Organic Electronics*. 11 (2010) 2037–2044. doi:10.1016/j.orgel.2010.09.003.

- [49] D. Tobjörk, N.J. Kaihovirta, T. Mäkelä, F.S. Pettersson, R. Österbacka, All-printed low-voltage organic transistors, *Organic Electronics*. 9 (2008) 931–935. doi:10.1016/j.orgel.2008.06.016.
- [50] M. Jung, J. Kim, J. Noh, N. Lim, C. Lim, G. Lee, J. Kim, H. Kang, K. Jung, A.D. Leonard, J.M. Tour, G. Cho, All-Printed and Roll-to-Roll-Printable 13.56-MHz-Operated 1-bit RF Tag on Plastic Foils, *IEEE Trans. Electron Devices*. 57 (2010) 571–580. doi:10.1109/TED.2009.2039541.
- [51] S.H. Lee, M.H. Choi, S.H. Han, D.J. Choo, J. Jang, S.K. Kwon, High-performance thin-film transistor with 6,13-bis(triisopropylsilyl)ethynyl) pentacene by inkjet printing, *Organic Electronics*. 9 (2008) 721–726. doi:10.1016/j.orgel.2008.05.002.
- [52] D.T. James, B.K.C. Kjellander, W.T.T. Smaal, G.H. Gelinck, C. Combe, I. McCulloch, R. Wilson, J.H. Burroughes, D.D.C. Bradley, J.-S. Kim, Thin-Film Morphology of Inkjet-Printed Single-Droplet Organic Transistors Using Polarized Raman Spectroscopy: Effect of Blending TIPS-Pentacene with Insulating Polymer, *ACS Nano*. 5 (2011) 9824–9835. doi:10.1021/nn203397m.
- [53] J.R. Davis, ASM International, eds., *Copper and copper alloys*, ASM International, Materials Park, OH, 2001.
- [54] R.J. Horwood, *TOWARDS A BETTER UNDERSTANDING OF SCREEN PRINT THICKNESS CONTROL*, (n.d.) 9.
- [55] F. Cverna, *ASM Ready Reference: Thermal properties of metals*, ASM International, 2002.
- [56] R.S. Okojie, A.A. Ned, A.D. Kurtz, Operation of $\alpha(6H)$ -SiC pressure sensor at 500 °C, *Sensors and Actuators A: Physical*. 66 (1998) 200–204. doi:10.1016/S0924-4247(98)00009-0.
- [57] A. García-Alonso, J. García, E. Castaño, I. Obieta, F.J. Gracia, Strain sensitivity and temperature influence on sputtered thin films for piezoresistive sensors, *Sensors and Actuators A: Physical*. 37–38 (1993) 784–789. doi:10.1016/0924-4247(93)80132-Z.
- [58] L. Ghasemi-Mobarakeh, M.P. Prabhakaran, M. Morshed, M.H. Nasr-Esfahani, H. Baharvand, S. Kiani, S.S. Al-Deyab, S. Ramakrishna, Application of conductive polymers, scaffolds and electrical stimulation for nerve tissue engineering, *Journal of Tissue Engineering and Regenerative Medicine*. 5 (2011) e17–e35. doi:10.1002/term.383.
- [59] T.F. Otero, J.G. Martinez, J. Arias-Pardilla, Biomimetic electrochemistry from conducting polymers. A review, *Electrochimica Acta*. 84 (2012) 112–128. doi:10.1016/j.electacta.2012.03.097.
- [60] J.Y. Wong, R. Langer, D.E. Ingber, Electrically conducting polymers can noninvasively control the shape and growth of mammalian cells., *Proceedings of the National Academy of Sciences*. 91 (1994) 3201–3204. doi:10.1073/pnas.91.8.3201.
- [61] M.R. Abidian, D.C. Martin, Experimental and theoretical characterization of implantable neural microelectrodes modified with conducting polymer nanotubes, *Biomaterials*. 29 (2008) 1273–1283. doi:10.1016/j.biomaterials.2007.11.022.
- [62] M. Asplund, T. Nyberg, O. Inganäs, Electroactive polymers for neural interfaces, *Polymer Chemistry*. 1 (2010) 1374. doi:10.1039/c0py00077a.
- [63] S. Baek, R.A. Green, L.A. Poole-Warren, The biological and electrical trade-offs related to the thickness of conducting polymers for neural applications, *Acta Biomaterialia*. 10 (2014) 3048–3058. doi:10.1016/j.actbio.2014.04.004.
- [64] P.A. Forcelli, C.T. Sweeney, A.D. Kammerich, B.C.-W. Lee, L.H. Robinson, Y.P. Kayinamura, K. Gale, J.F. Robinson, Histocompatibility and *in vivo* signal throughput for PEDOT, PEDOP, P3MT, and polycarbazole electrodes: Histocompatibility and *In Vivo* Signal throughput for Polymers, *Journal of Biomedical Materials Research Part A*. 100A

- (2012) 3455–3462. doi:10.1002/jbm.a.34285.
- [65] R.A. Green, N.H. Lovell, G.G. Wallace, L.A. Poole-Warren, Conducting polymers for neural interfaces: Challenges in developing an effective long-term implant, *Biomaterials*. 29 (2008) 3393–3399. doi:10.1016/j.biomaterials.2008.04.047.
- [66] M.R. Abidian, D.-H. Kim, D.C. Martin, Conducting-Polymer Nanotubes for Controlled Drug Release, *Advanced Materials*. 18 (2006) 405–409. doi:10.1002/adma.200501726.
- [67] C. Boehler, M. Asplund, A detailed insight into drug delivery from PEDOT based on analytical methods: Effects and side effects: A DETAILED INSIGHT INTO DRUG DELIVERY, *Journal of Biomedical Materials Research Part A*. 103 (2015) 1200–1207. doi:10.1002/jbm.a.35252.
- [68] S. Geetha, C.R.K. Rao, M. Vijayan, D.C. Trivedi, Biosensing and drug delivery by polypyrrole, *Analytica Chimica Acta*. 568 (2006) 119–125. doi:10.1016/j.aca.2005.10.011.
- [69] K. Krukiewicz, T. Jarosz, J.K. Zak, M. Lapkowski, P. Ruszkowski, T. Bobkiewicz-Kozłowska, B. Bednarczyk-Cwynar, Advancing the delivery of anticancer drugs: Conjugated polymer/triterpenoid composite, *Acta Biomaterialia*. 19 (2015) 158–165. doi:10.1016/j.actbio.2015.03.006.
- [70] F. Carpi, E. Smela, eds., *Biomedical Applications of Electroactive Polymer Actuators*, John Wiley & Sons, Ltd, Chichester, UK, 2009. doi:10.1002/9780470744697.
- [71] I.S. Romero, N.P. Bradshaw, J.D. Larson, S.Y. Severt, S.J. Roberts, M.L. Schiller, J.M. Leger, A.R. Murphy, Biocompatible Electromechanical Actuators Composed of Silk-Conducting Polymer Composites, *Advanced Functional Materials*. 24 (2014) 3866–3873. doi:10.1002/adfm.201303292.
- [72] E. Smela, Conjugated Polymer Actuators for Biomedical Applications, *Advanced Materials*. 15 (2003) 481–494. doi:10.1002/adma.200390113.
- [73] H. Xu, C. Wang, C. Wang, J. Zoval, M. Madou, Polymer actuator valves toward controlled drug delivery application, *Biosensors and Bioelectronics*. 21 (2006) 2094–2099. doi:10.1016/j.bios.2005.10.020.
- [74] M. Irimia-Vladu, “Green” electronics: biodegradable and biocompatible materials and devices for sustainable future, *Chem. Soc. Rev.* 43 (2014) 588–610. doi:10.1039/C3CS60235D.
- [75] H. Cheng, V. Vepachedu, Recent development of transient electronics, *Theoretical and Applied Mechanics Letters*. 6 (2016) 21–31. doi:10.1016/j.taml.2015.11.012.
- [76] K.K. Fu, Z. Wang, J. Dai, M. Carter, L. Hu, Transient Electronics: Materials and Devices, *Chemistry of Materials*. 28 (2016) 3527–3539. doi:10.1021/acs.chemmater.5b04931.
- [77] S.-W. Hwang, H. Tao, D.-H. Kim, H. Cheng, J.-K. Song, E. Rill, M.A. Brenckle, B. Panilaitis, S.M. Won, Y.-S. Kim, Y.M. Song, K.J. Yu, A. Ameen, R. Li, Y. Su, M. Yang, D.L. Kaplan, M.R. Zakin, M.J. Slepian, Y. Huang, F.G. Omenetto, J.A. Rogers, A Physically Transient Form of Silicon Electronics, *Science*. 337 (2012) 1640–1644. doi:10.1126/science.1226325.
- [78] S. Moreno, M. Baniasadi, S. Mohammed, I. Mejia, Y. Chen, M.A. Quevedo-Lopez, N. Kumar, S. Dimitrijevic, M. Minary-Jolandan, Biocompatible Collagen Films as Substrates for Flexible Implantable Electronics, *Advanced Electronic Materials*. 1 (2015) 1500154. doi:10.1002/aelm.201500154.
- [79] R. Khan, M. Khan, Use of collagen as a biomaterial: An update, *Journal of Indian Society of Periodontology*. 17 (2013) 539. doi:10.4103/0972-124X.118333.
- [80] J. Wang, L. Wang, Z. Zhou, H. Lai, P. Xu, L. Liao, J. Wei, Biodegradable Polymer Membranes Applied in Guided Bone/Tissue Regeneration: A Review, *Polymers*. 8 (2016) 115. doi:10.3390/polym8040115.
- [81] M. Knez, K. Nielsch, L. Niinistö, Synthesis and Surface Engineering of Complex

- Nanostructures by Atomic Layer Deposition, *Advanced Materials*. 19 (2007) 3425–3438. doi:10.1002/adma.200700079.
- [82] M. Leskelä, M. Ritala, Atomic layer deposition (ALD): from precursors to thin film structures, *Thin Solid Films*. 409 (2002) 138–146. doi:10.1016/S0040-6090(02)00117-7.
- [83] M. Knez, Application of ALD to Biomaterials and Biocompatible Coatings, in: *Atomic Layer Deposition of Nanostructured Materials*, Wiley-Blackwell, 2012: pp. 301–325. doi:10.1002/9783527639915.ch13.
- [84] J.Z. Mundy, A. Shafieifarhood, F. Li, S.A. Khan, G.N. Parsons, Low temperature platinum atomic layer deposition on nylon-6 for highly conductive and catalytic fiber mats, *Journal of Vacuum Science & Technology A: Vacuum, Surfaces, and Films*. 34 (2016) 01A152. doi:10.1116/1.4935448.
- [85] A.J.M. Mackus, D. Garcia-Alonso, H.C.M. Knoop, A.A. Bol, W.M.M. Kessels, Room-Temperature Atomic Layer Deposition of Platinum, *Chemistry of Materials*. 25 (2013) 1769–1774. doi:10.1021/cm400274n.
- [86] J. Lee, J. Yoon, H.G. Kim, S. Kang, W.-S. Oh, H. Algadi, S. Al-Sayari, B. Shong, S.-H. Kim, H. Kim, T. Lee, H.-B.-R. Lee, Highly conductive and flexible fiber for textile electronics obtained by extremely low-temperature atomic layer deposition of Pt, *NPG Asia Materials*. 8 (2016) e331–e331. doi:10.1038/am.2016.182.
- [87] S.-T. Li, H.-C. Chen, N.S. Lee, R. Ringshia, D. Yuen, A Comparative Study Of Zimmer BioMend® And BioMend® Extend™ Membranes Made At Two Different Manufacturing Facilities, (n.d.) 5.
- [88] R. Muratore, T. Akabas, I.B. Muratore, High-Intensity Focused Ultrasound Ablation of Ex Vivo Bovine Achilles Tendon, *Ultrasound in Medicine & Biology*. 34 (2008) 2043–2050. doi:10.1016/j.ultrasmedbio.2008.05.006.
- [89] H.-B.-R. Lee, S.F. Bent, Microstructure-Dependent Nucleation in Atomic Layer Deposition of Pt on TiO₂, *Chemistry of Materials*. 24 (2012) 279–286. doi:10.1021/cm202764b.
- [90] R. Xu, S.K. Selvaraj, G. Jursich, A. Feinerman, C. Takoudis, Nucleation Behavior-Morphology-Resistivity of Atomic Layer Deposited Pt on Atomic Layer Deposited Ytria-Stabilized Zirconia Films, *ECS J. Solid State Sci. Technol.* 2 (2013) P452–P456. doi:10.1149/2.017311jss.
- [91] L. Ge, C. Hu, Z. Zhu, W. Zhang, D. Wu, S. Zhang, Influence of surface preparation on atomic layer deposition of Pt films, *Journal of Semiconductors*. 33 (2012) 083003. doi:10.1088/1674-4926/33/8/083003.
- [92] A.K. Bishal, C. Sukotjo, C.G. Takoudis, Room temperature TiO₂ atomic layer deposition on collagen membrane from a titanium alkylamide precursor, *Journal of Vacuum Science & Technology A: Vacuum, Surfaces, and Films*. 35 (2017) 01B134. doi:10.1116/1.4972245.
- [93] P.-Y. Li, H.-W. Liu, T.-H. Chen, C.-H. Chang, Y.-S. Lu, D.-S. Liu, Characterization of an Amorphous Titanium Oxide Film Deposited onto a Nano-Textured Fluorination Surface, *Materials*. 9 (2016) 429. doi:10.3390/ma9060429.
- [94] H.-B.-R. Lee, K.L. Pickrahn, S.F. Bent, Effect of O₃ on Growth of Pt by Atomic Layer Deposition, *The Journal of Physical Chemistry C*. 118 (2014) 12325–12332. doi:10.1021/jp502596n.
- [95] K. Belbachir, R. Noreen, G. Gouspillou, C. Petibois, Collagen types analysis and differentiation by FTIR spectroscopy, *Analytical and Bioanalytical Chemistry*. 395 (2009) 829–837. doi:10.1007/s00216-009-3019-y.
- [96] B.H. León-Mancilla, M.A. Araiza-Téllez, J.O. Flores-Flores, M.C. Piña-Barba, Physico-chemical characterization of collagen scaffolds for tissue engineering, *Journal of Applied Research and Technology*. 14 (2016) 77–85. doi:10.1016/j.jart.2016.01.001.

- [97] J. Bogojeski, B. Petrović, D. Ivadin, Interactions of the Platinum(II) Complexes with Nitrogen- and Sulfur-Bonding Bio-Molecules in Chronic Lymphocytic Leukemia, in: P. Oppezzo (Ed.), *Chronic Lymphocytic Leukemia*, InTech, 2012. doi:10.5772/28585.
- [98] B.J. Reedijk, Metal-Ligand Exchange Kinetics in Platinum and Ruthenium Complexes, *Platinum Metals Review*. 52 (2008) 2–11. doi:10.1595/147106708X255987.
- [99] S.-M. Lee, E. Pippel, O. Moutanabbir, I. Gunkel, T. Thurn-Albrecht, M. Knez, Improved Mechanical Stability of Dried Collagen Membrane after Metal Infiltration, *ACS Applied Materials & Interfaces*. 2 (2010) 2436–2441. doi:10.1021/am100438b.
- [100] B. Karasulu, R.H.J. Vervuurt, W.M.M. Kessels, A.A. Bol, Continuous and ultrathin platinum films on graphene using atomic layer deposition: a combined computational and experimental study, *Nanoscale*. 8 (2016) 19829–19845. doi:10.1039/C6NR07483A.
- [101] N. Lu, Z. Suo, J.J. Vlassak, The effect of film thickness on the failure strain of polymer-supported metal films, *Acta Materialia*. 58 (2010) 1679–1687. doi:10.1016/j.actamat.2009.11.010.
- [102] R. Clark, K. Tapily, K.-H. Yu, T. Hakamata, S. Consiglio, D. O'Meara, C. Wajda, J. Smith, G. Leusink, Perspective: New process technologies required for future devices and scaling, *APL Materials*. 6 (2018) 058203. doi:10.1063/1.5026805.
- [103] A.J.M. Mackus, A.A. Bol, W.M.M. Kessels, The use of atomic layer deposition in advanced nanopatterning, *Nanoscale*. 6 (2014) 10941–10960. doi:10.1039/C4NR01954G.
- [104] A.J.M. Mackus, M.J.M. Merkx, W.M.M. Kessels, From the Bottom-Up: Toward Area-Selective Atomic Layer Deposition with High Selectivity, *Chemistry of Materials*. 31 (2019) 2–12. doi:10.1021/acs.chemmater.8b03454.
- [105] K. Cao, J. Cai, X. Liu, R. Chen, Review Article: Catalysts design and synthesis via selective atomic layer deposition, *Journal of Vacuum Science & Technology A: Vacuum, Surfaces, and Films*. 36 (2018) 010801. doi:10.1116/1.5000587.
- [106] S. Seo, B.C. Yeo, S.S. Han, C.M. Yoon, J.Y. Yang, J. Yoon, C. Yoo, H. Kim, Y. Lee, S.J. Lee, J.-M. Myoung, H.-B.-R. Lee, W.-H. Kim, I.-K. Oh, H. Kim, Reaction Mechanism of Area-Selective Atomic Layer Deposition for Al₂O₃ Nanopatterns, *ACS Applied Materials & Interfaces*. 9 (2017) 41607–41617. doi:10.1021/acsami.7b13365.
- [107] Q. Tao, G. Jursich, C. Takoudis, Selective atomic layer deposition of HfO₂ on copper patterned silicon substrates, *Applied Physics Letters*. 96 (2010) 192105. doi:10.1063/1.3428771.
- [108] S. Kannan Selvaraj, J. Parulekar, C.G. Takoudis, Selective atomic layer deposition of zirconia on copper patterned silicon substrates using ethanol as oxygen source as well as copper reductant, *Journal of Vacuum Science & Technology A: Vacuum, Surfaces, and Films*. 32 (2014) 010601. doi:10.1116/1.4826941.
- [109] Q. Tao, K. Overhage, G. Jursich, C. Takoudis, On the initial growth of atomic layer deposited TiO₂ films on silicon and copper surfaces, *Thin Solid Films*. 520 (2012) 6752–6756. doi:10.1016/j.tsf.2012.07.004.
- [110] M. Junige, M. Löffler, M. Geidel, M. Albert, J.W. Bartha, E. Zschech, B. Rellinghaus, W.F. van Dorp, Area-selective atomic layer deposition of Ru on electron-beam-written Pt(C) patterns versus SiO₂ substratum, *Nanotechnology*. 28 (2017) 395301. doi:10.1088/1361-6528/aa8844.
- [111] M. Pešić, S. Knebel, M. Geyer, S. Schmelzer, U. Böttger, N. Kolomiiets, V.V. Afanas'ev, K. Cho, C. Jung, J. Chang, H. Lim, T. Mikolajick, U. Schroeder, Low leakage ZrO₂ based capacitors for sub 20 nm dynamic random access memory technology nodes, *Journal of Applied Physics*. 119 (2016) 064101. doi:10.1063/1.4941537.
- [112] R. Oxland, X. Li, S.W. Chang, S.W. Wang, T. Vasen, P. Ramvall, R. Contreras-Guerrero, J. Rojas-Ramirez, M. Holland, G. Doornbos, Y.S. Chang, D.S. Macintyre, S.

- Thoms, R. Droopad, Y.-C. Yeo, C.H. Diaz, I.G. Thayne, M. Passlack, InAs FinFETs With H_{fin} nm Fabricated Using a Top-Down Etch Process, *IEEE Electron Device Letters*. 37 (2016) 261–264. doi:10.1109/LED.2016.2521001.
- [113] N. El, B. Hadri, A. Caddemi, Simulation of a Nanoscale SOI TG n-FinFET, *International Journal of Computer Applications*. 138 (2016) 10–14. doi:10.5120/ijca2016908981.
- [114] D. Kennouche, Y.K. Chen-Wiegart, K.J. Yakal-Kremiski, J. Wang, J.W. Gibbs, P.W. Voorhees, S.A. Barnett, Observing the microstructural evolution of Ni-Yttria-stabilized zirconia solid oxide fuel cell anodes, *Acta Materialia*. 103 (2016) 204–210. doi:10.1016/j.actamat.2015.09.055.
- [115] V. Encinas-Sánchez, A. Macías-García, M.A. Díaz-Díez, P. Brito, D. Cardoso, Influence of the quality and uniformity of ceramic coatings on corrosion resistance, *Ceramics International*. 41 (2015) 5138–5146. doi:10.1016/j.ceramint.2014.12.087.
- [116] T. Witton, J. Chalorntham, P. Dumrongbunditkul, M. Chareonpanich, J. Limtrakul, CO₂ hydrogenation to methanol over Cu/ZrO₂ catalysts: Effects of zirconia phases, *Chemical Engineering Journal*. 293 (2016) 327–336. doi:10.1016/j.cej.2016.02.069.
- [117] Y. Song, J.-H. Seo, Y.-S. Lee, Y.-H. Ryu, K. Hong, S.-K. Rha, Characterization of Electroplated Cu Thin Films on Electron-Beam-Evaporated Cu Seed Layers, *Journal of the Korean Physical Society*. 54 (2009) 1141–1145. doi:10.3938/jkps.54.1141.
- [118] X. Wang, J.C. Hanson, A.I. Frenkel, J.-Y. Kim, J.A. Rodriguez, Time-resolved Studies for the Mechanism of Reduction of Copper Oxides with Carbon Monoxide: Complex Behavior of Lattice Oxygen and the Formation of Suboxides, *The Journal of Physical Chemistry B*. 108 (2004) 13667–13673. doi:10.1021/jp040366o.
- [119] E.A. Goldstein, R.E. Mitchell, Chemical kinetics of copper oxide reduction with carbon monoxide, *Proceedings of the Combustion Institute*. 33 (2011) 2803–2810. doi:10.1016/j.proci.2010.06.080.
- [120] S. Poulston, P.M. Parlett, P. Stone, M. Bowker, Surface Oxidation and Reduction of CuO and Cu₂O Studied Using XPS and XAES, *Surface and Interface Analysis*. 24 (1996) 811–820. doi:10.1002/(SICI)1096-9918(199611)24:12<811::AID-SIA191>3.0.CO;2-Z.
- [121] P.J. Soininen, K.-E. Elers, V. Saanila, S. Kaipio, T. Sajavaara, S. Haukka, Reduction of Copper Oxide Film to Elemental Copper, *Journal of The Electrochemical Society*. 152 (2005) G122. doi:10.1149/1.1839491.
- [122] A. Satta, D. Shamiryan, M.R. Baklanov, C.M. Whelan, Q. Toan Le, G.P. Beyer, A. Vantomme, K. Maex, The Removal of Copper Oxides by Ethyl Alcohol Monitored In Situ by Spectroscopic Ellipsometry, *Journal of The Electrochemical Society*. 150 (2003) G300. doi:10.1149/1.1564108.
- [123] L. Lecordier, S. Herregods, S. Armini, Vapor-deposited octadecanethiol masking layer on copper to enable area selective Hf₃N₄ atomic layer deposition on dielectrics studied by *in situ* spectroscopic ellipsometry, *Journal of Vacuum Science & Technology A*. 36 (2018) 031605. doi:10.1116/1.5025688.
- [124] L.F. Peña, J.-F. Veyan, M.A. Todd, A. Derecskei-Kovacs, Y.J. Chabal, Vapor-Phase Cleaning and Corrosion Inhibition of Copper Films by Ethanol and Heterocyclic Amines, *ACS Applied Materials & Interfaces*. 10 (2018) 38610–38620. doi:10.1021/acsami.8b13438.
- [125] C.-C. Chang, M.-C. Shu, The Chemical Origin of Defects on Silicon Dioxide Exposed to Ethanol, *J. Phys. Chem. B*. 107 (2003) 7076–7087. doi:10.1021/jp027372+.
- [126] L.L. Tedder, G. Lu, J.E. Crowell, Mechanistic studies of dielectric thin film growth by low pressure chemical vapor deposition: The reaction of tetraethoxysilane with SiO₂ surfaces, *Journal of Applied Physics*. 69 (1991) 7037–7049. doi:10.1063/1.348932.
- [127] R. Xu, Q. Tao, Y. Yang, C.G. Takoudis, Atomic layer deposition and characterization of

- stoichiometric erbium oxide thin dielectrics on Si(100) using (CpMe)₃Er precursor and ozone, *Applied Surface Science*. 258 (2012) 8514–8520. doi:10.1016/j.apsusc.2012.05.019.
- [128] N. Jayaraju, L. Barstad, D. Cleary, Z. Niazimbetova, T. Liao, C. Grand, J. Dziewiszek, M. Rzeznik, M. Lin, D. Yee, Next generation electrolytic copper plating process for HDI applications, in: 2016 11th International Microsystems, Packaging, Assembly and Circuits Technology Conference (IMPACT), IEEE, Taipei, Taiwan, 2016: pp. 52–55. doi:10.1109/IMPACT.2016.7800078.
- [129] M.C. Biesinger, Advanced analysis of copper X-ray photoelectron spectra: Advanced analysis of copper X-ray photoelectron spectra, *Surface and Interface Analysis*. 49 (2017) 1325–1334. doi:10.1002/sia.6239.
- [130] C. Zhu, A. Osherov, M.J. Panzer, Surface chemistry of electrodeposited Cu₂O films studied by XPS, *Electrochimica Acta*. 111 (2013) 771–778. doi:10.1016/j.electacta.2013.08.038.
- [131] C. James, R. Xu, G. Jursich, C.G. Takoudis, Atomic Layer Deposition of Zirconium Oxide for Fuel Cell Applications, *The Journal of Undergraduate Research at the University of Illinois at Chicago*. 5 (2012). doi:10.5210/jur.v5i1.7505.
- [132] P. Keil, D. Lützenkirchen-Hecht, R. Frahm, Investigation of Room Temperature Oxidation of Cu in Air by Yoneda-XAFS, in: AIP Conference Proceedings, AIP, Stanford, California (USA), 2007: pp. 490–492. doi:10.1063/1.2644569.
- [133] W. Gaynor, C.G. Takoudis, G.W. Neudeck, Process–property relationships between silicon selective epitaxial growth ambients and degradation of insulators, *Journal of Vacuum Science & Technology A*. 14 (1996) 3224–3227. doi:10.1116/1.580217.
- [134] Christos G. Takoudis, Unpublished Results. (2019).
- [135] H. Rajesh, U.S. Ozkan, Complete oxidation of ethanol, acetaldehyde and ethanol/methanol mixtures over copper oxide and copper-chromium oxide catalysts, *Industrial & Engineering Chemistry Research*. 32 (1993) 1622–1630. doi:10.1021/ie00020a013.
- [136] X. Deng, A. Verdager, T. Herranz, C. Weis, H. Bluhm, M. Salmeron, Surface Chemistry of Cu in the Presence of CO₂ and H₂O, *Langmuir*. 24 (2008) 9474–9478. doi:10.1021/la8011052.
- [137] Mordechai Schlesinger, *Modern Electroplating*, Fifth, John Wiley & Sons, Ltd, 2010. 10.1002/9780470602638.
- [138] J.M. Steigerwald, S.P. Murarka, R.J. Gutmann, D.J. Duquette, Chemical processes in the chemical mechanical polishing of copper, *Materials Chemistry and Physics*. 41 (1995) 217–228. doi:10.1016/0254-0584(95)01516-7.
- [139] T. Gupta, *Copper Interconnect Technology*, Springer Science & Business Media, 2010.
- [140] T. Stanczyk, K. Wysokinski, M. Filipowicz, T. Tenderenda, K. Gibala, H. Krisch, M. Slowikowski, A. Ziolkowicz, M. Broczkowska, T. Nasilowski, Electrolytic Joints Between Metal Surfaces and Metal-Coated Fibers for Application in High Temperature Optical Fiber Sensors, *J. Lightwave Technol.* 33 (2015) 2480–2485. doi:10.1109/JLT.2014.2378031.
- [141] A. Rehman, S. Lee, Review of the Potential of the Ni/Cu Plating Technique for Crystalline Silicon Solar Cells, *Materials*. 7 (2014) 1318–1341. doi:10.3390/ma7021318.
- [142] R.F. Yanda, M. Heynes, A. Miller, A. Miller, *Demystifying Chipmaking*, Elsevier Science & Technology, Oxford, UNITED STATES, 2005. <http://ebookcentral.proquest.com/lib/uic/detail.action?docID=234967> (accessed March 8, 2019).
- [143] P.M. Vereecken, R.A. Binstead, H. Deligianni, P.C. Andricacos, *The chemistry of*

- additives in damascene copper plating, IBM Journal of Research and Development. 49 (2005) 3–18. doi:10.1147/rd.491.0003.
- [144] S. Hegde, U.B. Patri, S.V. Babu, Chemical-mechanical Polishing of Copper Using Molybdenum Dioxide Slurry, Journal of Materials Research. 20 (2005) 2553–2561. doi:10.1557/jmr.2005.0305.
- [145] Y. Ein-Eli, D. Starosvetsky, Review on copper chemical–mechanical polishing (CMP) and post-CMP cleaning in ultra large system integrated (ULSI)—An electrochemical perspective, Electrochimica Acta. 52 (2007) 1825–1838. doi:10.1016/j.electacta.2006.07.039.
- [146] N.K. Allam, A.A. Nazeer, E.A. Ashour, A review of the effects of benzotriazole on the corrosion of copper and copper alloys in clean and polluted environments, Journal of Applied Electrochemistry. 39 (2009) 961–969. doi:10.1007/s10800-009-9779-4.
- [147] B. Zhang, Y. Liu, C. Wang, BTA Free Alkaline Slurries Developed for Copper and Barrier CMP, ECS J. Solid State Sci. Technol. 4 (2015) P5112–P5117. doi:10.1149/2.0171511jss.
- [148] P.C. Goonetilleke, D. Roy, Relative roles of acetic acid, dodecyl sulfate and benzotriazole in chemical mechanical and electrochemical mechanical planarization of copper, Applied Surface Science. 254 (2008) 2696–2707. doi:10.1016/j.apsusc.2007.10.005.
- [149] M. Favaro, H. Xiao, T. Cheng, W.A. Goddard, J. Yano, E.J. Crumlin, Subsurface oxide plays a critical role in CO₂ activation by Cu(111) surfaces to form chemisorbed CO₂, the first step in reduction of CO₂, Proceedings of the National Academy of Sciences. (2017) 201701405. doi:10.1073/pnas.1701405114.
- [150] Z. Gu, Y. Liu, B. Gao, C. Wang, H. Deng, A novel compound cleaning solution for benzotriazole removal after copper CMP, Journal of Semiconductors. 36 (2015) 106001. doi:10.1088/1674-4926/36/10/106001.

APPENDICES

Appendix A

PERMISSION TO USE PREVIOUSLY PUBLISHED MATERIALS

Chapter 2 was previously published as “Screen Printed Strain Gauges and Ink Composition Optimization” in Sensors and Actuators A: Physical. This journal allows authors to use their articles in full or in part in a thesis or dissertation. The following statement is given on their webpage,

<https://www.elsevier.com/about/policies/copyright/permissions>.

“Can I include/use my article in my thesis/dissertation? - Yes. Authors can include their articles in full or in part in a thesis or dissertation for non-commercial purposes.”

Parts of Chapter 3 were previously published as “All-printed strain sensors: Building blocks of the aircraft structural health monitoring systems” in Sensors and Actuators A: Physical and as “Challenges and the state of the technology for printed sensor arrays for structural monitoring” in SPIE: Industrial and Commercial Applications of Smart Structures Technologies. The statement from Sensors and Actuators A: Physical is shown above. SPIE: Industrial and Commercial Applications of Smart Structures Technologies provides permission to authors to reproduce their original figures and text in new publications. The following statement is provided on their webpage,

<https://www.spiedigitallibrary.org/article-sharing-policies>.

“For articles published under SPIE copyright, authors, or their employers in the case of works made for hire, retain the following rights:

- All proprietary rights other than copyright, including patent rights.
- The right to make and distribute copies of the Paper for internal purposes.
- The right to use the material for lecture or classroom purposes.
- The right to prepare derivative publications based on the Paper, including books or book chapters, journal papers, and magazine articles, provided that publication of a derivative work occurs subsequent to the official date of publication by SPIE.

Thus, authors may reproduce their original figures and text in new publications. The SPIE source publication should be referenced; see citation formatting **below**.”

Appendix A (Continued)

Chapter 4 is under revision to be published as “Highly Conductive and Flexible Biomaterial Achieved by Low Temperature Atomic Layer Deposition on Collagen” in Biosensors and Bioelectronics. The following statement is provided on their webpage,

<https://www.elsevier.com/about/policies/copyright/permissions>

“Can I include/use my article in my thesis/dissertation? – Yes. Authors can include their articles in full or in part in a thesis or dissertation for non-commercial purposes.”

Chapter 5 has been submitted for publication as “On the Mechanism of Area Selective Atomic Layer Deposition of Zirconia on Electroplated Copper-Based Substrates” in the ECS Journal of Solid State Science and Technology. The following statement is provided on their webpage,

<http://ecsd1.org/site/ecs/copyright.xhtml>

“**PERMISSION IS NOT REQUIRED** to reuse your own content (i.e. reusing figures and/or tables from a paper you are an author on). Full credit to the original source should be given.”

Appendix B

OTHER PROJECTS

B.1 A theoretical model based on a group contribution method to describe atomic layer deposition of zirconia on silicon

Precursors for atomic layer deposition (ALD) are chemically complex compounds which are expensive to produce and characterize. These precursors require numerous properties to be suitable for ALD. These properties include, but are not limited to producing volatile, easily removable byproducts, stability at elevated temperatures, high vapor pressure, and non-self-reactivity. These properties are typically achieved with the use of different functional groups and with proper understanding of these groups, novel precursors could be developed and ALD reactions could be further characterized. Therefore, a theoretical model characterizing growth of the deposited metal oxide on the substrate was proposed. This model would allow a comparison between theoretical and experimental growth profile, could help determine the ALD window, and could provide suggestion for precursor modification or formation of a more effective or economically viable precursor. The interaction of precursor components with the substrate was estimated according to the Universal Quasi-chemical Functional-group Activity Coefficient Group Contribution Method (UNIFAC GCM) applying adsorbate solid solution theory (ASST) and a theoretical growth rate was calculated for each experimental precursor pulse using an optimization algorithm.

ALD of zirconia (ZrO_2) was performed on highly doped silicon <100> substrates with only a native oxide using tris(dimethylamino)cyclopentadienyl zirconium (ZyALD^{TM}) as the zirconium precursor and ethanol as the oxidizer. ALD was performed at 200°C in a custom-built ALD system. 70 ALD cycles with different precursor pulse times were used to study the saturation of the zirconium precursor on the silicon substrates. ZrO_2 thickness was measured via spectral ellipsometry and experimental growth rate for each precursor pulse time was found by dividing the measured thickness by the number of ALD cycles.

For the theoretical modelling, ALD was viewed as a chemisorption process. A typical chemisorption process consists of a bulk phase and a surface phase. The silicon substrate used in this study was viewed as a solid adsorbent and chemical species generated from precursor molecules were adsorbates. Once the silicon substrate is saturated with precursor, further adsorption of precursor molecules would not take place and a plot of growth rate

Appendix B (Continued)

vs. precursor pulse time would reach a plateau after a certain precursor pulse duration. The precursors were broken up into functional groups and their interaction parameters were found using an optimization algorithm. These interaction parameters were then used to compute the activity coefficients using UNIFAC GCM based on ASST. Then the number of moles of Zr in the surface, n_{Zr}^s , was calculated and used to calculate the theoretical growth rate. **Equation 1** was used to calculate the theoretical growth rate, where n_{Zr}^s is the number of moles of Zr in a monolayer of ZrO_2 , N_A is Avogadro's number, h_{Zr} is the thickness of a ZrO_2 monolayer, and C_{Zr}^{ml} is the number of Zr atoms in a monolayer. The theoretical growth rate was then compared to the experimental growth rate and used to determine whether the optimization of the interaction parameters was completed.

$$GR_{cal} = \frac{n_{Zr}^s N_A h_{Zr}}{C_{Zr}^{ml}} \quad (1)$$

Experimental and theoretical growth rates versus precursor pulse duration from using ZyALD as the Zr precursor and ethanol as the oxidizer are shown in **Figure 59a**. As the experimental and theoretical growth rates are quite similar, the interaction parameters from this system were expected to be optimized. **Figure 59b** shows the experimental growth rates from using ZyALD as the Zr precursor and oxygen/ozone as the oxidizer with the theoretical growth rates calculated using the interaction parameters from ZyALD and ethanol. The large difference in between the experimental and theoretical growth rates in **Figure 59b** suggests that the choice of oxidizer plays a significant role in the reaction. This is consistent with the experimental growth rates as the growth rate with oxygen/ozone as the oxidizer is ~3x greater than the experimental growth rate with ethanol as the oxidizer. Therefore, the functional groups from the oxidizer may need to be included in the modeling approach to more accurately fit data from the same precursor, but different oxidizers.

Appendix B (Continued)

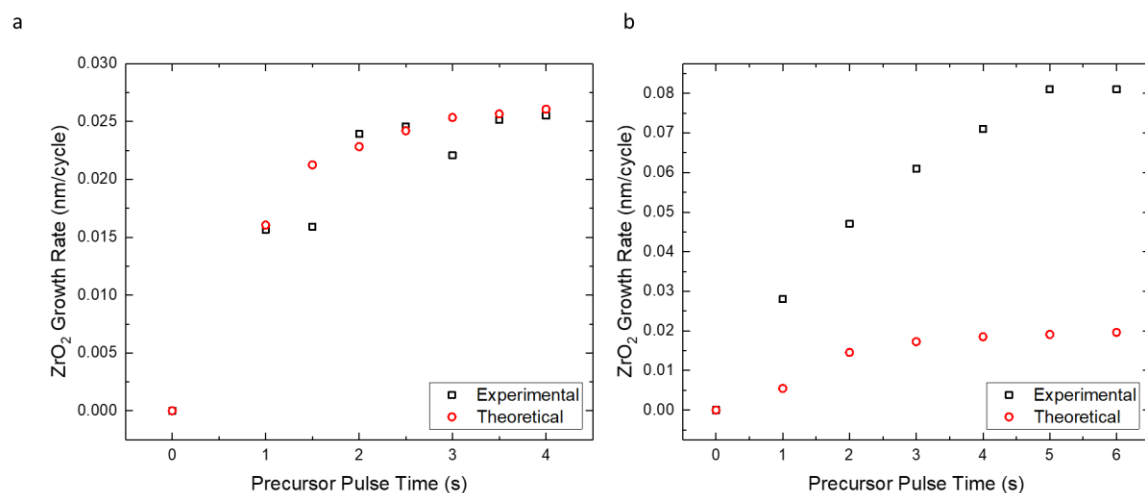


Figure 59. Experimental and theoretical growth rates of ZrO₂ on silicon substrates versus precursor pulse time. (a) Experimental growth rates are from ALD performed using ZyALD as the Zr precursor and ethanol as the oxidizer and theoretical growth rates are from the interaction parameters from ZyALD and ethanol. (b) Experimental growth rates are from ALD performed using ZyALD as the Zr precursor and oxygen/ozone as the oxidizer and theoretical growth rates were calculated using the interaction parameters from ZyALD and ethanol.

Appendix B (Continued)

B.2 Additional Evaluation of Screen Printing and Laser Trimming of Screen-Printed Strain Gauges

Graphic printing techniques are of great interest for fabrication of low-cost electronic devices and especially for strain gauge arrays for structural health monitoring. However, these techniques generally are not capable of the same level of reproducibility as conventional microfabrication techniques. Here we further evaluated screen printing process for producing small arrays of strain gauges and fine and different line widths as well as the effect of laser trimming screen-printed gauges.

Screen printing was done using a Gold Print SPR 25 screen printer, a printing offset of ~ 1 cm and 80 durometer squeegee blades. The screen pattern used had 325 wires per inch, wire diameters of $22.9\text{ }\mu\text{m}$, an emulsion thickness of $12.7\text{ }\mu\text{m}$, and a mesh angle of 22.5° . DuPont 7102 carbon ink was screen printed onto PET or polyimide film and heated to 100°C for two hours. Prior to screen printing, the PET and polyimide films were cleaned with IPA. In addition, the PET film was heated to 100°C for two hours prior to printing to prevent dimensional changes when drying the ink. Images of the printed gauges are shown in **Figures 60** and **61**. From the images in **Figure 61**, the line widths of the gauges appear to show the greatest variation for the finest lines. The approximate line widths and thicknesses from **Figure 61** are shown in **Table XI**. Here we also see a larger deviation in width for the gauges

Design Line Width [μm]	Screen Printed Line Width [μm]	Approximate Ink Thickness [μm]
150	186.47	8
250	272.55	8
500	500.99	10

TABLE XI. SCREEN PRINTED LINE WIDTHS AND APPROXIMATE THICKNESSES FOR GAUGES WITH DIFFERENT LINE WIDTH DESIGNS. LINE WIDTHS WERE MEASURED FROM THE OPTICAL MICROSCOPY IMAGES AND LINE THICKNESSES WERE APPROXIMATED FROM THE OPTICAL PROFILOMETRY IMAGES SHOWN IN **FIGURE 61**.

Appendix B (Continued)

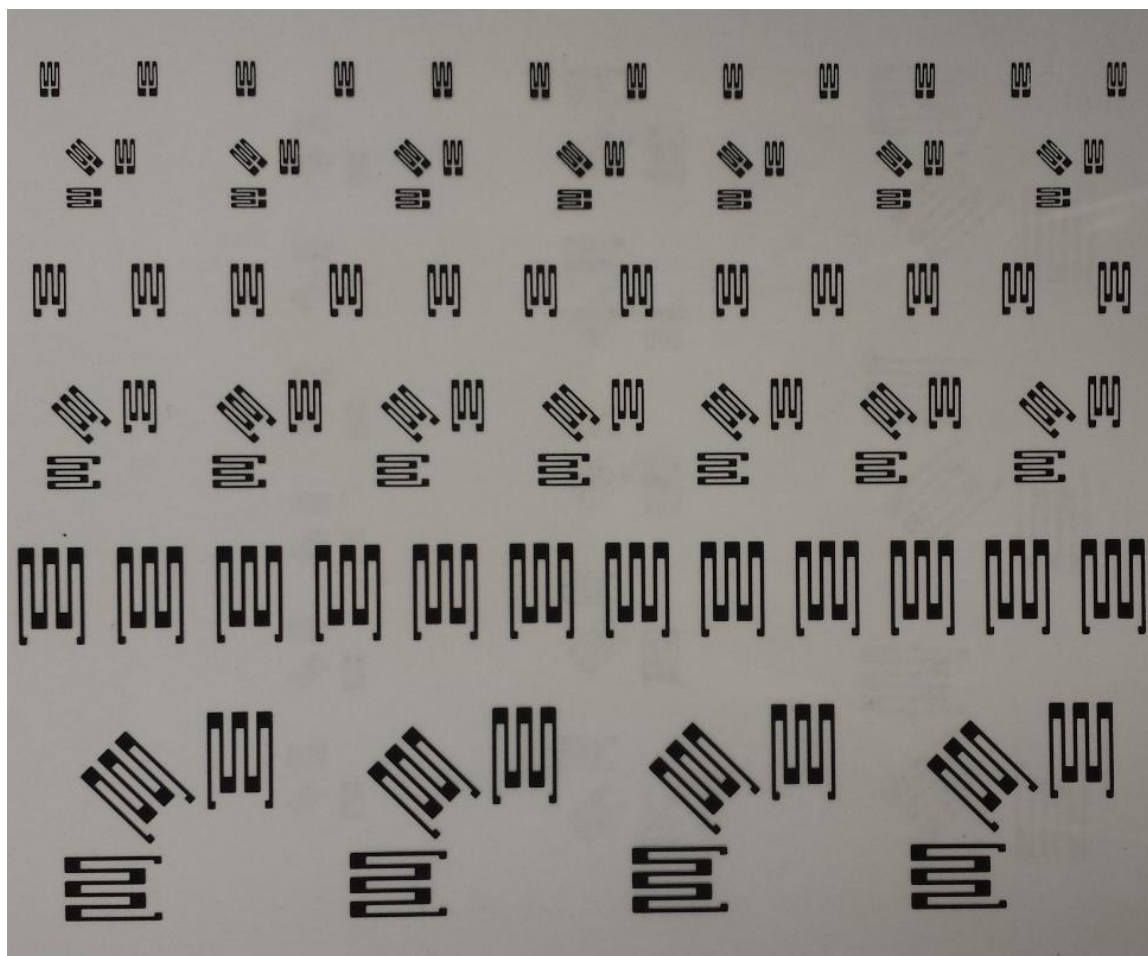


Figure 60. Image of screen-printed DuPont 7102 carbon strain gauges on PET.

Appendix B (Continued)

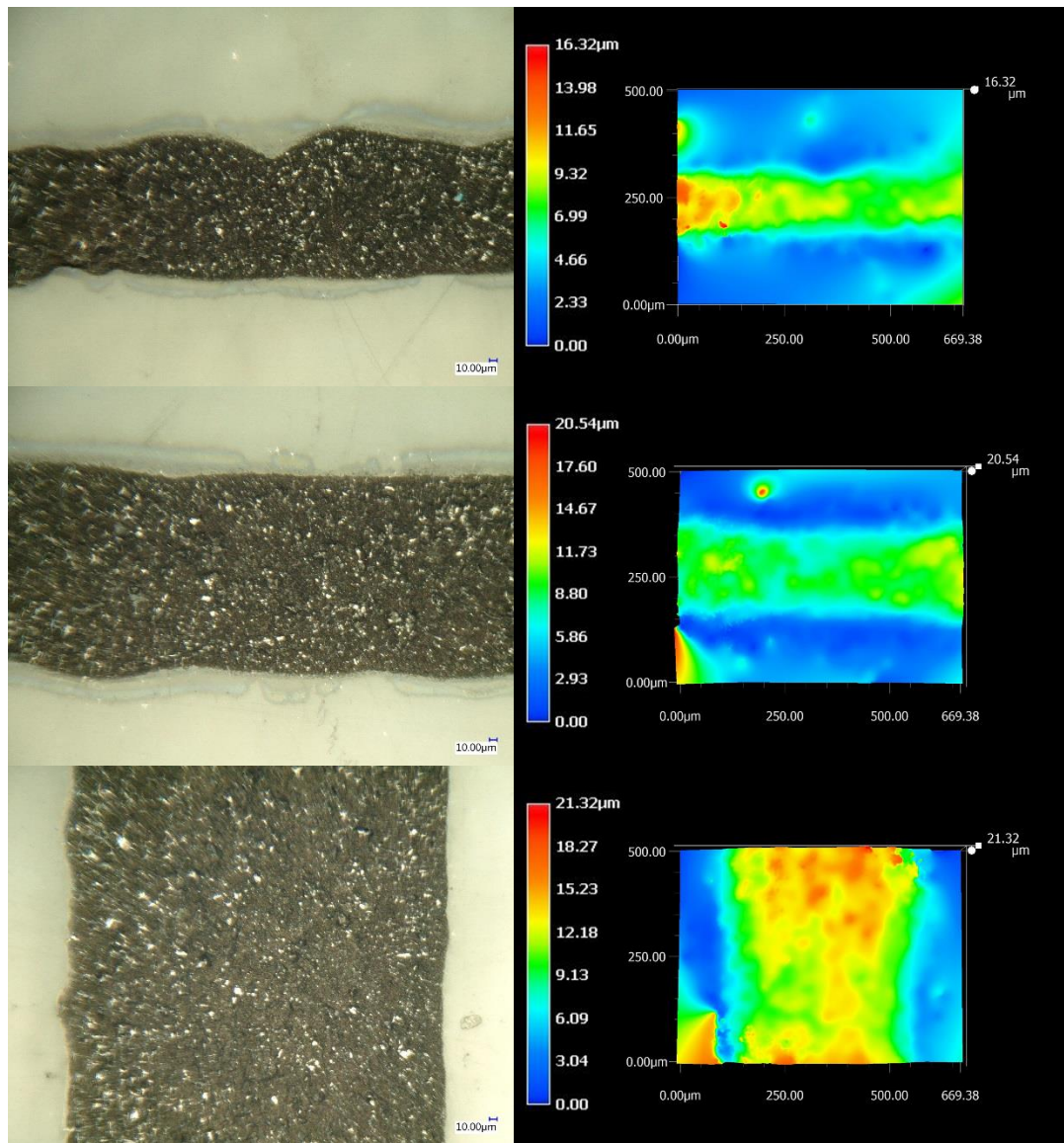


Figure 61. Optical microscopy and optical profilometry images of DuPont 7102 carbon ink strain gauges screen printed onto PET. The top images correspond to the finest line width devices (150 μm), the middle images correspond with the intermediate line width devices (250 μm), and the bottom images correspond to the thickest line width devices (500 μm).

Appendix B (Continued)

with the finest line widths. This deviation is believed to be due to uneven ink transfer through the screen pattern due to particles from the carbon ink accumulating in the screen mesh during printing, and which would have the largest effect for finer line widths. This accumulation may occur as less finer line widths have less contact area with the squeegee. A solution to this problem may be to use a softer, more flexible squeegee that can more effectively apply shear force to the ink in these fine lines. The average and standard deviation of resistances from four arrays of strain gauges on PET substrates are shown in **Table XII**. Here we see the largest standard deviations in resistance for the finer line widths as well as increasing standard deviations for subsequent prints. The larger standard deviations for finer lines are likely due to the larger variation in line widths while increasing standard deviations with subsequent prints is due to accumulation of graphite particles from the carbon ink in the screen pattern. This accumulation was observed during the printing process as the inks gradually began to dry on the screen pattern. Careful control of the printing environment (temperature and humidity) and more thorough cleaning of the screen patterns may reduce accumulation of ink particles within the screen patterns.

Design Line Width [μm]	Sheet 1: Average Resistance [$\text{k}\Omega$] \pm Std. Dev	Sheet 2: Average Resistance [$\text{k}\Omega$] \pm Std. Dev	Sheet 3: Average Resistance [$\text{k}\Omega$] \pm Std. Dev	Sheet 4: Average Resistance [$\text{k}\Omega$] \pm Std. Dev
150	$7.158 \pm 6.2\%$	$10.005 \pm 9.6\%$	$11.686 \pm 12.3\%$	$13.515 \pm 12.9\%$
250	$6.280 \pm 4.4\%$	$7.748 \pm 6.6\%$	$8.009 \pm 16.1\%$	$8.121 \pm 7.1\%$
500	$5.731 \pm 3.8\%$	$6.754 \pm 4.9\%$	$6.451 \pm 5.4\%$	$6.077 \pm 8.5\%$

Table XII. Average resistances and standard deviations for DuPont 7102 carbon gauges screen printed onto PET.

In an effort to further reduce the resistance variations of these gauges, laser trimming was performed as is often done with resistors. Despite being commonly used for resistors, laser trimming of strain gauges has not been reported in literature and the effect of this trimming on gauge sensitivity has not been studied. Laser trimming was

performed with a Tykma Electrox EMS 300 laser marking system. The Nd:YAG laser emitted 1064 nm laser pulses at an average power of 1 or 2 W with a frequency of 4 kHz and a scan rate of 200 mm/sec. With an average power of 1W, the focused laser beam diameter is $\sim 25\ \mu\text{m}$ and with a power of $\sim 2\text{W}$, it is $\sim 40\ \mu\text{m}$. Change in resistance during the laser trimming was measured using a Fluke 23 multimeter connected to thin insulated wires which had been bonded to the silver contacts (DuPont 5028) of the strain gauges with silver epoxy (#8331, MG Chemicals).

Carbon strain gauges on PET after the laser trimming are shown in **Figure 62**. The laser trimming was found to completely remove the ink from the substrate at higher power and in the case of excessive power, the substrate was damaged. The effect of laser trimming on resistance of similar strain gauges is shown in **Figure 63**. Here the resistances of the printed gauges were found to vary linearly with iteration of laser trimming and suggests that careful laser trimming may be able to effectively tune the resistance values to a desired value. The primary limitation in these bench-scale experiments was the alignment of the laser with the printed gauge, and control of the laser power which could vary significantly with the location of the focal point of the laser. In addition to resistance, the effect of the laser trimming on gauge sensitivity was studied. Normalized change in resistance versus microstrain for gauges that were laser trimmed is shown in **Figure 64** and the resistance values and gauge factors for these gauges is shown in **Table XIII**. For the gauges tested, the gauge factors increased by as much as 47%;

Gauge	Resistance Before Trimming [k Ω]	Gauge Factor Before Trimming	Resistance After Trimming [k Ω]	Gauge Factor After Trimming
0-1	6.344	$5.74 \pm 18.3\%$	6.602	$8.46 \pm 14.4\%$
45-1	5.660	$12.44 \pm 9.4\%$	6.617	$15.33 \pm 12.2\%$
90-1	5.629	$21.90 \pm 10.2\%$	6.535	$22.36 \pm 6.9\%$
0-2	6.157	$6.24 \pm 18.7\%$	6.760	$7.21 \pm 14.5\%$
45-2	5.487	$12.70 \pm 11.4\%$	6.557	$14.99 \pm 8.2\%$
90-2	5.180	$20.24 \pm 10.1\%$	-	-

TABLE XIII. RESISTANCES AND GAUGE FACTORS BEFORE AND AFTER LASER TRIMMING FOR TWO DUPONT 7102 CARBON 45-DEGREE ROSETTES ON PET. GAUGE FACTORS INCLUDE THE STANDARD ERROR FROM THE LINEAR REGRESSION. GAUGE 90-2 WAS DAMAGED BY THE LASER TRIMMING DUE TO MISALIGNMENT OF THE LASER.

Appendix B (Continued)

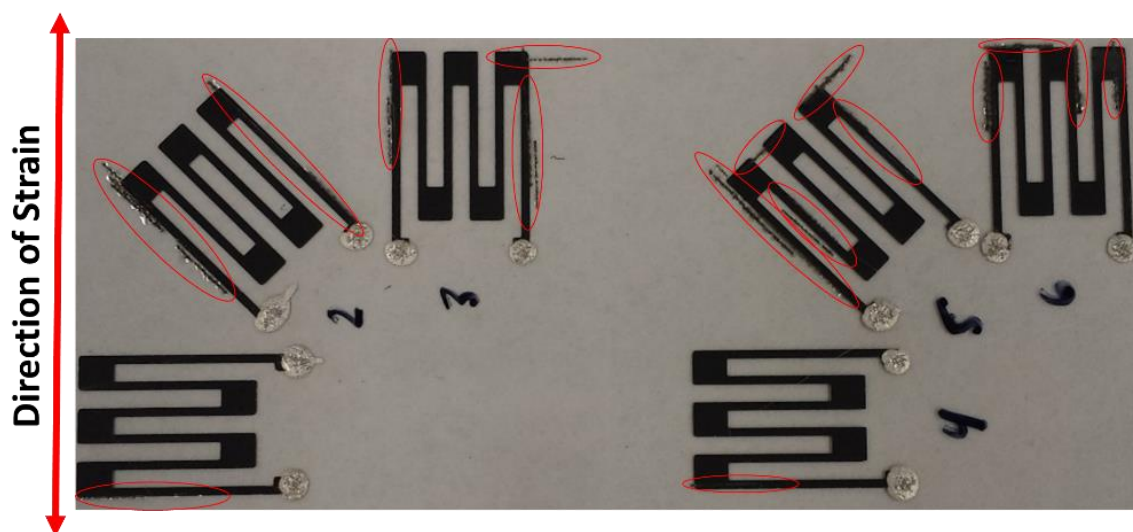


Figure 62. DuPont 7102 carbon gauges on PET after laser trimming. Red circles indicate where the laser trimming was performed.

Appendix B (Continued)

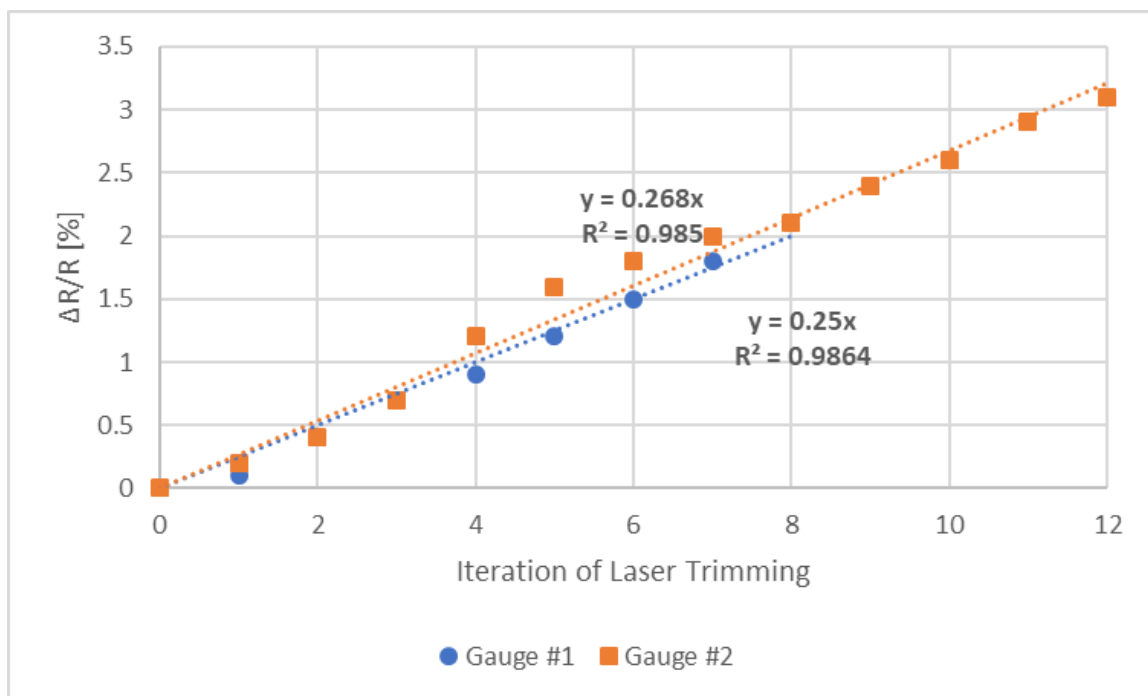


Figure 63. $\Delta R/R$ versus laser trimming iteration for two DuPont 7082 carbon strain gauges on PET.

Appendix B (Continued)

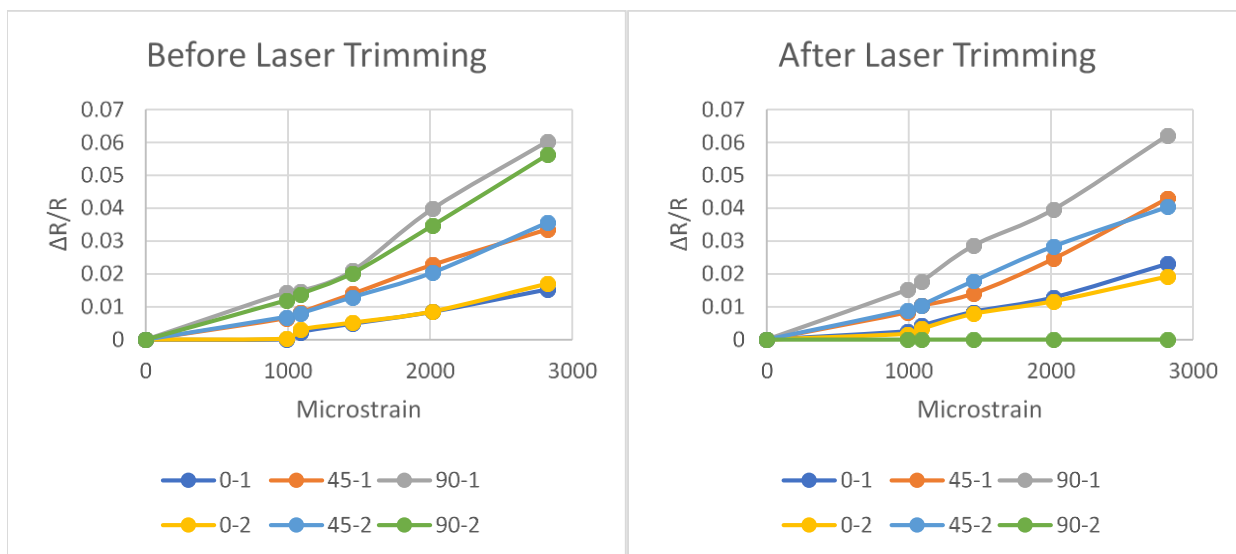


Figure 64. $\Delta R/R$ versus microstrain for two DuPont 7102 carbon 45-degree rosettes on PET before and after laser trimming. Gauge 90-2 was damaged by the laser trimming.

Appendix B (Continued)

however, the change in gauge factor did not appear to correlate with the amount of laser trimming required to meet a nominal resistance value. Change in gauge factor is likely due to the precise location of the laser trimming. Trimming the finer sections of the gauge is likely to have a larger effect on the sensitivity as removing material from these locations can result in very thin electrical connections which are more sensitive to applied strain. Thus, laser trimming the ends of the gauges is anticipated to have less effect on the sensitivity. However, these results also suggest that gauge sensitivity can be increased by altering the dimensions of the gauges after printing. Therefore, laser trimming may be used to achieve finer line widths than are capable from the printing process while simultaneously increasing the sensitivity of the gauges.

VITA

Nickolas Dean Anderson

- Education: Ph.D., Bioengineering,
University of Illinois at Chicago, USA
June 2019
- B.S., Bioengineering,
University of Illinois at Chicago, USA
May 2014
- Publications: **Anderson, N.**, Saha, S., Jursich, G., & Takoudis, C. (2019) "Selective Atomic Layer Deposition of Zirconia on Chemically Mechanically Polished Copper Substrates." In Preparation
- Anderson, N.**, Saha S., Jursich, G., & Takoudis, C. (2019) "On the Area Selective Atomic Layer Deposition of Zirconia on Electroplated Copper-Based Substrates." *ECS Solid State Science and Technology*. Submitted
- Bishal, A., **Anderson, N.**, Hung S., Koh, A., Sukotjo, C., & Takoudis, C. (2019) "Highly Conductive and Flexible Biomaterial Achieved by Low Temperature Atomic Layer Deposition on Collagen." *Biosensors and Bioelectronics*. Revision in Progress
- Anderson, N.**, Szorc, N. Gunasekaran, V. Joshi S., & Jursich G. (2019) "Highly Sensitive Screen printed Strain Sensors on Flexible Substrates via Ink Composition Optimization." *Sensors and Actuators A: Physical*. 290, 1-7.
- Joshi, S., Bland, S., DeMott, R., **Anderson, N.**, & Jursich, G. (2017) "Challenges and the state of the technology for printed sensor arrays for structural monitoring." *SPIE: Industrial and Commercial Applications of Smart Structures Technologies*. 10166, 101660H.
- Zhang, Y., **Anderson, N.**, Bland, S. Nutt S., Jursich, G., & Joshi, S. (2017) "All-printed strain sensors: Building blocks of the aircraft structural health monitoring systems." *Sensors and Actuators A: Physical*. 253, 165-172
- Presentations: **Presenter**, "Multiplexed Strain Sensor Arrays via All-Printing Fabrication on Flexible Substrates" Flex: Building the Innovation Ecosystem of Flexible Electronics, Feb 29 – Mar 3, 2016, Monterrey, CA.